Università degli Studi di Napoli *Federico II*

DOTTORATO DI RICERCA IN FISICA

Ciclo XXIX

Coordinatore: Prof. Salvatore Capozziello

Dose and image quality in
X-ray phase contrast breast imaging

Settore Scientifico Disciplinare FIS/07

Dottorando

Dr. Antonio Sarno

Tutore

Prof. Paolo Russo

Prof. Giovanni Mettivier

Anni accademici 2014/2017

Università degli Studi di Napoli *Federico II*

PhD in Physics

XXIX cycle

Dose and image quality in
X-ray phase contrast breast imaging
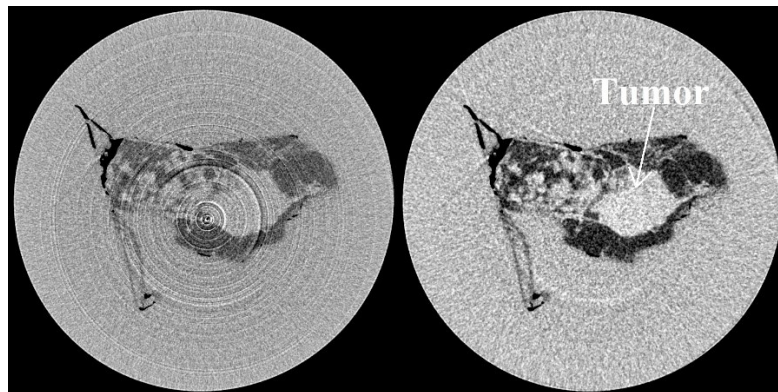
Candidate

dott. Antonio Sarno

Supervisors

Prof. Paolo Russo

Prof. Giovanni Mettivier

Academic Years 2014/2017

Preface

This thesis is submitted to the University of Naples "Federico II" for partial fulfillments of the requirements for the degree of *Philosophiae Doctor* (Ph.D.). It is based on my research work on X-ray breast dosimetry and phase-contrast imaging carried out during my PhD course. The data presented in this thesis are contained in ten original papers, to which I contributed substantially, published in peer-reviewed international journals and presented at three international congresses and two national congresses. Four addition articles, whose results are included in this thesis, have been submitted to peer-reviewed international journals, in the last months of this work.

This work has been carried out under supervision of Prof. Paolo Russo and co-supervision of Prof. Giovanni Mettivier, who approved this thesis work.

The results contained in this thesis have been carried out at the following institutions/facilities:

Dose and image quality in X-ray phase contrast breast imaging

List of contents

Figures index

IX

Tables index

Summary

Nowadays, mammographic examination is the gold standard technique for detecting breast cancer in asymptomatic women. However, it presents some limitations, mainly due to the superimposition of the tissues in the 2D mammograms, which may hide tumor lesions. Partially (digital breast tomosynthesis) and fully (CT dedicated to the breast) 3D breast imaging techniques have been developed in order to have a better tissues separation and to overcome such a limitation. Along with 3D breast imaging, the use of the X-ray beam phase shift, via so-called phase-contrast imaging techniques, has been shown to be a promising method in order to increase the image contrast between glandular tissue and tumor lesions. Indeed, in phase-contrast the image contrast is due to the X-ray wave phase-shift between different imaged materials, while in conventional imaging the image contrast arises from the different attenuation they introduce.

Among all phase-contrast techniques, propagation based phase-contrast imaging does not need any special optical elements in the beam path, but only an X-ray beam with a certain degree of coherence and enough distance between imaged object and detector. It can be implemented either with synchrotron radiation source or with a compact X-ray tube. The 3D propagation based phase-contrast breast imaging devices are not yet employed in the routine clinical exams but they are available only at experimental level, and appropriate evaluations of image quality and dose are necessary. This is needed in order to optimize the various techniques and to understand the corresponding dose limitations.

In this thesis, the dose paradigms in X-ray breast imaging are revisited and specific Monte Carlo simulation codes have been developed. A part of this work focuses on the breast dose aiming at studying the adopted breast models and the effects of the breast partial irradiation on the dose estimates, as occurs in 2D spot mammography clinical examinations as well as by adopting a narrow beam produced via synchrotron radiation.

The second part of this work focuses on the image quality obtainable in 3D images of the breast by adopting propagation based phase-contrast imaging. We present the CT scanner dedicated to the breast developed within the SYRMA-CT project at Elettra synchrotron radiation facility. We evaluate its imaging performance in terms of spatial resolution, image noise properties and capability of showing breast lesions and microcalcification clusters.

Finally, the CT scanner dedicated to the breast, developed at the University of Naples, which relies on compact X-ray source with a 7-μm focal spot is presented and its image performance at dose comparable to that adopted in two-view digital mammography is explored together with its capability of producing phase-contrast effects. This scanner was developed and studied in order to compare a scanner which is clinical feasible in terms of cost, setup dimension and scan time to the results obtainable via the high flux and monochromatic X-ray beam synchrotron based experimental scanner.

1. Introduction

1.1. The breast cancer burden and new breast cancer detection techniques

The breast cancer is today the most common cancer affecting women all over the world. The Globocan (2012) estimated 1.67 millions of new diagnosed cases and 0.52 millions of deaths breast cancer related among the women in 2012. Since the late 80s, when breast cancer mammographic screening programs started in several countries all over the world, the mortality related to such a disease have been drastically reduced. As shown in fig. 1.1, the mortality of women in USA reduced down to 20 per 100.000 females in 2012 from a starting value of about 35 per 100.000 in 1990.
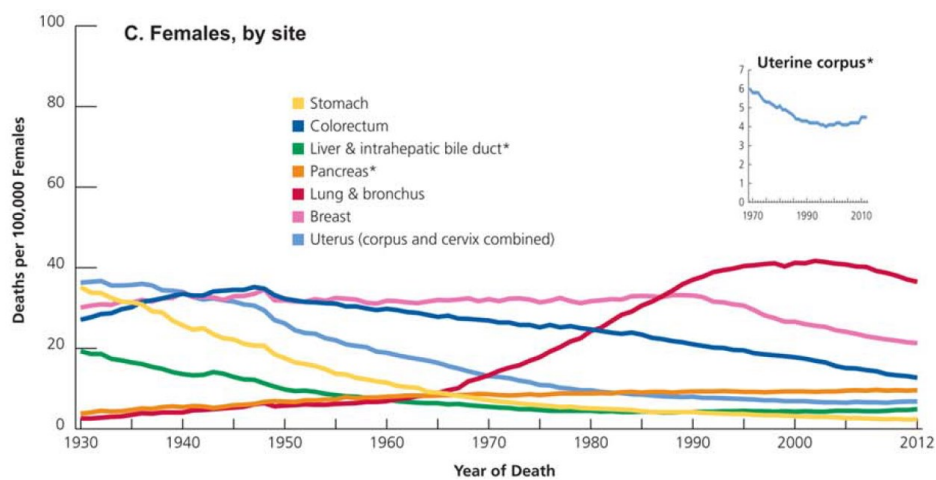
Fig. 1.1. *Deaths per 100,000 females in USA due to most common cancers (from Siegel et al 2016).*

Although the mammographic examination is today the gold standard technique for screening and diagnosis of breast cancer, it presents some limitations. Its sensitivity (i.e. the percentage of cancers with a positive initial interpretation) and the specificity (the percentage of non-cancer with a correct initial interpretation) are 84.9% and 90.3%, respectively (BCSC 2009a). Its performance is even lower in the case of young women (BCSC 2009b), who present denser breasts. It is worthy of noting that BCSC (2009a) defines cancers (or non-cancers) "the number of examinations with (or without) a tissue diagnosis of cancer within 1 year following the examination", so overestimating these parameters by excluding the misdiagnosis avoidable with a larger time lapse. Such non-ideal performance of the mammographic examinations are caused mainly by the superimposition of the breast tissues in the mammograms. In fact, this is a 2D image of a 3D compressed breast, and the breast tissues, mainly composed by glandular tissues and adipose tissues, overlap in the final image with the possibility of hiding the tumor masses and leading to a misdiagnosis.

In order to overcome the limitations proper of conventional 2D mammography, 3D imaging techniques dedicated to the breast have been developed. The digital breast tomosynthesis (DBT) allows producing non-isotropic 3D images of the compressed breast from several projections

acquired by several angles (Sechopoulos 2013a, 2013b). The final output is a stack of images of different planes of the compressed breast, parallel to the detector plane, with an in-plane spatial resolution of approximately 3–3.5 mm^{-1}, depending on the manufacturer. It is today employed for breast cancer diagnosis in conjunction with mammography and clinical studies for its usage in screening exams have started (Lång *et al* 2016).

The computed tomography dedicated to the breast (BCT) is a fully 3D X-ray imaging technique with an isotropic 3D spatial resolution (proposed in 2001 by Boone *et al* 2001a and Chen and Ning 2001 and recently reviewed in Sarno *et al* 2015). During a BCT examination, the patient lays on a support in prone position and the breast hangs from a hole in the support at the scanner isocenter. The gantry rotates below the patient support in the coronal plane in order to acquire several projections, usually more than 300, in order to reconstruct a 3D image of the breast. The imaged breast does not undergo the strong compression used in mammography and in DBT, so avoiding pain and discomfort for the patients.

While, on one hand, the BCT avoids the issue of the superimposition of tissue features in the 2D imaging technique, on the other hand it presents some unresolved limitations when compared with the conventional 2D mammography. First, the spatial resolution in 2D digital mammographic images is up to 12 mm^{-1} and it is several time higher than in the 3D BCT images (Sarno *et al* 2015) leading to difficulties in the microcalcifications detection (Lindfors *et al* 2008, O'Connell *et al* 2010). Moreover, the dose to the breast, assessed for the BCT scanner produced by Koning corp (http://koninghealth.com/), which received the CE mark in 2012 and the FDA approval in 2015 to be used in diagnosis along with mammography, resulted up to 7.2 times higher than that employed in two-view full-field digital mammography (Sechopoulos *et al* 2010).

Although in the 3D images produced via the BCT scanners the breast lesion may not be hidden by the healthy breast tissue, the physical properties of the tissues can make the former hardly distinguishable from the glandular tissue. In fact the attenuation coefficients, and then the corresponding gray level in the reconstructed CT slices, of the breast cancer tissue and the glandular tissue are similar. These results suggested to investigate beyond the absorption-based imaging technique and so exploring alternative breast imaging techniques. Exploiting the signal from the X-ray beam phase-shift, the so called phase-contrast imaging, has been shown as valid alternative to the absorption-based imaging (Bravin *et al* 2013). The complex refractive index, *n*, of the imaged sample material can be represented as:

$$n = 1 - \delta - j\beta. \tag{1.1}$$

Hence, the attenuation coefficient (μ) and the wave phase shift (ϕ) – for unit of length – introduced by such a sample are (Bravin *et al* 2013):

$$\mu = 4\pi \frac{\beta}{\lambda}, \tag{1.2}$$

$$\phi = 2\pi \frac{\delta}{\lambda}, \tag{1.3}$$

where λ is the X-ray wavelength. These equations relate the imaginary part of the refractive index to the attenuation introduced by the sample and the phase-shift to the decrement from unit of the real part of *n*. In the case of the breast tissues, in the energy range usually adopted in X-ray breast imaging, *δ* is more than 3 order of magnitude higher than *β* (CSIRO). For these reasons, phase-contrast mammography *(*Castelli *et al* 2011; Quai *et al* 2013; Longo *et al* 2014) and phase-contrast breast tomography (Fiedler *et al* 2004; Bravin *et al* 2013; Keyriläinen *et al* 2005, 2008; Momose *et al* 1996; Sztrókay *et al* 2013; Takeda *et al* 1998, 2000; Zhao *et al* 2012; Gureyev *et al* 2014) are under investigation as new imaging techniques for a potentially better definition and increased conspicuity of breast lesions at diagnosis. The potential of these techniques has been explored both with monochromatic synchrotron radiation (SR) X-ray sources (David *et al* 2007*;* Keyriläinen *et al* 2008) and with polychromatic X-ray tube sources (Cai and Ning 2009; Bravin *et al* 2013; Scherer *et al* 2016).

Among all the phase-contrast techniques, propagation-based phase contrast imaging (PB-PhC) does not need special optical elements in the beam path, compared to techniques which require complex optical setups (Fiedler *et al* 2004; Keyriläinen *et al* 2005, 2008; Momose *et al* 1996; Sztrókay *et al* 2013; Takeda *et al* 1998, 2000; Zhao *et al* 2012; David *et al* 2007*;* Cai and Ning 2009), but only an X-ray incident beam with some degree of spatial coherence and a sufficient distance between the imaged object and the detector. It can be implemented either with SR sources (Longo *et al* 2016, Sarno *et al* 2016a, Nesterets *et al* 2015) or in the laboratory using compact micro-focus X-ray tubes (Auweter *et al* 2014). The advantages of the edge enhancement effects in PB-PhC produced by X-ray refraction at the boundary of different tissue structures have already been shown in FFDM (Tanaka *et al* 2005, Honda and Ohara 2008), where "Clinical trials suggest superior detection of both mass and microcalcification" by PB-PhC based over the conventional absorption based FFDM (Tanaka *et al* 2005). Similar results were obtained with monochromatic X-ray radiation produced by synchrotron source, where edge enhancement effects "substantially improves the diagnostic quality of the images" (Dreossi *et al* 2008).

1.2. The SYRMA-CT project

In order to exploit both the advantages offered by the 2D and 3D PB-PhC imaging of the breast and those due to the phase-shift due to the PB-PhC, the SYRMA-CT (Synchrotron Radiation Mammography - Computed Tomography) project aims at producing the first 3D diagnostic images of the uncompressed breast, employing a high coherence and monoenergetic X-ray beam produced by a SR source. The SYRMA-CT project started in 2014 and it is funded by the INFN (Istituto Nazionale di Fisica Nucleare). It involves the teams of University of Napoli "Federico II", University of Trieste, University of Cagliari, University of Pisa and University of Ferrara, together with the INFN sections of Napoli, Trieste, Cagliari, Pisa and Ferrara and the INFN spin-off PIXIRAD srl,

which produces the detector employed into the developed setup and the Elettra-Sincrotrone Trieste SPcA where the SYRMA-CT system is installed.

1.3. This work

This work aims at investigating dosimetry and image quality in propagation-based phase-contrast imaging of the breast.

In breast imaging the reference dosimetric quantity is the dose absorbed, on average, in the glandular tissue (mean glandular dose - MGD), since the gland is the highest radiosensitive breast tissue. In mammography, the beam originating from the X-ray tube irradiates the whole breast volume. However, in the case of a breast partial irradiation, there is no protocol, which defines the dose paradigm and corresponding estimation techniques. A partial irradiation of the breast volume occurs for synchrotron radiation breast tomography in the SYRMA-CT project, since the beam height is much less than the height of the pendant breast from chest-wall to nipple. For this reason, the SYRMA-CT team considered to develop a Monte Carlo (MC) code in order to define and estimate the glandular dose in synchrotron radiation breast CT. In this thesis, we have developed a MC code for estimation of the MGD in the case of total as well as in partial irradiation, both with monoenergetic and polyenergetic beams, for 2D geometry (mammography) and 3D geometry (breast CT). The code has been validated vs the protocol of the American Association of Physicists in Medicine (report TG-195, Sechopoulos *et al* 2015) and via measurements at a synchrotron radiation facility (Elettra ScPA).

The SYRMA-CT project has made an extensive series of measurements at the Elettra facility (2014–2015), on breast phantoms and samples for image quality assessment and detector performance characterization, in CT irradiation geometry. This thesis reports the results of the analysis of those image datasets; in particular we have analyzed the system in terms of spatial resolution (modulation transfer function - MTF), image noise (noise power spectrum - NPS) and its capability in revealing breast lesions. Moreover, we investigated a phase-retrieval algorithm and an iterative reconstruction algorithm (developed for the SYRMA-CT project) in order to improve the image quality and to reduce the absorbed dose while preserving an acceptable image quality.

During this thesis, laboratory work has been carried out on the phase-contrast cone-beam micro CT scanner dedicated to the breast prototype (BµCT) developed at University of Naples, which features a micro focus X-ray tube with a focal spot as small as 7 µm and high resolution flat-panel detector with 50−µm pixel pitch. An image assessment has been performed on breast phantoms.

The thesis is structured as follows. The first part is dedicated to revisit dose paradigm in 2D full-field breast imaging (sect. 2), then the X-ray breast dosimetry in 2D partial breast irradiation is

studied, with a particular focus to the dose absorbed in the non-directly irradiated breast tissue due to the scattered radiation.

In the sect. 3, the results of the previous section have been transposed to the 3D case. The breast model in an uncompressed breast geometry, as adopted in BCT, is investigated and the conversion factors from the measured air kerma at the scanner isocenter to the dose to the radiosensitive breast tissue have been calculated both for monoenergetic and polyenergetic X-ray beams. Then, the conversion coefficients have been evaluated for the case of partial breast irradiation in pendant geometry, as proposed for the clinical studies in the SYRMA-CT project.

The sect. 4 is dedicated to the image quality assessment in BCT. The first part (sect. 4.1) shows the image quality achievable by the SYRMA-CT setup. In sect. 4.2, the feasibility study of the 3D breast imaging via the BµCT scanner developed at the University of Napoli is presented. It is based on the dosimetric conversion factors calculated in the previous sections and aims at showing that a high resolution scanner which relies on 7-µm focal spot and high resolution X-ray detector can be adopted with scan times not prohibitive for breast imaging. The image quality achievable with this scanner is presented and compared to that achievable by the clinical BCT prototypes.

2. Dosimetry in 2D X-ray breast imaging

This chapter presents investigations in which I was involved during this PhD thesis, whose results are reported in the following publications:

- Sarno et al 2016 Monte Carlo study of monoenergetic and polyenergetic normalized glandular dose (DgN) coefficients in mammography, Phys. Med. Biol. 62 306–325
- Sarno et al 2016 Monte Carlo evaluation of normalized glandular dose coefficients in mammography, Breast Imaging. Proc. of 13th International Workshop, IWDM 2016, Malmö, Sweden, June 19-22, 2016, Lecture Notes in Computer Science, Springer International Publishing, vol 9699, 190–196 DOI 10.1007/978-3-319-41546-8_25
- Sarno et al 2017 Air kerma calculation in Monte Carlo simulations for deriving normalized glandular dose coefficients in mammography. Phys. Med. Biol. under review
- Sarno et al 2017 A Monte Carlo model for mean glandular dose evaluation in spot compression mammography. Med. Phys. under review

2.1. Full-field mammography

In X-ray mammography, as well as in DBT and BCT, the mean glandular dose (MGD) is used in the evaluation of radioinduced cancer risk. Dose coefficients – such as normalized glandular dose (DgN), (i.e. the ratio between the MGD and the air kerma in a given position), are evaluated via Monte Carlo (MC) simulations, in order to derive corresponding MGD estimates on the basis of air kerma measurements in given positions of the irradiation field. A recent review of dosimetry in X-ray breast imaging has been reported by Dance and Sechopoulos (2016). In such a context, the breast is modeled as a homogenous mixture of glandular and adipose tissue embodied in a skin layer, usually 4-mm thick (Wu *et al* 1991; Boone 1999, 2002; Boone *et al* 2004; Sechopoulos *et al* 2007; Nosratieh *et al* 2015). Dance (1990) and Dance *et al* (2000, 2009, 2014) proposed to adopt a 5-mm adipose layer in order to simulate the shielding layer surrounding the adipose-glandular tissue of the standard breast: this model is the one adopted in the European Guidelines for breast cancer imaging (European Commission 2006). On the other hand, Boone (2002) modeled the skin as a layer of glandular-adipose tissue of appropriate equivalent thickness. However, skin introduces also a spectral distortion (beam hardening and scattered radiation) of the X-ray beam, whose extent could be estimated by adopting a partially homogeneous breast model ("real" rather than equivalent skin tissue on the outside, homogeneous mixture of adipose and glandular tissue in the internal "breast tissue" volume).

On the basis of the analysis of 3D images produced by BCT scans on a relatively large cohort of patients, Huang *et al* (2008) and Shi *et al* (2013) found that the most probable value of breast skin thickness was 1.45±0.3 mm (range of skin thicknesses: 0.8−2.5 mm) and 1.44±0.25 mm (range: 0.87−2.34 mm) respectively, i.e. much less than the 4−5 mm thickness usually considered in breast dosimetry on the basis of histology. Huang *et al* (2008) showed that the use of a skin thickness of 4 mm, instead of 1.45 mm, leads to an underestimation of the DgN up to 20%, at 24 kVp with a conventional mammographic spectrum produced with a molybdenum (Mo) anode and an added Mo filtration. By converse, such an underestimation in DgN implies that the conventional breast models

might produce a dose underestimation up to ~20% in routine mammography examinations. On the other hand, using data from Shi *et al* (2013), Vedantham *et al* (2013) showed that, for dedicated breast CT, with respect to 1.45 mm, the percent deviation in Monte Carlo simulated DgN was in the range -7.91% to +6.87%, for a skin thickness from a minimum of 0.87 mm to a maximum of 2.34 mm, thus indicating that a significant variation in DgN may arise from different assumptions on the breast skin thickness.

Using ultrasound measurements *in vivo*, Sutradhar and Miller (2013) found that the thickness of the breast skin was in the range 0.83−2.4 mm, with an average of 1.55 ± 0.25 mm, in good agreement with the X-ray CT determinations of Huang *et al* (2008) and Shi *et al* (2013). However, histological determinations of skin tissue reveal the presence of an epidermis+dermis layer and a subcutaneous fat tissue layer: this last tissue was not distinguished as a separate skin fat tissue in dedicated breast CT scans on patients, where adipose breast parenchyma tissue is observed (as discussed in Huang *et al* 2008). Hence, the above considerations motivate the investigation of the specific effect of this model feature (the skin tissue layer) on DgN coefficients in mammography, in order to show the deviation in DgN resulting from different choices in the assignment of the breast skin thickness and composition.

The presence of the compression paddles also influences the results of MC simulations for mammography dosimetry, both for the beam hardening and for the scatter radiation generated when the X-ray beam traverses the paddles. Boone (2002) included a 3-mm thick polystyrene paddle in the MC geometry for DgN calculations in mammography (Nosratieh *et al* 2015), and Nosratieh *et al* (2015) computed polyenergetic DgN coefficients on the basis of the monoenergetic data provided with such a setup. In the calculation of dose coefficients, Wu *et al* (1991), Boone (1999; 2002), and Dance (1990) define the hardware setting (including or not the compression paddles in the geometry and fixing their thickness and material) and they consider the paddle thickness in terms of beam hardening introduced, without taking into account the different amount of scattered radiation produced by insertion of different paddles in the beam path.

Another aspect which deserves attention is the production of bremsstrahlung radiation by slowing down electrons in the breast material. Indeed, to our knowledge, MC codes for DgN determinations do not include the simulation of the bremsstrahlung radiation: a quantitative evaluation of this effect is still to be provided.

A recalculation of DgN coefficients is considered appropriate, for taking into account all the above effects and to evaluate the extent of their influence on MGD estimates. This chapter aims at exploring these issues in the MC evaluation of DgN coefficients in mammography. We evaluated the influence of skin thickness, compression paddle(s) thickness and bremsstrahlung radiation, on the calculated monoenergetic DgN(E) values in the range 8−80 keV. This interval covers the range of photon energy, E, usually adopted in mammography, as well as the higher energy range which is not usually adopted in mammography systems, this last providing an insight in the DgN parameters

for some research lines (e.g. Koukou *et al* 2017, Diemoz *et al* 2016). Then, we evaluated the influence of these parameters for several polyenergetic spectra (via calculation of polyenergetic DgN coefficients, DgN$_p$) routinely used in mammography. The present evaluation of DgN$_p$ coefficients extends the results obtained by Huang *et al* (2008) for other mammographic spectra.

We modeled the breast tissue also as a heterogeneous mixture of adipose and glandular tissue, checked against the common assumption of a homogeneous breast tissue. Indeed, small volume elements below the skin in the interior of the breast volume contain only glandular or adipose tissue. Sechopoulos *et al* (2012) and Hernandez *et al* (2015) evaluated the difference between the dose estimated by employing a homogeneous breast model and that evaluated with patient specific breast phantoms, this last simulating a heterogeneous breast tissue with real glandular distribution, which is usually manly located at the center of the breast volume. They showed that the adoption of the homogeneous model introduces a bias of 30% in dose estimation. However, they did not compared the two different ways of computing the dose in MC simulations. In fact, in dose computation for the homogeneous breast model the so called G-factor (see below) is adopted and it is not used for the dose computation with the heterogeneous model. In order to investigate quantitatively the difference in the mammographic DgN coefficients in the two assumptions (homogeneous vs. heterogeneous mixture with glandular tissue randomly distributed over the breast volume), we carried out specific additional MC simulations for DgN(E) coefficients.

2.1.1. Monte Carlo simulations

The MC simulations were performed with the GEANT4 toolkit version 10.00. The code included the electromagnetic physics list option 4 package, as used in the AAPM TG-195. As suggested in the AAPM TG-195, tracking electrons in MC simulations for dose to the breast evaluation may be avoided; furthermore, the influence of tracking electrons and simulating the bremsstrahlung processes on DgN coefficients has been studied in this work. Photoelectric interactions, incoherent and coherent scattering were simulated. The MGD was evaluated as:

$$\text{MGD} = \frac{\sum_i G_i(E) \times E_i^{\text{dep}}}{f_g \times W_b},\tag{2.1}$$

where E_i^{dep} is the energy released at the interaction event i, f_g is the breast glandular fraction by mass (e.g., $f_g = 0.2$ for a 20% glandular and 80% adipose breast), and W_b is the breast mass (skin excluded). The deposited energy in the breast tissue included the energy released by photons at their interaction site in the breast, as well as the energy released by electrons produced at the photon hit (multiple scatter included). The factor G(*E*), introduced by Boone (1999), was evaluated as (Dance and Sechopoulos 2016):

$$G(E) = \frac{f_g \times \frac{\mu_{en}}{\rho}(E)_g}{f_g \times \frac{\mu_{en}}{\rho}(E)_g + (1 - f_g) \times \frac{\mu_{en}}{\rho}(E)_a}.\tag{2.2}$$

Here, μ_{en}/ρ is the mass energy absorption coefficient of glandular (subscript g) and adipose (subscript a) tissues, evaluated by considering the functional interpolation given by Fedon *et al* (2015). In the cases of 0% glandular breasts the f_g was assumed equal to 0.001. The *G*-factor was evaluated interaction-by-interaction, at the current energy of the photon during the transport process (Wilkinson and Heggie 2001). Finally, the DgN values were computed as:

$$DgN = \frac{MGD}{K_{air}}. \tag{2.3}$$

While Dance (1990) simulated the ion chamber geometry in their MC simulation for glandular dose coefficients, other authors (Boone 1999, 2002; Sechopoulos *et al* 2007; Nosratieh *et al* 2015) computed K_{air} (or the x-ray exposure) from the photon fluence incident on a fixed scoring region at the entrance skin breast surface. Nosratieh *et al* (2015) calculated the photon fluence as suggested in Boone and Seibert (1997). To our best knowledge, there are no published reports which highlight the role of the photon incidence angle on the calculation of K_{air} for MC dosimetry in mammography. For this reason, we do not take into account such a contribution in this section. Indeed, the incident air kerma, K_{air}, was evaluated at the entrance skin plane, under the compression paddle, by scoring the photon fluence on a circle with a diameter of 50 mm with its center located at 25 mm from the chest wall, and by computing the air kerma as:

$$K_{air} = \frac{\sum_i E_i \times \frac{\mu_{en}}{\rho}(E_i)_{air}}{S}, \tag{2.4}$$

where E_i is the energy of the *i*-th photon which passes through the scoring surface S, and μ_{en}/ρ_{air} is the mass energy absorption coefficient of the (dry) air obtained from the NIST database. No backscatter from the breast is taken into account in the evaluation of K_{air}.

In the sect. 2.1.4 we introduce and evaluate the role of the incident photon angle on the scoring surface by considering the following formula for the air kerma calculation:

$$K_{air}^{\theta} = \sum_i \frac{E_i \times \frac{\mu_{en}}{\rho}(E_i)_{air}}{S \times \cos\theta_i}, \tag{2.5}$$

In the various cases examined, the percentage difference between DgN values calculated in two different ways was evaluated as:

$$\text{Percent deviation} = 100 \times \frac{DgN_{ref} - DgN_X}{DgN_{ref}}, \tag{2.6}$$

where the subscript *ref* indicates the reference value in the comparison.

For each MC simulation run, as many as 10^8 photons were generated. The single run took ~ 1 hour (processor: Intel Core i7−3770 CPU @ 3.40 GHz). The statistical uncertainty was evaluated as suggested in AAPM TG-195 and was less than 0.1%.

Values of DgN_p for polyenergetic spectra were computed by weighting the monoenergetic $DgN(E)$ coefficients at incident photon energy E as suggested by Boone (2002):

$$DgN_p = \frac{\sum_{E_{min}}^{E_{max}} \Phi(E) \times \vartheta(E) \times DgN(E) \times \Delta E}{\sum_{E_{min}}^{E_{max}} \Phi(E) \times \vartheta(E) \times \Delta E}. \tag{2.7}$$

where $\phi(E)$ is the spectrum at the entrance skin surface (photons/mm^2) and $\vartheta(E)$ is the photon fluence to air kerma conversion factor (mGy·mm^2/photons). Although Nosratieh *et al* (2015) proposed to include the compression paddle in the monoenergetic DgN values evaluation (so producing a polyenergetic X-ray beam at the entrance skin surface), in order to use properly the eq. 2.7, the monoenergetic DgN values have to be evaluated with a monoenergetic beam impinging on the breast surface. Moreover, the influence of the compression paddle is already contained in the beam shape $\phi(E)$ (properly evaluated just below the paddle as suggested by European Guidelines 2006). Hence, the compression paddle should be excluded by the simulations. This work shows the difference in the DgN$_P$ evaluated by adopting the two approaches.

Three different anode-filter combinations routinely used in mammographic units were taken into account: *a*) molybdenum anode with 0.030-mm molybdenum filter (Mo/Mo), *b*) molybdenum anode with 0.025-mm rhodium filter (Mo/Rh), *c*) tungsten anode with 0.050-mm rhodium filter (W/Rh). The spectra were computed in the range of tube voltages 18−40 kVp, with the code described in Boone *et al* (1997). In all cases an added filtration of 2 mm of PMMA was added. The spectra were tuned by added filtration layers (Mo or Rh) in order to match the beam HVL.

The MC code was validated as suggested in AAPM TG-195. Here, the cases I, II and III reported in the TG-195 have been implemented, corresponding to cases of interest for this study. Details on the cases considered and the resulting validations with the code developed in this work are shown in the Appendix A (Supplementary Material, sect. 9.1). In the Appendix A, we show that the MC code developed in this work agrees within the statistical uncertainties with the validation tests (cases I-III) of TG-195 (AAPM 2015; Sechopoulos *et al* 2015).

2.1.2. Breast models

The breast was modeled as proposed in the report AAPM TG-195 (AAPM 2015; Sechopoulos *et al* 2015), as a semicylinder with radius of 100 mm (including a skin layer of 2-mm thickness), and a compressed breast thickness of 50 mm. The patient body is modeled as a water box of volume 300×300×170 mm^3. The compression and breast support paddles were made of polymethylmethacrylate (PMMA) and have a thickness of 2-mm each. The isotropic X-ray source was placed at 595 mm from the upper surface of the breast and it was collimated in order to irradiate a detector surface of 140×260 mm^2 located at 15 mm below the bottom surface of the breast. The density and the composition of the patient body and of the compression paddles are those provided by National Institute of Standards and Technology (Hubbell and Seltzer 2004). The breast interior was modeled as a homogeneous mixture of glandular and adipose tissues; the composition and density of the external skin layer and the breast tissues are those provided by Hammerstein *et al* (1979).

In various MC simulation runs, the skin thickness was varied in order to evaluate its influence on DgN; the selected skin thicknesses were 5 mm, 4 mm, 3 mm, 2 mm and 1.45 mm. We also

investigated the influence on DgN estimates of the presence of a subcutaneous fat layer between the skin layer (composed by epidermis and dermis) and the inner breast. Moreover, we evaluated the influence of the compression paddles on DgN determinations by removing them from the beam path or by inserting them and then varying their thickness in the range 1−5 mm, in steps of 1 mm.

The breast tissue was modeled also as a heterogeneous mixture of adipose and glandular tissues. Specifically, the volume internal to the skin layer was modeled as a 3D matrix of a cubic voxels (size of $1\times1\times1$ mm^3); each voxel consisted of either 100% glandular or 100% adipose tissue. For a mixed-composition breast of glandular fraction f_g by mass, a fraction v_g of the total number of voxels contained glandular tissue and the remaining fraction $(1-v_g)$ of voxels contained adipose tissue, with the voxels containing glandular tissue randomly distributed in the breast volume. The fraction v_g was evaluated as:

$$v_g = \frac{f_g\times\rho_a}{(1-f_g)\times\rho_g+f_g\times\rho_a} \times V \tag{2.8}$$

where ρ_a and ρ_g are, respectively, the densities of the adipose tissue and the glandular tissue suggested by Hammerstein *et al* (1979), and V is the total number of voxels in the breast model.

We calculated the DgN for five breast models with different glandular distributions and their average DgN coefficients were evaluated. The effect of the randomization process was investigated by changing randomly the volume distribution of the glandular voxels in successive iterated runs of the MC simulations, and by plotting the scored quantity (monoenergetic MGD per incident photon) as a function of the iteration number.

Figure 2.1 shows the MGD per generated photon, for a 5-cm thick breast with 20% glandular fraction, for photon energies in the range 8−80 keV. The skin thickness was 1.45 mm (Fig. 2.1a) or 5 mm (Fig. 2.1b). The value of 20% glandularity represents a more realistic value for the average glandular fraction of the breast, than the commonly adopted value of 50% glandularity (see Yaffe *et al* 2009, where an average glandular fraction of 19.3% was found, including the skin). In both plots, examining the curves for the total energy deposit, one can consider that at the lower photon energies the skin layer "shields" the breast tissue and the dose to the glandular breast is low (less than $\sim 10^{-12}$ mGy/photon). At increasing photon energies, the X-ray beam penetrates the skin layer and the total dose to the glandular breast increases, up to a maximum at 23 keV (for 1.45 mm skin thickness) or at 24 keV (for 5 mm skin thickness). Then, at higher photon energies, the total dose first reduces and then starts to increase smoothly, reaching a broad minimum at about 65 keV. The decrease may be attributed to the energy dependence of the energy absorption coefficient of the breast tissue, which reduces as the photon energy increases (see Fig. B1a in Appendix B contained in the Supplementary Material). Indeed, the kerma in breast tissue per unit photon fluence follows this trend, with a broad minimum between 61 and 62 keV (see Fig. B1b in Appendix B contained in the Supplementary Material).

In fig. 2.1 the contributions from primary and from secondary radiation to the total MGD per photon are considered separately: the primary dose first increases (due to the skin shielding effect) and then steadily decreases (due to the decreasing μ_{en}/ρ). The dose due to secondary radiation reaches a broad peak at a higher energy than that of the sharper peak from primary radiation − since less secondary-energy deposits occur in the surface layers, and since energy deposition events by Compton interactions become more frequent at increasing energies (see Fig. B1 in Appendix B, sect. 9.2. contained in the Supplementary Material). Then, after a slight decreasing, it starts increasing at energies around 50 keV, representing the largest contribution to the total MGD per photon.

At energies higher than 28 keV, for a skin thickness of 1.45 mm, the MGD due to the secondary radiation is higher than that produced by the primaries. Such a specific energy value reduces as the skin thickness decreases: for a skin thickness of 5 mm it is 26 keV (29 keV when the skin is not simulated).
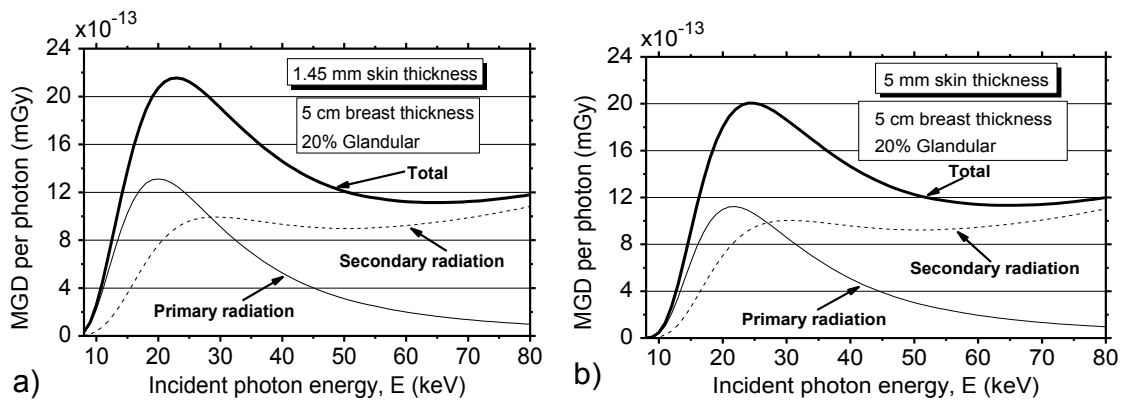
Fig. 2.1. *MGD per photon to a breast of 20% glandular fraction, due to primary photons (first hit), to secondary photons and due to both contributions (total) for skin thicknesses of 1.45 mm (a) and 5 mm (b).*

Figure 2.2 shows the MGD per photon due to the primary (Fig. 2.2a) and to the secondary radiation (Fig. 2.2b), for breast skin thicknesses of 1.45 mm and 5 mm, and a glandular fraction of 20%. For primary radiation, a thicker skin, which strongly shields the breast tissue, determines a lower MGD at all energies, in particular below 40 keV photon energy (Fig. 2.2a). At about 27 keV the probability of photoelectric interactions in skin tissue equals the probability of Compton interaction: for corresponding higher energies the skin becomes a *secondary radiation source*. A skin thickness of 1.45 mm determines higher MGD values than for the case of 5-mm thickness, for energies lower than 27 keV, i.e. in a range where the photoelectric effect is dominant (Fig. 2.2b). For energies higher than 27 keV, a thicker skin layer corresponds to a more intense secondary radiation source, so that the MGD due to secondary photons is slightly higher.
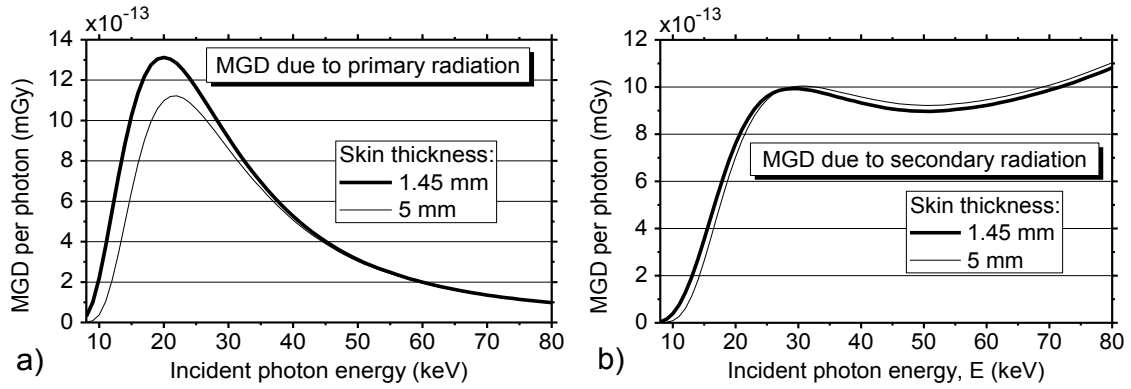
Fig. 2.2. *MGD per photon to a breast of 20% glandular fraction, due to the primary photons (a) and to the secondary photons (b) for skin thicknesses of 1.45 mm and 5 mm.*

Figure 2.3. shows the difference between monoenergetic DgN in the cases where the skin thickness is 2, 3, 4 or 5 mm, with respect to using a value of 1.45 mm. A thicker skin corresponds to lower DgN values for energies lower than 38 keV (Fig. 2.3a): the difference reduces monotonically as the primary X-ray energy increases (Fig. 2.3b). At 16.8 keV (corresponding to the mean energy of the Mo/Mo mammographic spectra used in the AAPM−TG195), skin thicknesses of 2 mm, 3 mm, 4 mm and 5 mm produce lower DgN(E) by 4%, 11%, 17% and 23% respectively, compared to that obtained with 1.45-mm skin thickness. For energies higher than about 38 keV, a skin thickness of 1.45 mm produces a slightly lower DgN: this difference does not exceed 1.8%, for 5-mm skin thickness (Fig. 2.3b).

Figure 2.4 shows the percentage difference in DgN(E) between the value obtained modeling a breast with a skin layer of 1.45 mm with respect to the reference breast model proposed by Dance (1990) (where an adipose shielding layer is simulated for the skin layer). The data were calculated for a 20% glandular breast with a compressed thickness of 50 mm. From 8 to 20 keV, the former model produces higher DgN values than those obtained for the Dance's model, and the difference decreases monotonically as the photon energy increases up to 20 keV. At 16.8 keV a difference of ~5% can be observed. For higher energies, the latter model produces higher DgN coefficients, with a maximum difference of 2%. The differences in DgN values between these two models do not significantly depend on the breast glandular fraction.

We simulated also the case of an adipose layer of 2 mm inserted between the skin layer and the glandular-adipose homogeneous portion of the breast: the corresponding DgN values differ by less than 10% with respect to those obtained for the Dance's model, for primary photon ranging between 10 keV and 16 keV (breast thickness = 5 cm; glandular fraction = 20%) (fig. 2.5). For higher photon energies, the latter model produces higher DgN but within 2.2%, in the energy range 22−25 keV. A slight dependence of the DgN differences on the breast glandular fraction is present (fig. 2.5), and the underestimation of the former model in the case of 0% glandular breast is not higher than 0.9% for primary energies higher than 16 keV.
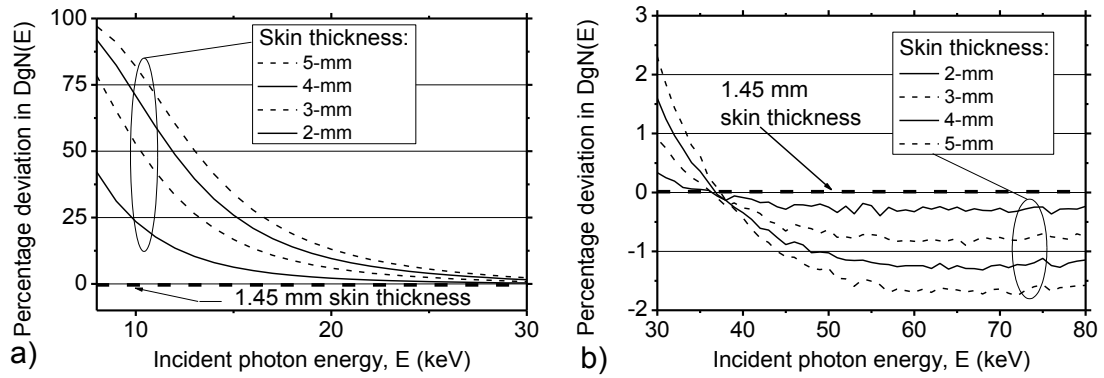
Fig. 2.3. *Percentage DgN deviation in the energy range 8−30 keV in panel (a) and in the range 30−80 keV in panel (b), for a breast with skin layer of 5 mm, 4 mm, 3 mm and 2 mm, with respect to that with a skin layer of 1.45 mm thickness. Glandular fraction = 20%; compressed breast thickness = 5 cm.*
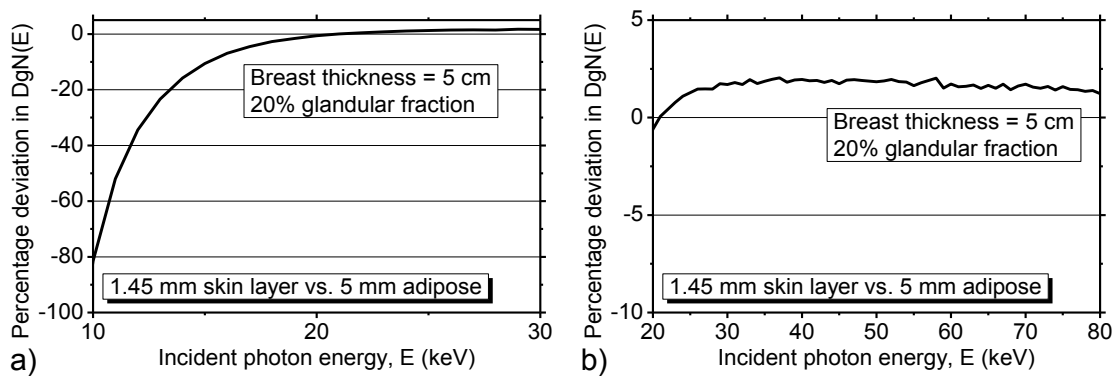
Fig. 2.4. *Percentage difference in DgN coefficients for a breast with a skin thickness of 1.45 mm with respect to that with an adipose layer of 5 mm thickness simulating the skin (ref. values) in the energy range 10−30 keV (a) and in the range 30−80 keV (b).*
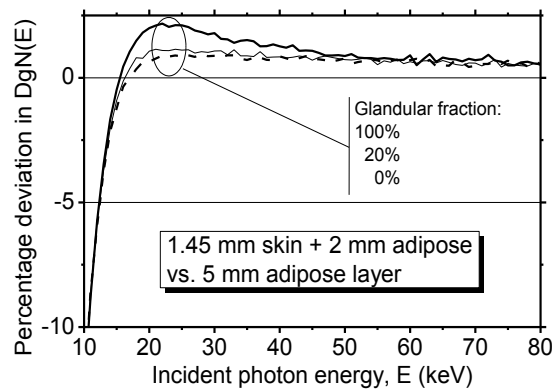
Fig. 2.5. *Percentage difference in DgN coefficients for a breast with a skin thickness of 1.45 mm with an added adipose shielding layer with respect to that with adipose layer of 5 mm thickness proposed by Dance (1990) (ref. values).*

Boone (2002) used a totally homogeneous breast model for the DgN calculation, in which the composition of the skin layer (4-mm thick) is the same used for the breast adipose-glandular tissue mixture. In order to take into account the slight difference in the attenuation coefficients between the skin tissue and the adipose-glandular tissue in the totally homogeneous model, we increased the entrance skin at the entrance beam surface by 2.92 mm and 0.78 mm at 10 keV and 50 keV,

respectively, for 0% glandular breast; it was increased by 112 μm and 96 μm at 10 keV and 50 keV, respectively, for 100% glandular breast. Figure 2.6 shows the difference in DgN for a breast glandularity of 0% and 100%, obtained with the totally homogeneous model with respect to the partially homogeneous model, at 10 keV (fig. 2.6a) and at 50 keV (fig. 2.6b). While the two models do not produce significant differences at 50 keV, at 10 keV the totally homogeneous model has DgN coefficients 80% lower than for the partially homogeneous model (for 0% glandularity), and 8% higher for 100% glandularity.

We simulated either the cases in which the top compression paddle, or the bottom support paddle, or both, are not included in the beam path. Figure 2.7 shows the deviation of monoenergetic DgN coefficients from the case presented in the AAPM-TG195, which considers the two compression paddles. The reference case is the one with both paddles included in the simulation. The difference in DgN(E) calculated without any paddles is negative at energies less than 19 keV (-1.8% at 10 keV); then it increases reaching +2.2% at energies greater than 45 keV. Without the breast support paddle a positive DgN difference up to about 2% can be observed, at energies above 45 keV. The exclusion of the top compression paddle has a limited effect on DgN, with differences not lower than -2% and not higher than +0.5% with respect to the case of both paddles in the beam.
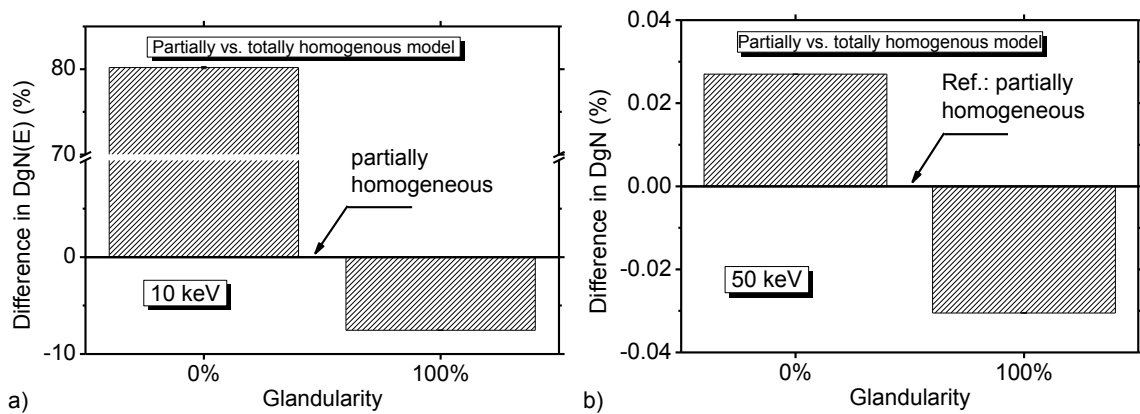
Fig. 2.6. *Percentage difference of the totally homogeneous model with respect to the partially homogeneous model at (a) 10 keV and (b) 50 keV, for a breast thickness of 5 cm and glandular fraction of 0% and 100%.*
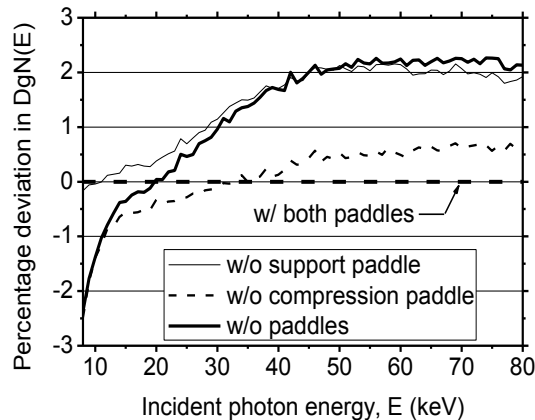
Fig. 2.7. *Percentage difference between DgN(E) values evaluated with both compression paddles to that evaluated without the paddles, or by excluding one of them. Breast glandular fraction = 20%; compressed breast thickness = 5 cm.*

Figure 2.8 shows the influence of the thickness of the top compression paddle, by showing the percentage difference in DgN(E) for thicknesses of 1, 2, 3, 4 or 5 mm, with respect to the case of no compression paddle. Below 35 keV the difference in DgN is positive (i.e. the DgN coefficient with the top compression paddle in the beam is lower than that without the paddle), and monotonically decreasing for any paddle thickness. The difference ranges between +4% at 8 keV and -1% at 80 keV (for a compression paddle of 5 mm thickness). This difference reduces as the thickness of the paddle reduces, down to 1 mm.

Figure 2.9 shows the percentage deviation in DgN(E) evaluated without considering bremsstrahlung processes in the MC simulations with respect to the case in which the electron energy cutoff in the breast tissue is set at 990 eV and the bremsstrahlung processes are simulated. While for 100% glandular breast, no conspicuous differences are present, for lower glandular fraction, the absence of bremsstrahlung processes produced a bias for photon energies higher than 30 keV. However, monoenergetic DgN(E) values produced by excluding bremsstrahlung processes do not overestimate the dose to the breast by more than 1.1% at 48 keV for a 0% glandular breast, this representing a very small effect.
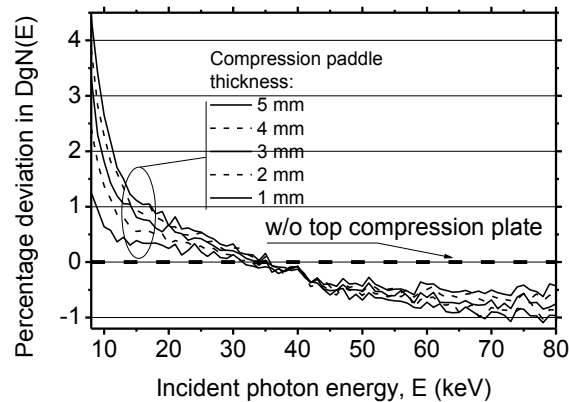
Fig. 2.8. Influence of the thickness of the top compression paddle on DgN(E) for a PMMA paddle thickness in the range 1–5 mm. The percentage difference is evaluated with respect to the case in which the top paddle is not simulated. Breast glandular fraction = 20%; compressed breast thickness = 5 cm.
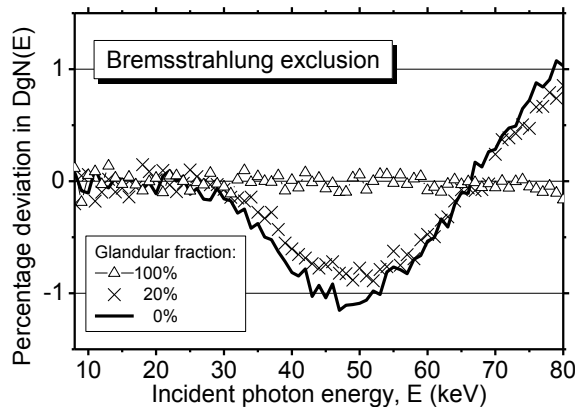
Fig. 2.9. Percentage deviation in DgN(E) from the case in which bremsstrahlung processes are simulated and a low cutoff electron energy is set, for the cases in which the bremsstrahlung processes are not included in the MC simulations. Breast thickness = 5 cm; compression paddles = 2 mm PMMA; skin thickness = 1.45 mm.

Figure 2.10a shows a validation of the heterogeneous breast model (containing a fraction of cubic voxels with glandular tissue, and the remaining fraction with only adipose tissue) for a glandular fraction of 20% and a compressed breast thickness of 5 cm. Here, the MGD per photon was evaluated at 16.8 keV, in successive runs (up to 30 iterations) in which the position of each glandular voxels in the breast volume was varied randomly.

The DgN(E) values were compared with those given by the TG-195 simulations for the corresponding breast model. The MC code with the heterogeneous breast model produced MGD values per photon which varied from run to run with a coefficient of variation of less than 0.4%. Hence, a few runs of the MC code were enough to obtain statistically stable values of the scored quantity. On the other hand, there is a difference (between 4% and 5%) between the values provided by our code and that of the TG-195 report (fig. 2.10a). The percentage difference between the released energy in the breast tissue (both glandular tissue and adipose tissue) for a partially homogeneous model and heterogeneous model was ~0.4% at 16.8 keV, for 5-cm thick breast with a glandular fraction of 20%. Such a difference can be ascribed to the geometrical description with cubic voxels of the half-cylinder volume of the glandular tissue. This effect might be reduced by simulating sub-mm^3 voxels. Moreover, the use of the G factor in the partially homogeneous, as well as in the totally homogeneous breast model, and the use of fitting functions for the evaluation of the mass energy absorption coefficient of the fat and glandular tissues, may introduce a bias in MGD compared to the case of a heterogeneous breast, where the G factor is not employed.

Figure 2.10b shows the difference between the DgN(E) coefficients for heterogeneous breasts compared to homogeneous model (in this case the fitting functions for the evaluation of the mass energy absorption coefficient of the fat and glandular tissues were those provided by Fedon *et al* 2015).
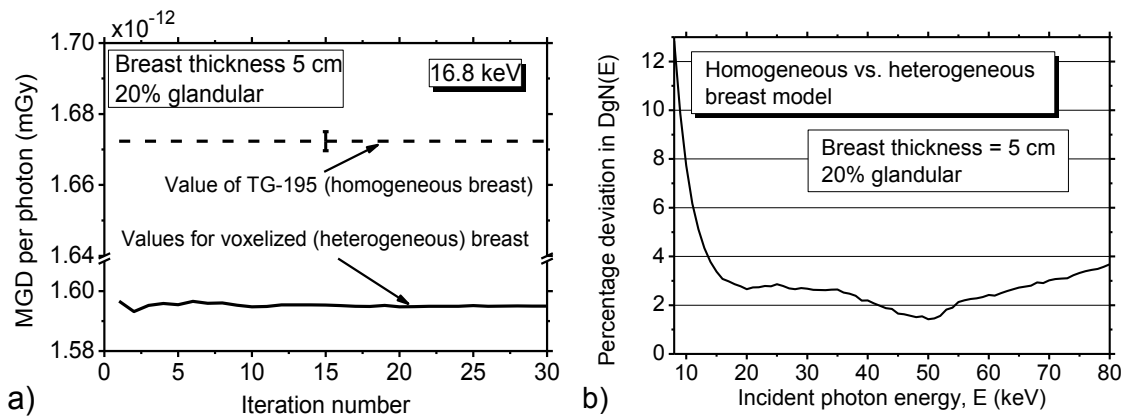
Fig. 2.10. *a) Validation of the voxelized heterogeneous breast model. The MGD per photon (at 16.8 keV) was evaluated in successive runs of the MC simulation, in which the three-dimensional distribution of the voxels containing glandular tissue was changed randomly. The average value and error bar provided by TG-195 is shown for comparison. b) Percentage difference in DgN(E) coefficients evaluated with a heterogeneous breast model to that obtained with a homogeneous breast model.*

The DgN(E) coefficients for the heterogeneous model were computed for five breast models, which differed only for the randomly-selected distribution of glandular tissue voxels. The final DgN values are the average values of the five simulations. In the range 8−80 keV, DgN(E) coefficients computed for the heterogeneous model were lower than for the homogeneous model: the difference was between 1% and 3% for primary photon energies between 15 keV and 50 keV. DgN(E) fluctuations between the five simulations were lower than 0.2% in this range.

2.1.3. Polyenergetic DgN

For Mo/Mo, Mo/Rh and W/Rh spectra, the use of a skin thickness of 4 mm leads to DgN_p underestimation with respect to DgN_p computed for a skin thickness of 1.45 mm (fig. 2.11a) (breast thickness = 5 cm; glandular fraction = 20%). Such an underestimation is lower for harder spectra (W/Rh). In the case of Mo/Mo spectra, the underestimation ranges between 30% at 20 kVp, and 15% at 40 kVp. At 30 kVp, the discrepancies are 19%, 15% and 11% for Mo/Mo, Mo/Rh and W/Rh spectra, respectively. Figure 2.11b shows the DgN_p underestimation obtained by adding a 2-mm thick adipose layer, for a breast with a skin thickness of 1.45 mm. We performed these simulations in order to explore the condition of a thicker skin layer than the above value determined from dedicated BCT scans, since a subcutaneous fat layer might be undetected in such an exam (Huang et al 2008). At all kilovoltages, the addition of the adipose layer produced DgNp values lower than in the case of a sole 1.45-mm thick skin layer. The discrepancies are lower than in the previous case and range between 12% (for Mo/Mo spectrum at 18 kVp) and 2% (for a W/Rh spectrum at 40 kVp). At 30 kVp, the discrepancies are 6%, 4% and 2% for Mo/Mo, Mo/Rh and W/Rh spectra, respectively. In all cases, the discrepancy reduces as the tube voltage increases.
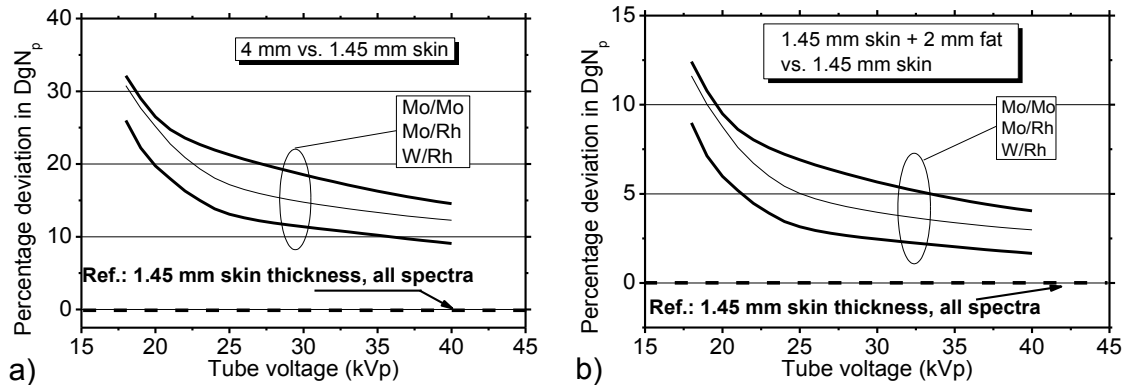
Fig. 2.11. *Percentage deviation of DgNp, evaluated with W/Rh, Mo/Rh and Mo/Mo spectra, for a breast with a skin thickness of 4 mm (a) or a skin thickness of 1.45 mm and an added adipose layer of 2 mm (b) from those obtained with a 1.45 mm skin layer. Glandular fraction = 20%; compressed breast thickness = 5 cm.*

Figure 2.12 shows the effect on the DgN_p values introduced by the inclusion of a 2-mm thick PMMA compression paddle in the simulations of DgN(E). The DgN_p values were computed for the three mammographic spectra, following eq. 2.7. The paddle inclusion in the MC simulation causes a DgN_p underestimation of less than 1.5 %.

Figure 2.13a shows the DgN_p reported by Nosratieh et al (2015), for a breast with a skin thickness of 4 mm, a compression paddle of 3 mm of polystyrene and no bremsstrahlung processes in the simulations; the spectra are tuned by an added layer of PMMA in order to match the given HVL. For comparison, this figure shows the DgN_p computed with our code including a supporting paddle of 2 mm and by inclusion of the bremsstrahlung processes. In this latter case, the spectra are tuned by an added Rh layer and the compression paddle is not included in the monoenergetic simulations (2 mm of PMMA are included in the spectra computation). The shielding layer surrounding the breast is simulated as either a 1.45 mm thick skin layer and an added adipose layer of 2 mm, or by excluding such an adipose layer. The HVL is that obtained below the compression paddle. The DgN_p are those for a breast thickness of 5 cm, W/Rh spectra and 0% and 100% glandular fraction. Figure 2.13b shows the difference between corresponding curves plotted in fig. 2.13a. The reference values are those obtained by Nosratieh et al (2015). In the case in which the skin layer is modeled as 1.45-mm thick skin tissue, the DgN_p values are higher than the reference values at any tube voltages; the discrepancies are comprised between -19% (at 26 kVp) and -4% (at 34 kVp). Including an adipose layer between the skin and the breast tissue reduces the DgN_p values (fig. 2.13a). In this last case, the DgN_p for the W/Rh spectra are higher than those provided by Nosratieh et al (2015), with a discrepancy comprised between −15% (at 26 kVp) and −3% (at 34 kVp). We note that our MC code was previously validated (within 0.2% agreement) (Sarno et al 2016b) versus the data provided by Boone (2002), which provided the monoenergetic $DgN(E)$ data used in Nosratieh et al (2015).
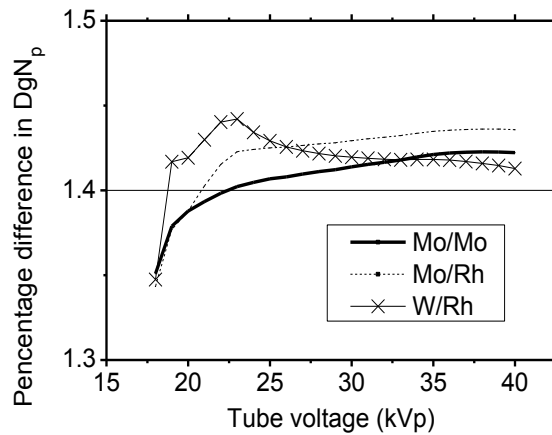
Fig. 2.12: *Percentage deviation of DgN_p, (for W/Rh, Mo/Rh and Mo/Mo anode/filter combinations), as a function of the tube voltage, calculated including the compression paddle (2 mm thick PMMA paddle) in the monoenergetic DgN simulations with respect to those computed without the compression paddle. Skin thickness = 2 mm; glandular fraction = 20%; compressed breast thickness = 5 cm.*
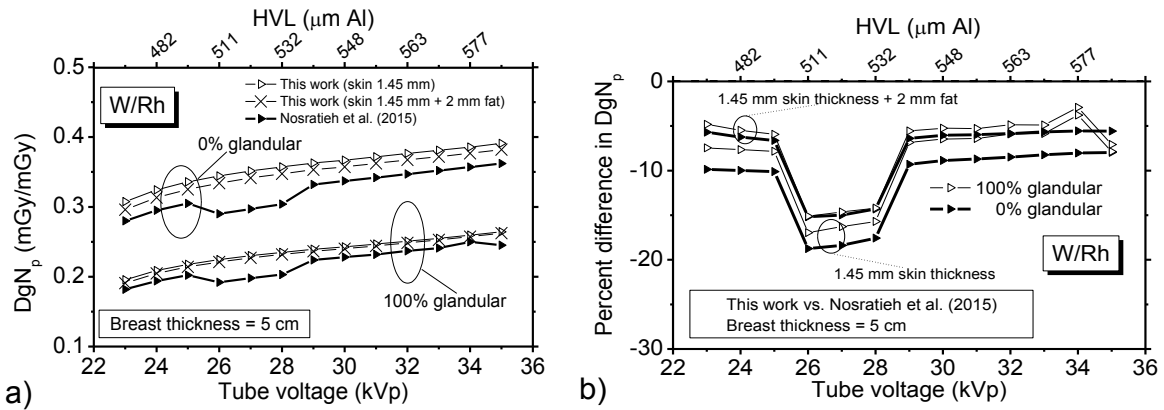
Fig. 2.13. *a) DgN$_p$ for 0% and 100% glandular tissues, for W/Rh spectra from Nosratieh et al (2015) (skin thickness = 4 mm; compression paddle = 3 mm; spectra shape tuned via PMMA thickness; bremsstrahlung excluded) and for a breast with a skin thickness of 1.45 mm, a PMMA supporting paddle of 2 mm (without compression paddle) by including the bremsstrahlung processes in the simulation and both with and without 2 mm of adipose layer between the skin and the glandular-adipose tissue homogeneous mixture. b) The data in (a) are replotted as percentage difference of DgN$_p$ obtained with a skin thickness of 1.45 mm, with and without 2 mm adipose layer with respect to the data provided in Nosratieh et al (2015).*

2.1.4. Air kerma calculation in DgN

In order to study the influence of the photon incident angle θ_i on the air kerma calculation, four irradiation geometries have been simulated and summarized in fig. 2.14:

a) 140×260 mm^2 wide parallel beam; compression paddle included (fig. 2.14a);

b) isotropic half-cone beam source placed at 595 mm from a 50 mm thick breast upper surface and electronically collimated in order to irradiate a 140×260 mm^2 surface at 15 mm beyond the breast bottom surface; compression paddle excluded (semi-aperture of the x-ray beam = 12 deg) (fig. 2.14b);

c) isotropic half-cone beam source placed at 595 mm from a 50 mm thick breast upper surface and electronically collimated in order to irradiate a 140×260 mm^2 surface at 15 mm beyond the breast bottom surface; compression paddle included; paddle thickness in the range 1−5 mm (fig. 2.14c);

d) isotropic half-cone beam source placed at 595 mm from a 50 mm thick breast upper surface and electronically collimated in order to irradiate a 140×260 mm^2 surface at 15 mm beyond the breast bottom surface; compression paddle included; breast excluded; patient body excluded (fig. 2.14d).

In this evaluation, differently from the previous sections, the scoring region is a square of 30×30 mm^2 placed at 60 mm from the chest-wall, as adopted in European QA guidelines (European Commission 2006).
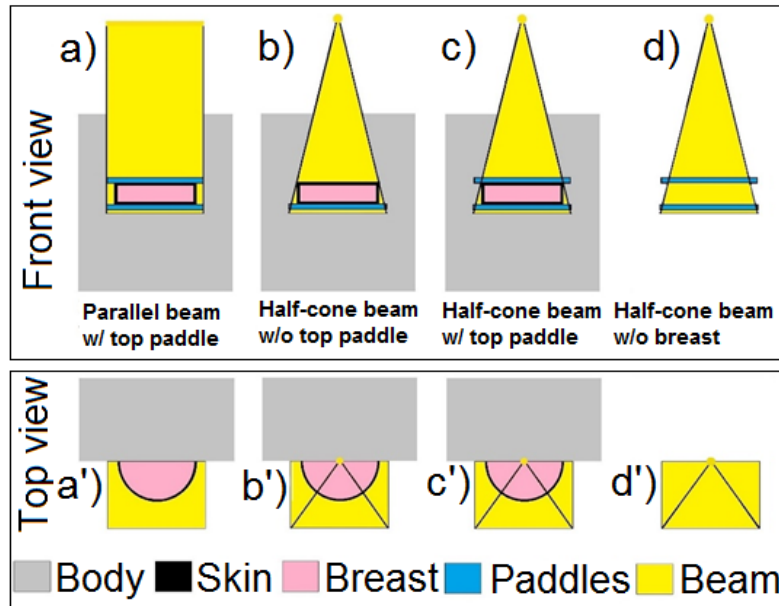
Fig. 2.14. *Sketch of the breast irradiation geometries explored in this work: parallel beam with compression paddle (a-a'); half-cone beam without (b-b') and with (c-c') compression paddle; half-cone beam with compression paddle and without breast in place (d-d').*

Figure 2.15 shows the ratio between K_{air} and K_{air}^{θ} for the irradiation geometry represented in fig. 2.14a, as a function of photon energy. In this test the breast is in place and a mono-energetic and parallel x-ray beam was employed in order to take into account exclusively the contribution due to the scatter from the compression paddle, and not that due to the beam divergence. A ratio K_{air}/K_{air}^{θ} of unity indicates that forward scatter from the paddle and backscatter from the breast has no effect on the calculation of the incident air kerma, while values less than 1 indicate that there is an underestimation in the evaluation of the incident air kerma if one does not take into account the $cos\theta$ factor in eq. 2.5. Figure 2.15 shows that as regards the sole influence of scatter contributions and disregarding the divergence of the source beam, K_{air}^{θ} is greater than K_{air} by as much as 7.2% at 10 keV, and 14.2% at 50 keV.
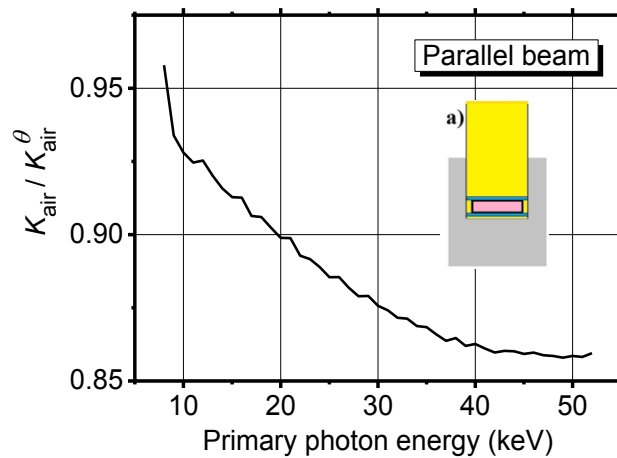
Fig. 2.15. *The ratio between the air kerma values evaluated with eq. (2.4) and (2.5), respectively, as a function of photon energy. Parallel beam geometry, source to scoring surface distance = 595 mm, compression paddle thickness = 2 mm. The inset refers to geometry a) in fig. 2.14a.*

21

Figure 2.16a shows the frequency distribution of the photon incidence angle on the air kerma scoring surface, with both the breast and the top compression paddle in place (fig. 2.14c). The half-cone beam irradiation was simulated at 16 keV, a photon energy close to the average value for typical spectra used in x-ray mammography. Being the scoring region placed at 60 mm from the chest-wall, the incidence angle of the primary photons, which do not interact in any material before impinging on the scoring surface, is comprised between 4.3 deg and 7.5 deg: such photons cause the prominent peak in figure 2.16a. On the other hand, scattered photons spread out over a larger angular range up to 90 deg with respect to the direction normal to the top paddle surface. The scatter frequency (fraction of scattered photons per unit angle) is less than about 1/300th of the corresponding frequency for primary and forward-peaked scattered photons. Integrating this curve for scattering angles greater than 7.5 deg shows that scattered photons contribute less than 8% of the total number of photons reaching the breast surface.

Figure 2.16b shows K_{air}^{θ} per 10^9 generated photons as a function of the incidence angle on the scoring surface, for the Mo/Mo spectrum at 25 kVp (average photon energy = 16 keV). For comparison, the same MC calculation was performed with a 16 keV mono-energetic spectrum. No significant differences between the mono-energetic and poly-energetic case can be noticed.

Figure 2.17 shows the scored air kerma per unit angular interval (divided by the number of generated photons) as a function of the angle θ, for MC calculated values of K_{air}^{θ} and K_{air}. These two quantities have been evaluated for the geometry represented in fig. 14c and for the mono-energetic x-ray beam at 16 keV. The largest differences in the two quantities occur for values of θ larger than about 15 deg, where the factor ($1/cos\theta$) in eq. 2.5 is relatively large. The area under each curve is the total incident air kerma per one billion source photons, and their ratio $\{\sum_i[\Delta K_{air}^{\theta}(\theta_i)/\Delta\theta]\bullet\Delta\theta) / \sum_i(\Delta K_{air}(\theta_i)/\Delta\theta]\bullet\Delta\theta)\}$ is 1.11, indicating that in the calculation of the incident air kerma, using eq. 2.4 rather than eq. 2.5, may produce an underestimation of 11% in the incident air kerma and a corresponding overestimation of 11% for the DgN values.
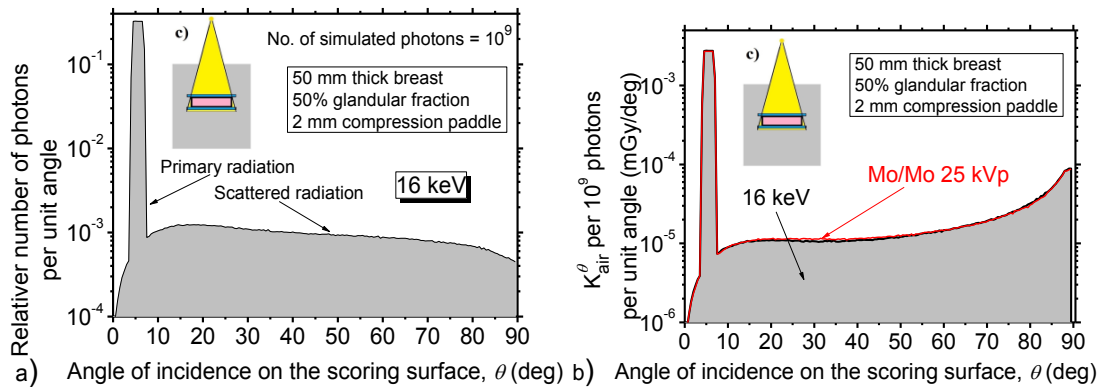
Fig. 2.16. *a) Frequency distribution of the angle of incidence on the scoring surface. b) Air kerma per 10^9 generated photons as a function of the incidence angle on the scoring surface, evaluated according to eq. (2.5). Breast thickness = 50 mm; breast glandularity = 50%; compression paddle thickness = 2 mm; mono-energetic half-cone beam at 16 keV. The angular bin size is 0.5 deg.*
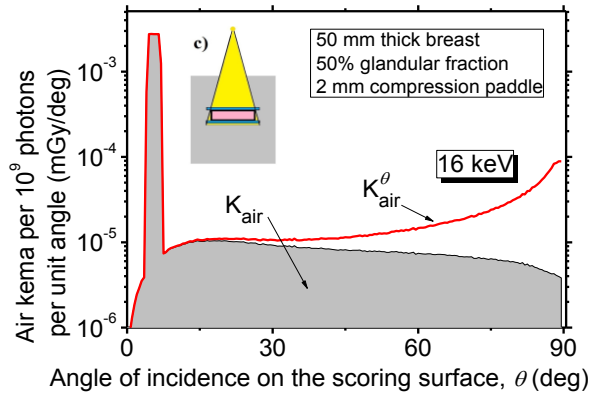
Fig. 2.17. *Air kerma per 10^9 generated photons as a function of the incident angle on the scoring surface, evaluated according to eq. 2.4 (K_{air}) or according to eq. 2.5 (K_{air}^θ).*

Figure 2.18 shows the ratio between the K_{air} and K_{air}^θ for the three cases represented in figs. 2.14b-d. When the compression paddle is not included in the simulated geometry, the x-ray half-cone beam divergence (the same for all mono-energetic beams) leads to a constant ratio of 0.997, on average. On the other hand, when the top paddle is present, K_{air} is always less than K_{air}^θ, with values of the ratio decreasing with increasing energy, and with a maximum deviation of about 14% ($K_{air}/K_{air}^\theta \cong 0.86$) with both the compression paddle and the breast in place.
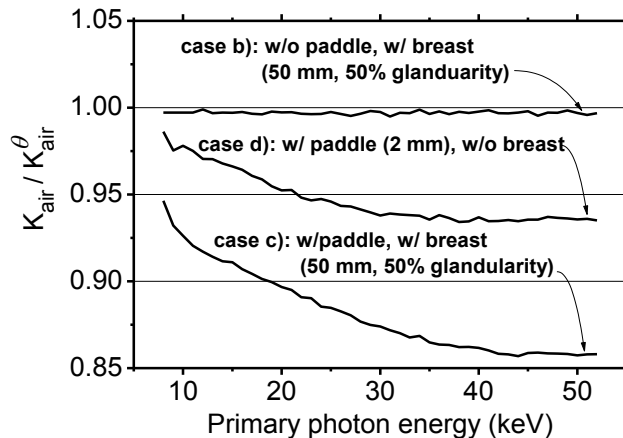
Fig. 2.18. *The ratio between the air kerma values evaluated with eq. (2.4) and (2.5), respectively, as a function of photon energy. Cone beam geometry, source to scoring surface distance = 595 mm, compression paddle thickness = 2 mm.*

The inclusion of a 2 mm thick PMMA compression paddle introduces a contribution due to the scattered photons: in this case the ratio K_{air}/K_{air}^θ goes from 0.978 to 0.936 from 10 to 50 keV, respectively, indicating an air kerma (and then, a DgN) underestimation between 2.2% (at 10 keV) and 6.4% (at 50 keV). The backscattered photons generated from the patient tissues (either the body or the breast) and impinging on the upper face of the scoring surface represent an additional factor to take into account for the air kerma calculation. As shown in fig. 2.18, the contribution due to the breast produces an underestimation in the range from 7.4% (at 10 keV) to 14% (at 50 keV).

In sect. 2.1.2, we showed that a compression paddle thickness increasing from 1 mm to 5 mm introduces a weak influence on the MC estimation of mono-energetic DgN when the calculation of the incident air kerma is carried out using eq. 2.4. On the other hand, figure 2.19 shows the deviation (i.e., the ratio from the considered reference case) in the case in which eq. 2.5 is employed in the calculation of DgN(E). It increases significantly as the thickness of the compression paddle increases, in the range 1−5 mm, due to the increasingly larger contribution of photon scattered in the paddle material. The largest deviation occurs at photon energies close to 45 keV. For a 2 mm thick paddle the relative DgN(E), calculated with respect to the case of no paddle in the beam, is 0.934 at minimum, while for a thickness of 5 mm it reaches a minimum value of 0.882, which indicates a difference as large as 11.8%.
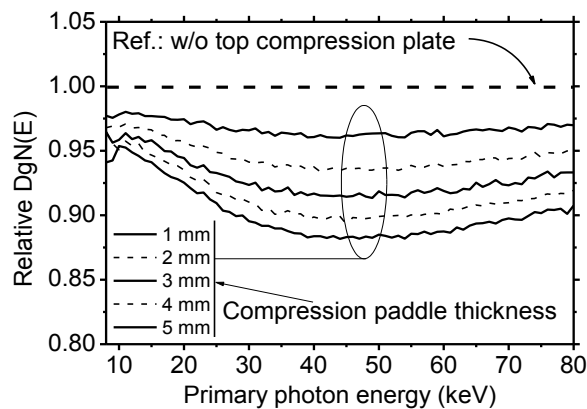
Fig. 2.19. Influence of the thickness of the top compression paddle on the MC calculation of DgN(E) for a PMMA paddle thickness in the range 1−5 mm when the incident photon angle on the scoring surface is considered in the air kerma calculation. The deviation is evaluated as the ratio to the results obtained without the top paddle. Breast glandular fraction = 20%; compressed breast thickness = 5 cm: cone-beam irradiation. The breast was in place in the beam path when evaluating the glandular dose and the incident air kerma.

2.2. Partial irradiation in 2D breast imaging

Partial irradiation in mammography is routinely used during diagnostic work-up of screening or clinical findings, especially in the case when breast undergoes spot compression. In this X-ray imaging modality, only a portion of the breast is compressed and directly irradiated by the X-ray beam. Although spot mammography can be performed with the breast in contact with the detector (usually adopting a small air gap), a larger air gap with a magnification factor of about 1.5 is commonly used.

This section aims at investigating, via MC simulations, the effects of model parameters (breast diameter, shape of the compressed breast, distance between the source and the breast, position of the irradiated area) on the estimates of glandular dose to the breast in partial irradiation in mammography, where only a portion of the breast is imaged. In addition, results obtained with homogeneous breast models (where the breast is simulated as a homogeneous mixture of glandular and adipose tissue surrounded by a skin layer) have been compared to those obtained using breast models with realistic glandular tissue distributions developed from breast CT images.

2.2.1. Dosimetric parameters

In the case of partial volume irradiation, one has to take into account the energy (E_V) absorbed in the directly irradiated glandular breast mass (M_V) as well as the energy absorbed in the not-directly irradiated portion of the breast (E_S) due to scattered photons. Hence, for the MGD (the ratio between the total energy absorbed in the glandular tissue, E_T, and M_T) the following formula can be adopted:

$$\text{MGD} = \frac{E_T}{M_T} = \frac{E_S + E_V}{M_T}. \tag{2.9}$$

Mettivier *et al* (2015), in their investigation of partial irradiation of the breast with a thin laminar beam from a SR source, defined the quantity:

$$\text{MGD}_V = \frac{E_V}{M_V}. \tag{2.10}$$

In this case, only the glandular mass directly irradiated M_V is taken in account, so leading to larger values than those obtained with the eq. 2.9, in particular for small volume irradiation (Mettivier *et al* 2015). The MGD_V was introduced for the first time for the partial breast irradiation in magnification mammography by Liu et *al* (1995) and investigated by Koutalonis *et al* (2006).

An approximate method of estimating MGD for magnification view spot compression has been proposed in Report 89 of IPEM (2005) and is also included in this study. This approximation is denoted MGD_M and is defined as:

$$\text{MGD}_M = \frac{E_{FF}}{M_T} \times \frac{A_I}{A_F} \tag{2.11}$$

where E_{FF} is the energy absorbed for a full-field irradiation, M_T is as defined for eq. 2.9, A_I is the directly irradiated area at the mid-plane of the breast and A_F is the area of the compressed breast. For

the present calculation this has been taken as 226.19×10^2 mm^2, the area of a compressed breast modeled as a cylinder with a semi-circular cross section with a radius of 120 mm (see below). This approximation involves the use of the conventional full-field estimate of MGD. It permits the use of commonly-adopted whole-breast MGD estimates and avoids the calculation of new DgN coefficients, since the MGD in spot mammography would be obtained by simply calculating the ratio of the irradiated area to the whole breast area. For each definition, the normalized glandular dose coefficients (DgN, DgN$_V$, and DgN$_M$, in mGy/mGy) are evaluated by dividing the values of the respective absorbed doses in eqs. 2.9–2.11 by the incident air kerma (K_{air}) at the entrance skin surface.

2.2.2. Monte Carlo simulations

The results of this section were carried out via the MC code presented in the sect. 2.1. The electrons were not tracked but assumed to deposit their energy locally at the point of X-ray interaction. Default cutoffs and step size were used. The dose absorbed in the breast tissue was evaluated following eq. 2.1. K_{air} was evaluated under the compression paddle, in a square region of interest (S) of area 8×8 mm^2 at the entrance breast skin surface attached to the chest-wall using eq. 2.5. Differently from the previous section, the angle between the photon direction and the vector normal to the scoring plane is included in the calculation in order to take into account the large angle photons scattered into the compression paddle which has been outlined of great influence in the sect. 2.1.4. In the evaluation of K_{air}, both primary radiation and scatter from the compression paddle were taken into account, but backscatter from the breast was not included.

Simulations with monoenergetic X-ray beams were performed with photons in the energy range of 8–45 keV. Polyenergetic normalized glandular dose coefficients were evaluated for a W/Rh (Rh filter thickness of 0.050 mm) mammographic spectrum at 28 kVp (1st HVL below 2 mm PMMA compression paddle = 0.511 mm Al) modeled following Hernandez and Boone (2014). The statistical uncertainty achieved in all simulations was below 0.2%.

In the case of simulations with voxelised breasts (see sect. 2.2.3), two validation tests were performed. First, the code was also validated against the AAPM – TG195 Report case 3 (Sechopoulos *et al* 2015). For this comparison, the Report geometry was replicated, but with the breast represented as a voxelised breast of semi-circular cross section with a voxel size of $0.5 \times 0.5 \times 0.5$ mm^3. All voxels representing breast tissue, excluding skin, were composed of a homogeneous mixture of adipose and glandular tissue with the appropriate glandular fraction.

As a second validation of simulations with voxelised breasts, a set of 10 heterogeneous breasts was created by randomly assigning each voxel representing breast tissue as either fully glandular or adipose voxels. The number of glandular voxels in each phantom was set according to eq 2.8. The MC simulations results obtained with the 10 different phantom realizations were averaged and compared to the results of using the homogeneous breast model (breast diameter = 120 mm, full-field breast compression, breast thickness = 50 mm, compression paddle dimension = 90×90 mm^2,

see below). The simulations were performed for W/Rh spectra and tube voltage ranging between 18 kVp and 40 kVp.

2.2.3. Breast models and irradiation geometry in spot mammography

In the homogeneous model developed in the USA (Wu *et al* 1991,1994), the breast is simulated as a cylinder with a semi-elliptical cross section composed of a homogeneous mixture of glandular and adipose tissue, surrounded by a 4-mm skin layer. The composition of the breast tissues is that proposed by Hammerstein *et al* (1979). Although during spot compression the uncompressed area of the breast is thicker than the compressed area, Liu *et al* (1995) and Koutalonis *et al* (2006) simulated it as a fully compressed breast, with a constant thickness as used in full-field MC simulations (fig. 2.20a). In this work, such a model has been compared to a model which considers a thicker portion of the breast for the uncompressed area with respect to the spot area. For this, a rectangular block was subtracted from the full-field compressed breast to mimic the thinner portion of the breast experiencing the spot compression (fig. 2.20b). In order to evaluate the influence of the breast shape on the absorbed energy, various breasts were modelled with a constant thickness of 30 mm between the compression paddle and breast support table, while varying the uncompressed breast thickness between 30 mm (constant compression thickness) and 70 mm. The breast radius was modified so as to maintain a constant total glandular mass in all cases. In the case of the uncompressed breast thickness of 30 mm a breast radius of 120 mm was adopted. Such a breast radius, larger than that used in for the full-field irradiation (sect. 2.1) is adopted in order to entirely contain a 90×90 mm^2 compression paddle in the breast area.
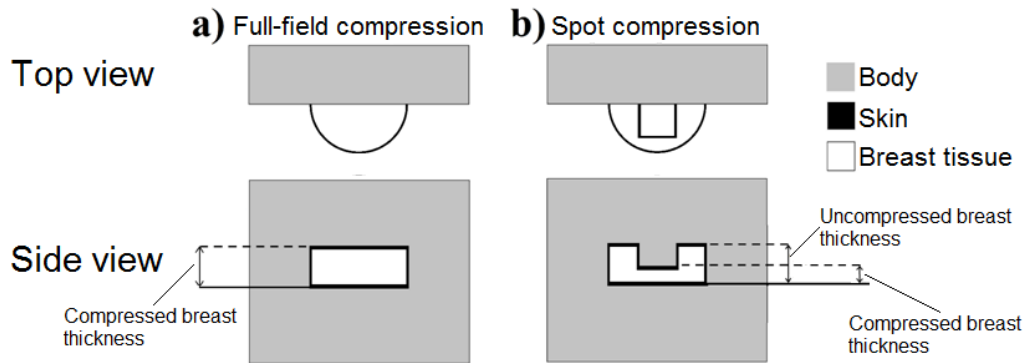
Fig. 2.20. *Schematic of the homogeneous breast model in a) full-field compression and in b) spot compression.*

To study the influence of breast diameter on the glandular dose estimates, the radius was varied between 90 mm and 150 mm (compressed breast thickness = 30 mm; uncompressed breast thickness = 60). In the case of DgN$_M$, E_{FF} was always calculated for a standard breast with a radius of 120 mm. In this work, the breast was modeled as a cylinder with semi-circular cross section, differently from the semi-elliptical cross section adopted in the USA standard (Wu *et al* 1991).

In this work, the patient specific phantoms developed by Sechopoulos *et al* (2012) were used to characterize the difference between dose estimates using the homogeneous simple model breast and

patient specific phantoms. Briefly, Sechopoulos *et al* (2012) used images obtained from dedicated breast CT clinical scans of 20 different breasts to construct voxel phantoms of the pendant breast as imaged in CT. The voxels were classified into four categories: air, skin, adipose and glandular tissue (Yang *et al* 2012) and the phantoms compressed as for a cranio-caudal (CC) mammographic acquisition (Zyganitidis *et al* 2007). Table 2.I shows the mean value, the minimum, the maximum and the standard deviation of the compressed breast thickness, the area and the glandular fraction by mass (skin excluded) of the 20 breasts. The software developed for mimicking the breast compression produces only fully compressed breasts (fig. 2.21a). In order to simulate spot compression, the upper portion of each fully compressed breast (summarized in Table 2.I) was cut out to obtain a breast with a portion compressed to 60% of the thickness of the breast undergoing full field compression (fig. 2.21b).

In order to study the variation in dose with breast geometry, the difference in thickness between the compressed and uncompressed portions was varied as shown in figs. 2.21b, 2.21c and 2.21d. To maintain a constant overall glandular mass when the uncompressed portion of the breast thickness was varied, the increase in glandular mass in the additional uncompressed portion was compensated by removing a portion of breast tissue from the outer part of the breast phantom. Where necessary to ensure a complete layer, a 2.184 mm thick layer of skin (8 voxels), which is the average skin thickness at the upper surface of the 20 3D breast images after compression, was added.

Table 2.I. *Characteristics of the 20 patient specific compressed breast phantoms used in the "fully-compressed" spot dosimetry simulations.*

	Mean	Stand. Dev.	Min	Max
Compressed thickness (mm)	59	15	29	78
Area (mm²)	12,379	5,485	3,111	25,090
Glandular fraction by mass (%)	23.1	15.4	5.0	54.3
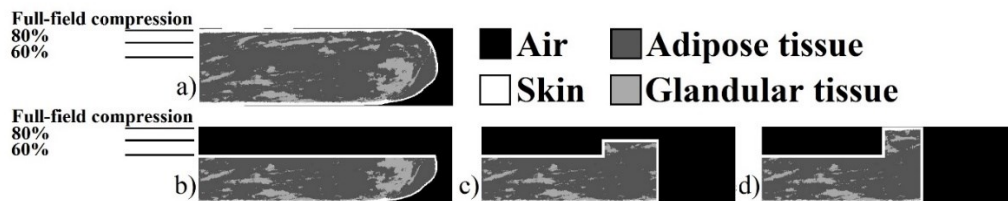
Fig. 2.21. *Sagittal slice of breast n°1 under full-field compression (a), under spot compression to 60% of the thickness of the full-field case and with the uncompressed portion having a thickness of 60% (b), 80% (c) and 100% (d) of the full-field case.*

In the MC simulations, X-rays were emitted isotropically from a point source located 433 mm from the breast support table. Reflecting how clinical systems work during magnification mammography, the X-ray beam was collimated to irradiate a surface at the breast support table as large as the compression paddle. In additional simulations, the effect of varying the distance between

the breast support table and the source was evaluated in the range 343–645 mm, for 50 mm breast thickness, 20% glandular fraction by mass and W/Rh spectrum. Figure 2.22 shows the irradiation geometry.

The compression paddle and breast support table were in all simulations represented as 2 mm thick polymethyl-methacrylate (PMMA) sheets. The breast support table had an area of 140×260 mm^2 while the compression paddle had an area of 90×90 mm^2, as in most modern mammographic systems. In addition, the dimensions of the compression paddle were varied between 10×10 mm^2 and 140×260 mm^2 to investigate the impact of paddle area on dose. In its standard position the paddle was centered laterally and with its center 45 mm anterior to the chest wall. In order to investigate the influence of compression paddle position on dose, its position along the center line of the breast was varied so that the distance between it and the chest-wall was in the range of 0−50 mm. Lateral displacement of the paddle was also investigated with the distance between the center of the paddle and the center line of the breast being varied in the range of 0−70 mm. In all cases, the distance between detector and source was 655 mm. As in the previous section, the patient body was modeled as a water box of volume $300 \times 300 \times 170$ mm^3.
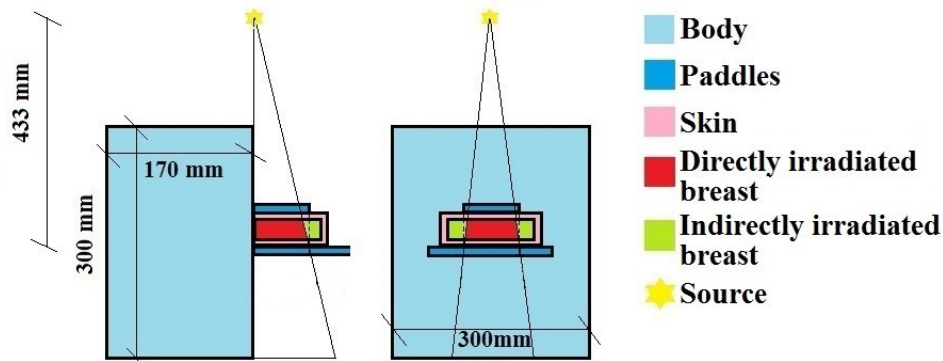
Fig. 2.22. Irradiation geometry used in this work. The isotropic point source is located 433 mm from the breast support table and the X-ray beam is collimated in order to directly irradiate an area on the support table as large as the compression paddle.

In order to compare the dosimetry of the homogeneous breast model to the more realistic patient specific phantoms, we calculated DgN and DgN$_V$ coefficients for the homogeneous breast model and for the patient specific phantoms shown in fig. 2.21a. This version of the patient model was used to avoid introducing artificial glandular tissue distributions due to the removal of the upper portion of the breast representation, resulting in the densest portion of the breasts being located adjacent to the X-ray incident surface of the breast. For the homogeneous breast we used a breast thickness range of 20−80 mm (in 10 mm steps) and glandular fractions of 6%, 12%, 23.1% (i.e. the mean value from Table 2.I), 32% and 42% in the case of 28 kVp W/Rh. The breast radius was 120 mm. The resulting DgN and DgN$_V$ coefficients were then interpolated or extrapolated (on the basis of breast thickness and glandularity) to provide DgN and DgN$_V$ coefficients based on the homogeneous breast model

for each breast summarised in Table 2.I. The resulting coefficients were then compared with those calculated for the same breasts using the corresponding voxelised anthropomorphic breast models.

2.2.4. Normalized glandular dose coefficients

Figure 2.23 shows the ratio between E_V and E_T for varying areas of the directly irradiated breast surface, ranging from 0.78×10^2 mm^2 (for a compression paddle of 10×10 mm^2) to 226.19×10^2 mm^2 (for a full-field irradiation), for a 50 mm thick 20% glandular breast (28 kVp, W/Rh). As expected, the ratio E_V/E_T monotonically increases up to 100% (i.e. the value for full-field irradiation) as the directly irradiated surface increases. For a compression paddle of 90×90 mm^2 (directly irradiated area = 63.37×10^2 mm^2), about 95% of the energy absorbed in the breast glandular tissue is absorbed in the directly irradiated portion. DgN (fig. 2.24a) and DgN$_V$ (fig. 2.24b) values increase as the area of the directly irradiated surface increases.

As expected, using the conventional definition for the glandular dose in spot compression mammography (MGD/DgN) leads to a substantially lower dose value compared to the case when only the directly irradiated part of the breast is taken into account (MGD$_V$/DgN$_V$) (fig. 2.25). Moreover, DgN$_M$ values are lower compared to the other dose estimates defined in this work, at all energies investigated (fig. 2.25). For monoenergetic X-ray beams (energy range 8−45 keV) and a 90×90 mm^2 compression paddle, DgN$_M$ and DgN are more than 60% lower than DgN$_V$ (fig. 2.25b). DgN$_M$ coefficients, which approximate DgN in spot compression mammography, are between 3% and 14% lower compared to DgN in this photon energy range (fig. 2.25b). For W/Rh spectra at 28 kVp, all three normalized glandular dose coefficients increase with increasing compression paddle area, up to the value for full-field irradiation, and are then the same in all cases (fig. 2.26). For a compression paddle area of 90×90 mm^2, DgN$_V$ is about 3 times higher than DgN and DgN$_M$. In the same conditions, DgN$_M$ underestimates DgN by 6.7%. Decreasing the paddle area to 80×80 mm^2 or 50×50 mm^2 (paddle dimensions comprised in the range typically used in spot compression mammography) reduces DgN$_V$ by 0.7% and 3.4%, respectively (fig. 2.26).
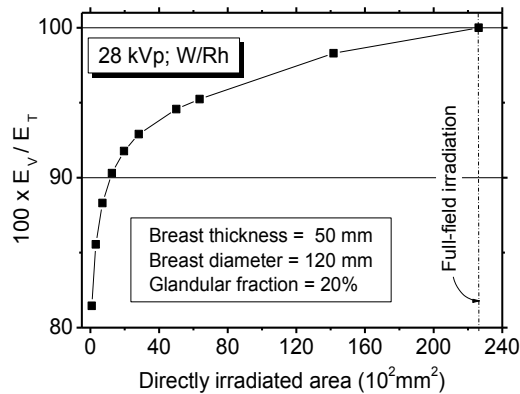
Fig. 2.23. *Percent ratio between E_V and E_T for an irradiated area ranging between 0.78×10^2 mm^2 and 226.19×10^2 mm^2 (full-field irradiation).*
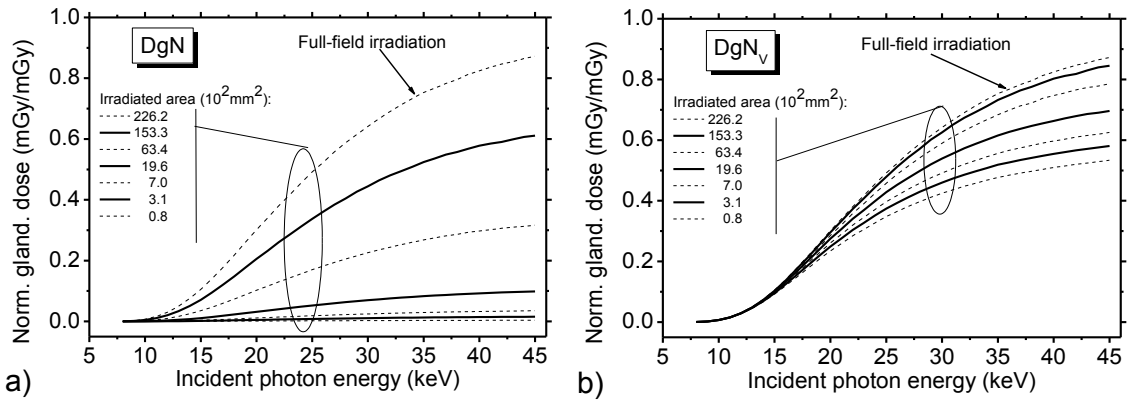
Fig. 2.24. *Monoenergetic (a) DgN and (b) DgN$_V$ for a 20% glandular breast with a thickness of 50 mm (constant thickness compression).*
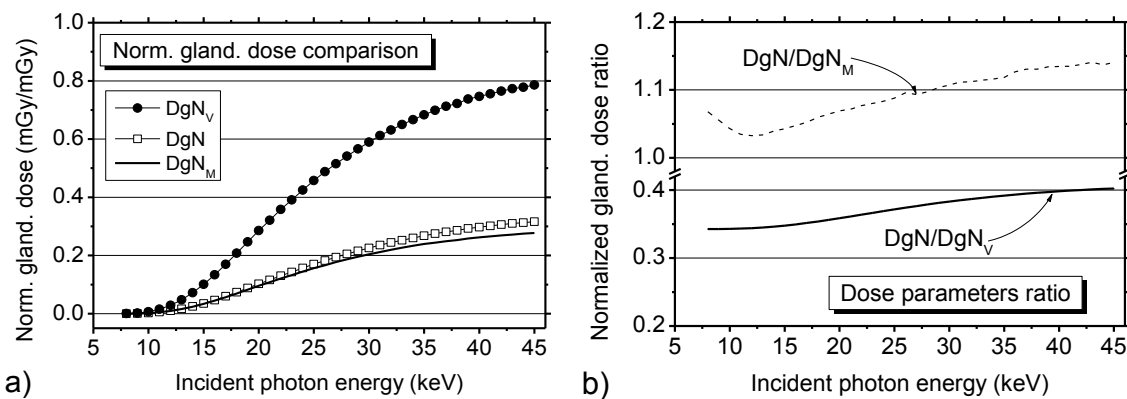
Fig. 2.25. *a) Comparison of the three DgN conversion coefficients for a single breast and compression paddle size and their variation with monoenergetic X-ray energy. b) DgN/DgN$_M$ and DgN/DgN$_V$ ratio. Breast thickness = 50 mm; glandular fraction = 20%; compression paddle area = 90 × 90 mm^2*
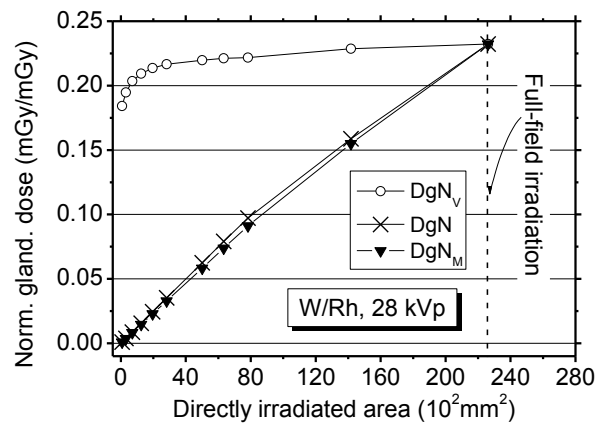
Fig. 2.26. *Polyenergetic DgN, DgN$_V$ and DgN$_M$ for a 20% glandular breast with a thickness of 50 mm (constant thickness compression) for varying compression paddle size.*

Modeling the breast shape under spot compression more realistically, in which the compressed portion is thinner than the uncompressed portion, leads to results essentially the same as those obtained when the uncompressed and compressed regions of the breast are set to the same thickness. Figure 2.27 shows the three dosimetric parameters, for a 20% glandular breast and a breast thickness of 30 mm below the 90 × 90 mm^2 compression paddle. For a W/Rh spectrum at 28kVp, all three

normalized glandular dose coefficients depend weakly on the breast compression shape, as long as the total breast mass is constant. DgN_V for a 28 kVp W/Rh spectrum, remains almost constant, with only a 0.4% increase (MC statistical uncertainty = 0.2%) when increasing the thickness of the uncompressed breast portion from 30 to 70 mm.
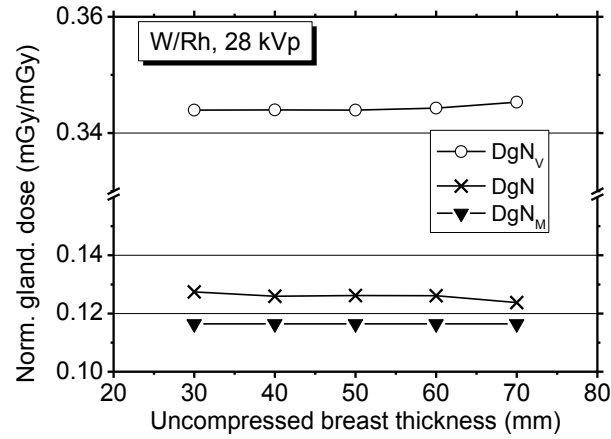
Fig. 2.27. Polyenergetic DgN, DgN_V and DgN_M for a 20% glandular breast. Breast thickness between the paddles = 30 mm; compression paddle = 90 × 90 mm².

As can be seen in Figure 2.28, DgN_V does not depend on the breast radius, and therefore on the overall breast mass, while DgN does. This is in contrast to the behavior of DgN in full-field mammography, where the dependence on breast diameter is considered negligible (Boone 2002) and a standard breast model with a standard diameter is adopted (Dance 1990). For a 20% glandular breast with a compressed thickness of 30 mm and an uncompressed thickness of 60 mm, increasing the breast radius from 90 mm to 120 mm (with the corresponding increase in the breast glandular mass) reduces DgN by 52%. In the same radius range, DgN_V remains constant apart from a small decrease between a breast radius of 90 mm (when the compression paddle is not entirely within the breast surface) and 100 mm.

For a fixed distance between detector and source of 655 mm, DgN and DgN_V increase as the source to the breast support table distance increases and the magnification decreases (fig. 2.29). Reducing the source to the breast support table distance from 645 mm (i.e. spot compression without magnification) to 433 mm (i.e. spot magnification compression with ×1.5 magnification factor) decreases DgN_V and DgN coefficients by 5.7% and 9.3% respectively, for a 20% glandular fully compressed 50 mm breast and W/Rh spectrum at 28 kVp.
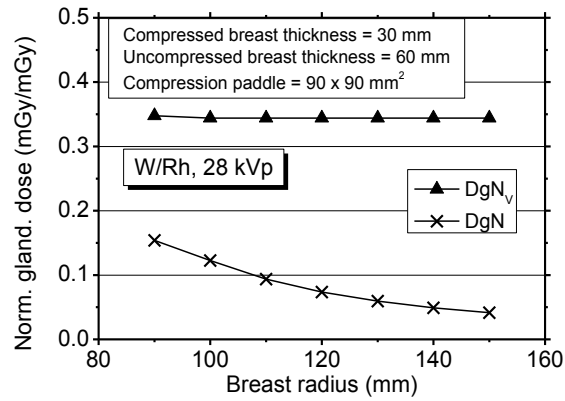
Fig. 2.28. *Polyenergetic DgN and DgN$_V$ for a 20% glandular breast with varying breast radius.*
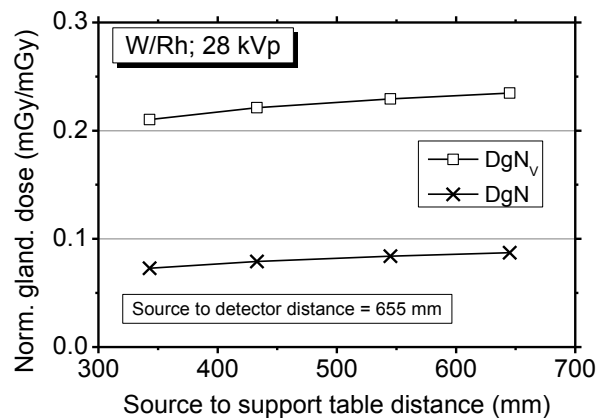
Fig. 2.29. *Polyenergetic DgN and DgN$_V$ at different source to breast support table distances. Breast thickness 50 mm; glandular fraction 20%, breast radius 120 mm, compression paddle area 90 × 90 mm².*

Increasing the distance between the irradiated portion of the breast either from the chest-wall (fig. 2.30) or laterally from the center line of the breast (fig. 2.31) has no influence on normalized glandular dose, unless a portion of the compression paddle extends beyond the breast surface. In this case, both DgN and DgN$_M$ are reduced as the paddle moves away from the chest-wall or from the center line of the breast. Moving the compression paddle from 30 mm to 50 mm from the chest-wall reduces the former by 22% and the latter by 20%. Moving the compression paddle 70 mm from the breast centerline reduces DgN and DgN$_M$ by 11% and 10%, respectively. Under these conditions, a weak increase can be observed in DgN$_V$ of no more than 1.6%.

Figure 2.32 shows DgN (fig. 2.32a) and DgN$_V$ (fig. 2.32b) coefficients evaluated for the homogeneous model in the case of W/Rh spectrum at 28 kVp, for breast thicknesses ranging between 20−80 mm and glandular fractions of 6%, 18%, 32% and 42%. The simulated breast radius is 120 mm and the skin thickness 4 mm.
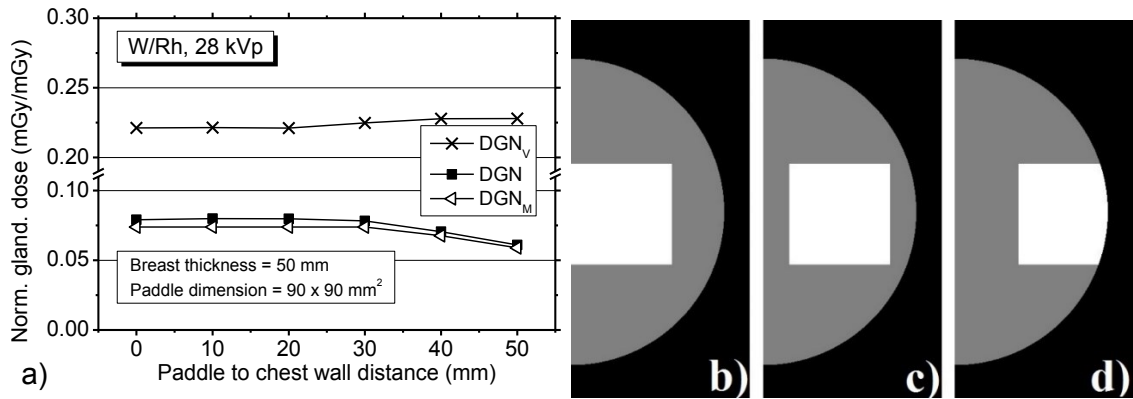
Fig. 2.30. *a) Polyenergetic DgN, DgN$_V$ and DgN$_M$ at different compression paddle – to – chest wall distances. Glandular fraction = 20%, breast radius = 120 mm. Drawing of the modeled breast, in grey, with the direct irradiated area in white for distances between chest wall and compression paddle of (b) 0 mm, (c) 20 mm and (d) 50 mm.*

In the first validation test of the voxelised version of the MC code used in this work, the MGD per photon obtained with this code when assigning all voxels a homogeneous 20% glandular/80% adipose mixture was within -2.2% for the 16.8 keV monoenergetic X-ray beam and +0.3% for the 30 kVp Mo/Mo spectrum of the AAPM TG 195 Report results.

In the second validation, the comparison of a homogeneous breast defined as a simple solid to the voxelised version with random assignment of voxels as fully glandular or adipose (breast thickness = 50 mm; breast radius = 120 mm; glandularity = 20%; compression paddle = 90 × 90 mm², see below), resulted in differences in the normalized glandular dose coefficients lower than 2% for W/Rh spectra in the range 18-40 kVp (1.6% at 28 kVp). In the previous section (Sarno *et al* 2016c) similar results have been shown in the case of full-field breast irradiation. For the second validation, the *G*-factor is used for the homogeneous breast simulation but it is not used for the breast defined as randomly placed fully adipose and glandular voxels. Therefore, any differences in the mass energy absorption coefficients used for calculation of the *G*-factor in the homogeneous case and the coefficients used internally by the MC code to simulate each interaction could introduce differences of this, albeit low, magnitude.
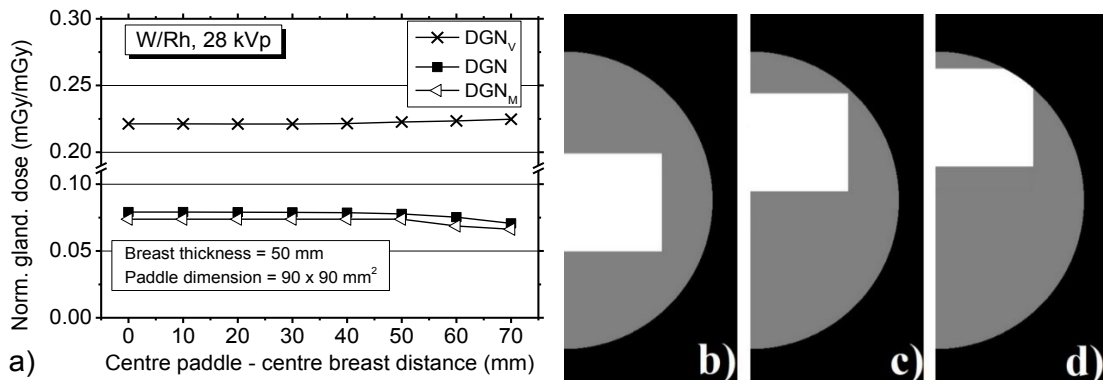
Fig. 2.31. *Polyenergetic DgN, DgN$_V$ and DgN$_M$ at different compression paddle center – breast center distances. Glandular fraction = 20%, breast radius = 120 mm. Drawing of the modeled breast, in grey, with the directly irradiated area in white for distances between the centre of the paddle and the centre of the breast of (b) 0 mm, (c) 50 mm and (d) 70 mm.*

34
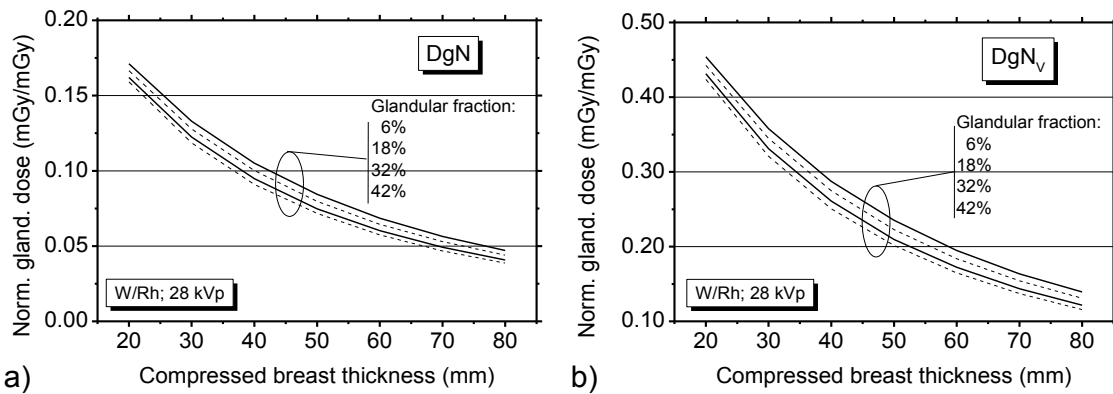
Fig. 2.32. *Polyenergetic (a) DgN and (b) DgN$_V$ obtained for the homogeneous breast model. Compression paddle = 90 × 90 mm²; source to breast support table distance = 433 mm.*

Figure 2.33 shows average DgN$_V$ and DgN values obtained for the 20 patient specific breasts summarized in Table 2.I evaluated for a compression paddle of 90 × 90 mm² with different thicknesses for the uncompressed breast areas. As found for the homogeneous model, the normalized glandular dose coefficients do not vary with the shape of the uncompressed portion of the breast. Therefore, for both simple breast models and for realistic patient breasts, an accurate representation of the relationship between the spot compressed and uncompressed areas of the breast is not needed for dosimetry evaluation.

By comparing the results in Fig. 2.33 to those in Fig. 2.27, it can be seen that the ratio between DgN and DgN$_V$ is different for patient-specific breasts compared to that of the simple breast model. In the patient breasts, the glandular tissue tends to be located towards the center of the breast. The spot being simulated for the results in fig. 2.33 was located close to the center of the breast area, so a higher proportion of the glandular tissue was included within the directly irradiated volume, and most of the energy absorbed outside this volume was in adipose tissue. Therefore, in the case of the patient breasts the denominator in the calculation of DgN and DgN$_V$ does not vary as much as in the case of the simple model, in which the distribution of glandular tissue is uniform across the whole breast.
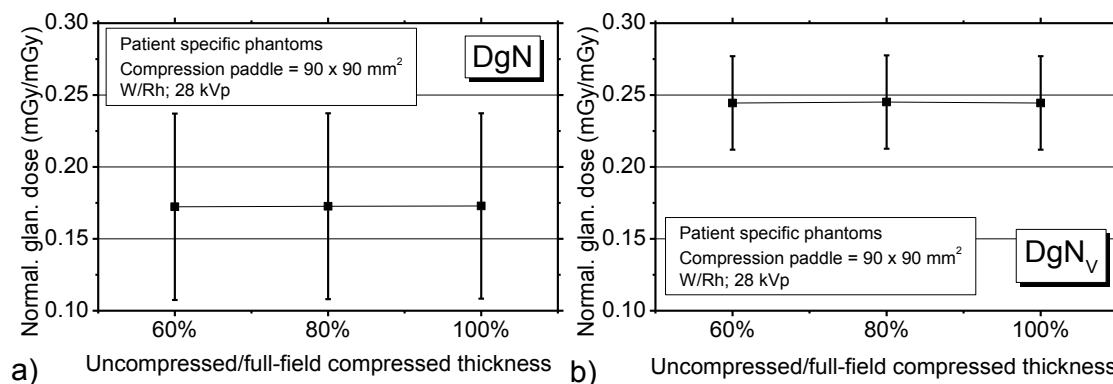
Fig. 2.33. *Average of the polyenergetic a) DgN and b) DgN$_V$ results for the 20 patient specific breasts summarized in table 2.I for a compressed breast thickness between the paddles of 60% of the full-field compressed breast thickness. The error bars were evaluated as the standard deviation of the results obtained for the 20 patient breasts.*

Figure 2.34 shows the ratio between the normalized glandular dose values estimated from the homogeneous model (reported in fig. 2.32) to those obtained by using each of the patient breasts, summarized in Table 2.I. The results are for full-breast compression (as demonstrated above, spot compression does not influence the normalized glandular dose), and a compression paddle of area 90×90 mm^2. The ratios for DgN and DgN$_V$ are (mean $\pm$ 1 SD) 0.54 ± 0.18 and 0.96 ± 0.19, respectively. Therefore, using a simple homogeneous breast model with standardized size and a skin thickness of 4 mm underestimates the MGD to patient breasts by about 50%. As well as the expected influence of using a different skin thickness, the influence of breast area and the spatial distribution of the glandular tissue on DgN in spot mammography introduces important variations that would need to be addressed in future.
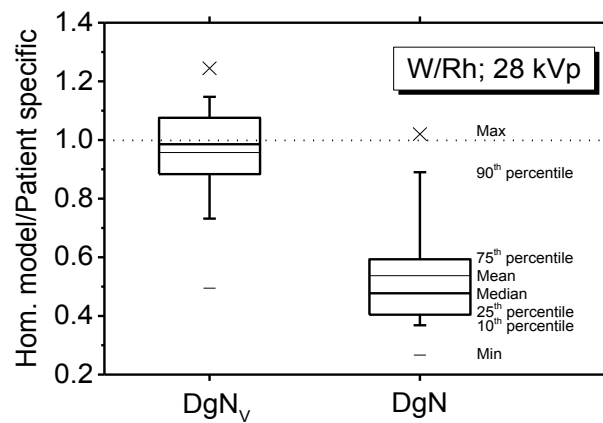
Fig. 2.34. Box-whisker plot of the ratio between the normalized glandular dose obtained with the homogeneous breast model (skin thickness = 4 mm; breast radius = 120 mm) and that obtained with the patient specific breast phantom. W/Rh spectrum at 28 kVp, compression paddle dimension = 90×90 mm^2; $\times 1.5$ magnification.

3. Dosimetry in 3D X-ray breast imaging

This chapter presents investigations which produced the following publications:

- *Sarno et al 2016 Geant4 calculation of normalized glandular dose coefficients in computed tomography dedicated to the breast. Oral presentation at the European Congress of Medical Physics, Athens (Greece) 1st – 4th September 2016*
- *Mettivier et al 2015 Glandular dose in synchrotron radiation breast computed tomography Phys. Med. Biol. 61 569–587*

3.1. Cone-beam CT dedicated to the breast

BCT has been approved by FDA in USA to be used in conjunction with mammography for breast cancer diagnosis. As in the case of 2D imaging of the breast, already discussed in the previous sections, MGD is accepted as the reference dosimetric value. Similarly to the 2D case, conversion factors, the DgN_{CT} coefficients, must be calculated in order to estimate MGD from related measured exposure or incident air kerma, usually measured at the entrance skin surface in mammography (European Commission 2006) and DBT (Van Engen *et al 2016*). In BCT, the air kerma (K_{iso}) is measured at the scanner isocenter (Boone *et al* 2004, Thacker and Glick 2004, Sechopoulos *et al* 2010) and the MGD then evaluated as follows:

$$MGD = DGN_{CT} \times K_{iso} \qquad (3.1)$$

Many authors provided DgN_{CT} coefficients both for monochromatic and polychromatic spectra (Boone *et al* 2004, Thacker and Glick 2004, Sechopoulos *et al* 2010). Sechopoulos *et al* (2010) tabulated the DgN_{CT} coefficients for the FDA approved and CE marked Koning corp prototype (http://koninghealth.com/); these values are calculated for a single spectrum HVL, and they can be adopted only for some Koning units (because the spectra can consistently vary between the different BCT units) and not for BCT setups which adopt different spectra.

This section aims at defining a breast model for DgN_{CT} evaluation and at providing via Monte Carlo (MC) simulations monochromatic DgN_{CT} coefficients ($DgN_{CT}(E)$), in the energy range usually adopted in BCT, both for clinic and research in this field. Moreoever, polychromatic DgN_{CT} ($pDgN_{CT}$) are provided for the BCT setups clinically available. Finally, the results obtained for the proposed breast model are validated vs patient specific digital phantoms.

3.1.1. Monte Carlo simulations

In order to calculate the $DgN_{CT}(E)$ coefficients the same MC code for results in sections 2.1 and 2.2 was adopted. The dose to glandular portion of the breast has been evaluated following eq. 2.1.

K_{iso} was evaluated at the scanner isocenter by scoring the photons in a 20×30 mm^2 placed with the upper edge (20 mm long) at the source height and it was evaluated as in eq. 2.5. However, any source of scatter are avoided, and the factor introduced by the angle between the photon direction and the normal vector to the scoring surface is negligible.

Finally, the $DgN_{CT}(E)$ are calculated:

$$DgN_{CT}(E) \ = \frac{MGD}{K_{iso}} \ .$$ (3.2)

In order to reduce the amount of output data in the final datasheet, the $DgN_{CT}(E)$ were fitted with 8th-order polynomial curves. The zero-order term is forced to 0. The fitting process was implemented with Matlab R2016b with last absolute residual algorithm (LAR). Monoenergetic DgN_{CT} were computed in the photon energy range 5−82 keV.

In order to compare the examined cases, the ratio between two DgN_{CT} coefficients was evaluated as:

$$DgN_{RATIO} = \frac{DgN_X}{DgN_{ref}},$$ (3.3)

where the subscript *ref* indicates the reference value in the comparison.

Both the K_{iso} and the MGD were computed with an uncertainty lower than 0.1%, but for photon energy lower than 8 keV, where an uncertainty between 0.1% and 0.2% was calculated. The uncertainty was evaluated as suggested by Sempau *et al* 2001.

The $pDgN_{CT}$ were computed from the DgN(E) as suggested by Boone (1999) and reported in eq. 2.7. The used spectra are those presented by the Koning corp BCT (Sechopoulos *et al* 2010), produced with a W anode and an added Al filtration. Although in Sechopoulos *et al* (2010) the X-ray beam HVL was assessed to be 1.39 mm Al, the Al filter thickness uncertainty can make such a value to vary among the different BCT units. In order to cover a broader range of spectra, we calculated the pDgN values for HVL ranging between 1.25 mm Al and 1.50 mm Al. The spectra were computed as suggested by Hernandez and Boone (2014). A layer of 2 mm of PMMA was added during the spectra calculation in order to take into account the protective plastic cup, which is present in the BCT units (Sechopoulos *et al* 2010). The HVL was tuned by varying the Al filter thickness.

In the case of patient specific breast phantoms (see sect. 3.1.2), the geometry does not present the symmetry of the homogeneous case, due to the heterogeneous glandular tissue distribution and the arbitrary breast silhouette. This implies that the source had to rotate during the breast irradiation simulating the real scanning geometry. For this reason, a new MC code validation test was carried out. Hence, 10 voxellised cylinders were generated. They presented a diameter of 140 mm, a height of 1.5 times the radius, the skin thickness was 2 mm and a glandular fraction by mass of 20%. The voxel were made either of 100% glandular tissue or of 100% adipose tissue. The glandular voxels were placed randomly within the breast adipose tissue and the 10 different breasts differed by the different glandular distribution. The number of the glandular voxel has been evaluated following eq. 2.8. Finally the MGD, on average over the 10 breast, has been compared to that of a 20% glandular homogeneous breast, in the monoenergetic energy range 8-80 keV. During this validation the source rotated in step-and-shoot mode on a scan angle of 360 deg with a step of 1 deg.

3.1.2. Breast model and irradiation geometry

The breast was modelled as a cylinder composed of a homogeneous mixture of glandular and adipose tissue surrounded by layer simulating the skin. The composition of the skin and the homogeneous breast tissue are those reported in Boone (1999). The skin thickness was 1.45 mm thick (Huang *et al* 2008); moreover the effect of modifying the skin thickness on the DgN_{CT} has been investigated. The DgN_{CT} coefficient have been evaluated for breast diameter in the range 80−180 mm (with 20 mm step), for glandular fraction by mass of 0%, 14.3%, 25%, 50%, 75% and 100% and for breast height equal to 1, 1.5 and 2 times the breast radius. The chest wall was modelled as a water box of $300{\times}300{\times}150$ mm^2.

The irradiation geometry of the Koning corp. apparatus was replicated. The radiation source was placed at 650 mm from the isocenter and the isotropic X-ray cone beam was electronically collimated in order to irradiate a $400{\times}300$ mm^2 flat panel detector at 923 mm from the source (fig. 3.1). The distance between the chest-wall and the X-ray central beam (i.e. the ray which impacts perpendicular to the detector) was 0 mm, as already proposed by Sechopoulos *et al* (2012) in order to cover the entire breast during the scan. Such a distance is justified by the breast entire coverage shown for the Koning apparatus (O'Connell *et al* 2010). However, since Boone *et al* (2004) proposed to use a distance of 20 mm, the influence of this parameter on the DgN_{CT} was investigated in this work.
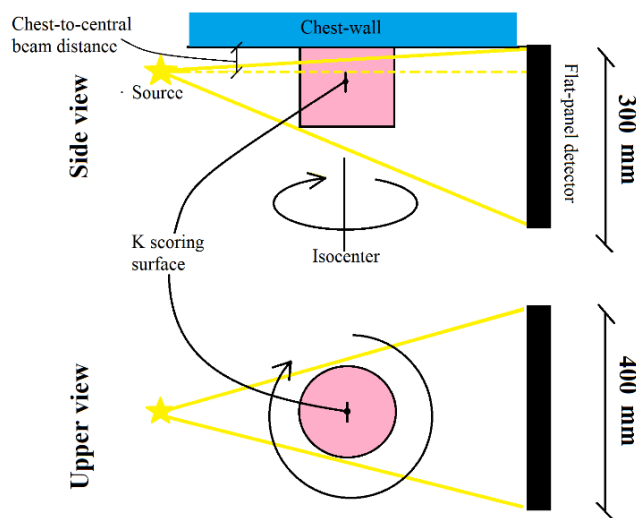
Fig. 3.1. *Irradiation geometry adopted in this work*

Since the glandular distribution has been shown to represent an issue in MGD estimation in mammography, the DgN_{CT} coefficients evaluated for the homogeneous breast model are compared to those obtained for patient specific digital phantoms (fig. 3.2). In order to obtain these coefficients, 20 3D images of uncompressed breasts have been acquired via a BCT scanner (Sechopoulos *et al* 2010). The image voxels in the CT slices ($0.273{\times}0.273{\times}0.273$ mm^3) were classified into four categories: air, skin, adipose and glandular tissue (Yang *et al* 2012). These patient specific breast phantoms have been already presented in sect 2.2. Table 3.I summarizes the glandular fractions (by

mass), the length and the equivalent diameters at the chest wall of the patient specific breasts. The glandular fraction differences between tab. 2.I and tab. 3.I can be ascribed to the influence of the compression software employed in the first case. The breast diameter at the chest wall have been computed from the breast area in the 70-th coronal slice from the chest (at about 20 mm from the chest). They were irradiated with a W spectrum with an HVL of 1.40 mm Al, from 300 equally spaced angles over 360 deg scan angle. The polyenergetic DgN_{CT} coefficients obtained for the homogeneous model were linearly interpolated or extrapolated on the basis of the glandularity, diameter and length of the patient specific breast phantoms in order to be compared.
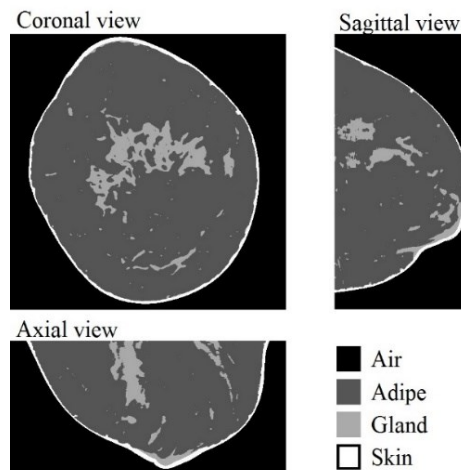
Fig. 3.2. *Coronal, sagittal and axial views of the patient specific breast phantom[1].*

Table 3.I. *Characteristics of the patient specific breast phantoms.*

	Mean	Std. Dev.	Min	Max
Glandular fraction by mass (%)	28.0	22.6	4.9	76.0
Diameter (mm)	112	21	64	146
Length (mm)	90	28	46	161

Figure 3.3 shows the ratio between the monoenergetic DgN_{CT} evaluated for a chest-wall to central X-ray beam of 20 mm and those evaluated for a distance of 0 mm or 10 mm. In all cases, the K_{iso} scoring region was placed with its upper edge at the height of the central beam axis. The comparison was performed in the energy range 10-60 keV, for a breast with a diameter of 140 mm, height equal to 1.5 times the radius and a glandular fraction of 20%. Setting a distance between the patient chest and the central X-ray beam of 10 mm instead of 20 mm produces DgN_{CT} values down to 3.3% lower.

---

[1] These digital breast phantoms have been courteously provided by prof. Ioannis Sechopoulos (Radboud UMC, Njmegen, The Netherlands).

It reduces to 3%, on average, for photon energies higher than 20 keV. A similar trend can be noticed if the chest-to-central beam distance is set to 0 mm instead of 20 mm. In this case, the percent difference is in the range 5.0%−6.4%.

In mammography, the modelled breast skin drastically influenced the estimated MGD (sect. 2.1, Sarno *et al* 2016c). In BCT, where the photon energies are higher than in mammography, such an influence is lower (fig. 3.4). For the case of a 20% glandular breast with a diameter of 140 mm and height of 1.5 times the radius, modelling the skin layer of 4 mm thick (as in the USA mammographic protocols, Wu *et al* 1991) instead of 1.45 mm leads to a $pDgN_{CT}$ decrease of 4.8% for 49 kVp and HVL of 1.25 mm Al. The higher is the HVL the lower is this difference. It reduces to 4.3% for HVL of 1.50 mm Al (fig. 3.4).
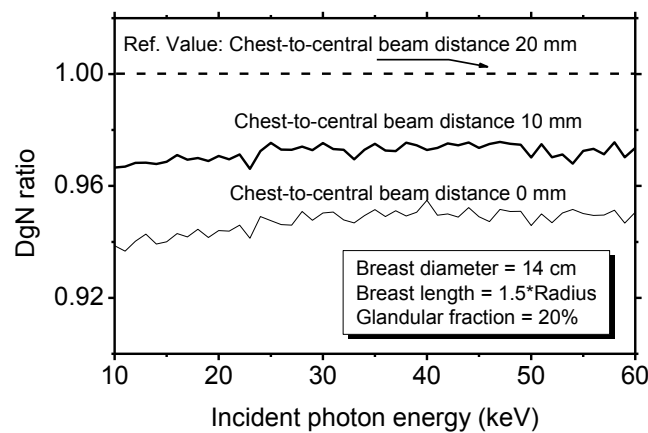
Fig. 3.3. *Ratio between monoenergetic DgN_{CT} coefficients for distance between the chest and the central X-ray beam is 20 mm and those evaluated with such a distance set to 10 mm and 0 mm.*
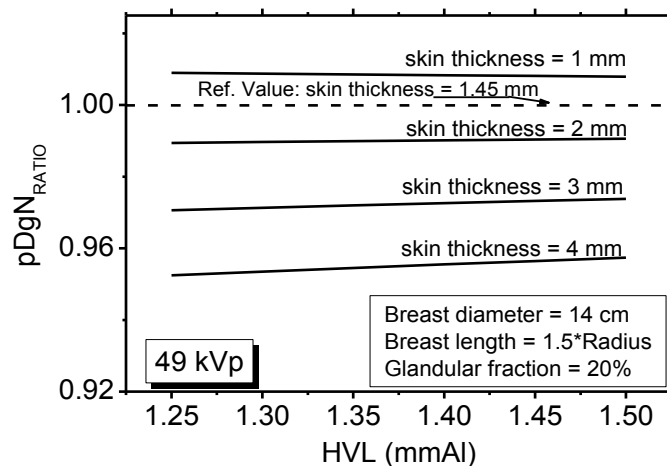
Fig. 3.4. *Ratio between polyenergetic DgN_{CT} coefficients at 49 kVp and HVL between 1.25 and 1.50 mmAl evaluated with a skin thickness of 1.45 mm and those for skin thickness of 1, 2, 3 and 4 mm. The HVL was tuned by varying the Al filter thickness.*

3.1.3. Monoenergetic curve fit

Figure 3.5 shows the DgN_{CT} coefficients for a 25% glandular breast with a diameter of 120 mm. They were evaluated for a breast height of 1, 1.5 or 2 times the breast radius. As already shown in

41

Thacker and Glick (2004), the DgN_{CT} coefficients reduce as the breast length reduces. The DgN_{CT} coefficients were evaluated for primary photon energy ranging between 5 and 82 keV with a 1 keV step. The continuous lines represent the DgN_{CT} coefficient curve fitting (8th-order polynomial); in all cases in the fig. 3.5, the R^2 statistics is higher than 0.9999 and the zero-order term was forced to 0. Although the DgN_{CT} coefficients have been evaluated in the photon energy range 5−82 keV, the fitting curves presented in this work can lead to uncorrected results outside the range 8−80 keV, because of the boundary conditions. In Appendices C.1−C.3 (sect. 9.3) report the 8th polynomial coefficients for all the DgN_{CT} evaluated for breast glandular fraction of 0%, 14.3%, 25%, 50%, 75% and 100% and for breast diameters in the range 80-180 mm with a step of 10 mm. They have been evaluated for breast height of 1, 1.5 or 2 times the breast radius. In all cases, the R^2 is higher than 0.9998.
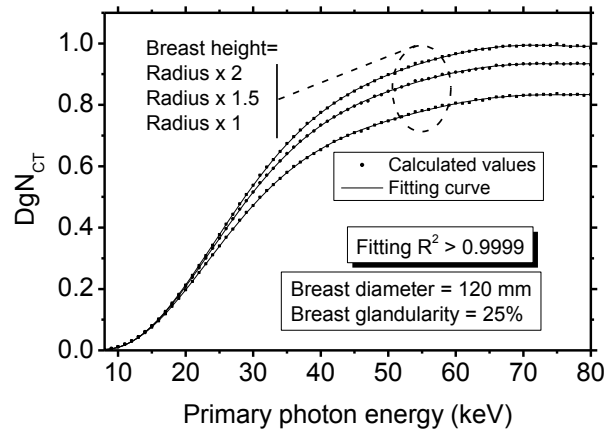
Fig. 3.5. *Monoenergetic DgN$_{CT}$ for 25% glandular breast with a diameter of 120 mm. Breast height equal to 1, 1.5 or 2 time the breast radius.*

3.1.6. Polyenergetic DgN$_{CT}$

Figure 3.6 shows the $pDgN_{CT}$ evaluated for a 14.3% glandular breast, with a diameter ranging between 8 cm and 18 cm and with the breast height equal to 1.5 times the radius, as a function of the beam HVL. They were computed from the corresponding monoenergetic DgN_{CT} by means of eq. 2.7. For a breast with a diameter of 12 cm, increasing the beam HVL from 1.25 to 1.40 mm Al increases the $pDgN_{CT}$ coefficients by 7%. Appendices C4−C6 (sect. 9.3) report $pDgN_{CT}$ coefficients for breasts with a glandular fraction of 0%, 14.3%, 25%, 50%, 75% and 100% with diameter ranging between 8 cm and 18 cm. The breast height is 1 (appendix C.4), 1.5 (appendix C.5) or 2 (appendix C.6) times the breast radius. The spectra HVL (W anode and Al added filtration) was comprised in the range 1.25−1.50 mm Al (sampling step = 0.05 mm Al).

Figure 3.7 shows the ratio between the monoenergetic DgN_{CT} evaluated with heterogeneous breast phantoms (on average) and those evaluated with a homogeneous breast model. As showed in previous sections (Sarno *et al* 2016c), a slight discrepancy, lower than ~2%, in MGD values can be

ascribed to the G-factor, which is not employed for the heterogeneous breast. Figure 3.7 shows that no further bias are introduced by the source rotation.
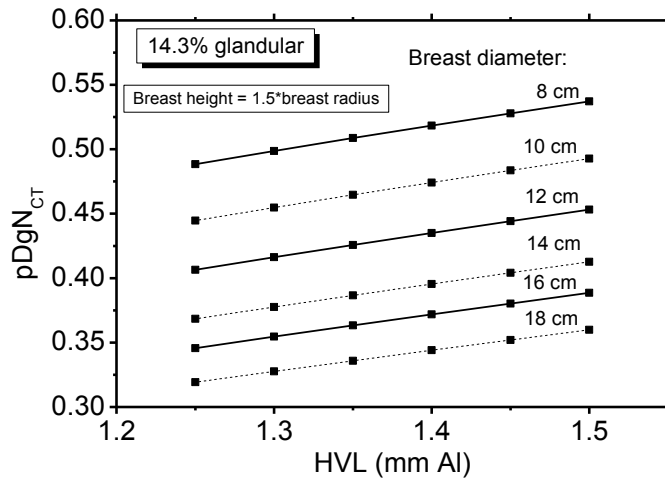
Fig. 3.6. *Polyenergetic DgN$_{CT}$ for a 14.3% glandular breast.*
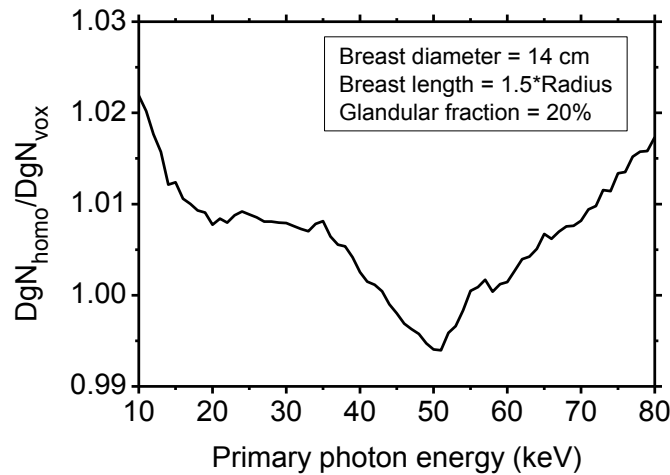
Fig. 3.7. *Ratio between the DgN$_{CT}$ coefficients evaluated with a heterogeneous breast model and a homogeneous breast model.*

Each of the patient specific breast phantom has been uploaded in the MC code and irradiated with a W spectrum at 49 kVp (HVL = 1.40 mm Al). Then the pDgN$_{CT}$ coefficients were evaluated by dividing these values for the air kerma at the isocenter evaluated without the breasts in place. For each patient breast, the pDgN$_{CT}$ evaluated with the homogeneous model were computed by interpolating or extrapolating the values in appendices C4−C6 on the basis of the breast glandularity, diameter and length. Figure 3.8 shows the ratio between these last values and those evaluated with the patient specific breasts. It shows that such a ratio, on average, is 1.045. This indicates that the difference in MGD estimation with the data provided in this work, obtained with a homogenous breast model, is not more than 4.5%, on average. The ratio minimum and maximum values are 0.822 and 1.243, indicating that in future, a more patient specific breast model can be adopted.
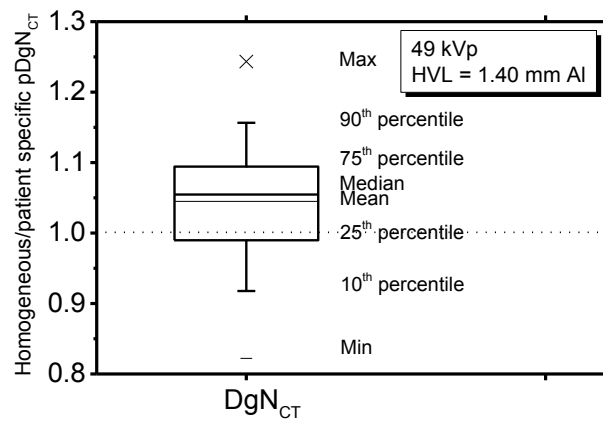
Fig. 3.8. *Ratio between the pDgN*CT *evaluated for homogeneous breast model and those obtained for the patient specific breast phantom. 49 kVp, HVL = 1.40 mm Al.*

3.2. Breast CT with synchrotron radiation

In SR-BCT, proposed in SYRMA-CT project, the thin laminar X-ray beam is fixed and the patient support rotates around a vertical axis and translates vertically. In order to limit the total scan time in multiple turns of the patient support, one may envisage that only a fraction of the pendant breast is imaged, e.g. by investigating regions where a suspicious lesion has been previously located. This condition calls for the specific evaluation of the glandular dose and normalized glandular dose coefficients in cases where not all of the (glandular mass in the) breast is irradiated, as also occurs in spot compression mammography (sect. 2.2). This evaluation must be performed (for a given breast size, breast composition and monochromatic beam energy) by considering various heights of the total scanned section (in the longitudinal direction from chest wall to nipple), in dependence of the total height of the thick section of the breast selected for imaging. A specific dosimetric protocol of this type is needed for assessing the imaging scan procedure.

In the present MC study, we calculated the breast glandular dose for a SR-BCT scan for various sizes and compositions of the pendant breast, at various energies of the monochromatic SR beam and at a fixed height of the laminar SR beam for different thicknesses of the total irradiated section of the breast. This permitted to calculate also normalized glandular dose coefficients for given breast size and composition, at the monochromatic beam energy, to be used for *in vivo* SR-BCT scans. We point out that the MC code discussed in this section (3.2), differently from that of the previous sections, was developed by Dr. C. Fedon in his PhD thesis (Fedon 2016), based on the work of the SYRMA-CT collaboration. Results from this code were reported in Mettivier *et al* (2015): in this paper new dose metrics have been introduced (see following sect.), which will be implemented for partial breast irradiation dosimetry in this thesis work (sect. 4.1). This part of the thesis aims at introducing the issue of the partial irradiation in pendant uncompressed breast geometry in order to better understand the results related to the SYRMA-CT scanner in sect. 4.1.

3.2.1. Dosimetric parameters

Similarly to the case of spot mammography, MGD was calculated from the ratio between E_T and M_T (eq. 2.9), and the MGD_V from the ratio between E_V and M_V (eq. 2.10). However, one has to consider also the dose delivered indirectly to the glandular tissue outside the irradiated volume: this dose originates from radiation scattered to breast regions adjacent to the irradiated ones. Then, one can define a third quantity, MGD_t:

$$MGD_t = \frac{E_T}{M_V} \tag{3.4}$$

where E_T is greater than E_V due to scatter dose, and M_V less than M_T, and so MGD_t is greater than MGD_V. The two quantities are coincident only in the limit where the whole breast is scanned. In the axial scanning of a section of the breast in multiple successive rotations and corresponding vertical translations of the patient support, for a given width of the SR beam, MGD_V and MGD_t should be

45

evaluated as a function of the total height of the scanned section, since the tails of the longitudinal scatter dose profiles from each axial scan overlap and sum up to determine the multiple scan average dose to the glandular tissue. If the height of the irradiated section corresponds to that of the beam (i.e. just one axial scan is performed), then the MGD_t metric is related to the notion of the CTDI metric in whole body CT dosimetry (Kalender 2014). Indeed, in whole body CT, the $CTDI_{100}$ is evaluated in single axial scan with an ion chamber which integrates the dose along the z-axis over a length of 100 mm. Similarly, in the evaluation of the MGD_t parameter, the energy deposited by scattered radiation outside the irradiated volume is attributed to the glandular mass in this volume, as an additional contribution to the dose.

As already done for DgN_{CT} coefficients in cone-beam BCT, DgN_{CT}, DgN_{CT}^t and DgN_{CT}^V were computed by dividing MGD, MGD_t and MGD_V by the air kerma at the scanner isocenter in the case of partial irradiation.

3.2.2. Monte Carlo simulations and irradiation geometry

The MC simulations for this study were carried out using the Geant4 toolkit 10.00. The SYRMA-CT collaboration decided to use G4EmLivermorePhysics library, instead of Option 4 used in the previous section. Although the two libraries showed to produce similar results in breast dosimetry (Fedon *et al* 2015), additional validation tests were performed. The code was validated vs measurement at the SR source and data in literature. The validation results are reported in Mettivier *et al* (2015).

By using the validated MC code, the dose was evaluated in cases which matched the characteristics of the SR beam specifications. A sketch of the simulated setup is reported in fig. 3.9. The radiation field shape was a rectangular one, with a fixed width of 150 mm and a variable dimension *w* according to the case studied. The samples had a cylindrical shape (diameter = d) with a height *h* of 1.5 times the sample's radius, as in (Boone *et al* 2004). A water box (with a volume of 13.5 dm^3) was added for simulating the body of the patient. The skin thickness and the glandular fraction by weight used in this study were 1.45 mm (Huang *et al* 2008, Shi *et al* 2013) and 0%, 50% and 100%, respectively. The dimensions of the irradiated volume were calculated as $\pi(d/2)^2 \times s$ where *s* is variable according to the case studied.

A CT scan simulation consisted of a rotation of the phantom from 0 to 360 deg with a 1 deg step; for each projection image up to 1 million photon histories were generated. The simulations were repeated 9 times using different seeds for each simulation for a *COV* less than 1%.

The height *w* of the beam was fixed to 3 mm and MGD, MGD_V and MGD_t were calculated. In this case, the vertical dimension, *s*, of the irradiated breast volume was varied from 3 to 87 mm by translating vertically the beam with a step of 3 mm. This is the case closest to the SR-BCT scan conditions in the SYRMA-CT project.

Finally, the DgN$_{CT}$, the DgN$_{CT}$^{v} and the DgN$_{CT}$^{t} coefficients for breast diameter in the range 80−160 mm with a glandular fraction by mass of 0%, 14.3%, 25%, 50%, 75% and 100% with photon energy in the range 8−50 keV (1 keV step) were calculated.
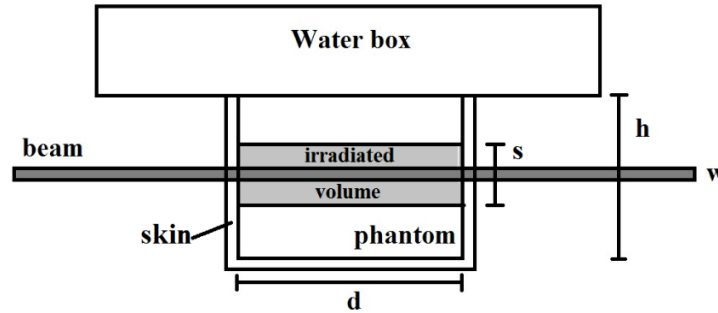
Fig. 3.9. *Sketch of the simulated setup. The radiation field shape was set with a fixed width of 150 mm and a variable dimension w according to the case study. The samples had a cylindrical shape with a diameter d and a height h. The dimensions of the irradiated volume are $\pi(d/2)^2 \times s$ where s is variable according to the case studied. A water box (with a volume of 13.5 dm^3) was added for simulating the body of the patient. The skin thickness was 1.45 mm.*

3.2.3. Dose evaluation

Figure 3.10a shows the MGD, the MGD$_V$ and the MGD$_t$ for a 12-cm breast diameter (h = 90 mm) with a glandular fraction of 50% at a fixed energy of 38 keV (one of the energy values that will be adopted in the SYRMA-CT project) as a function of the height s of the irradiated volume. It is possible to note the linear dependence of the MGD on the height of the irradiated volume, due to the linear increase of the deposited energy with the increasing vertical dimension of the irradiated volume. On the other hand, the MGD$_V$ increases with a sub-linear trend with the increasing vertical dimension of the irradiated volume, because the deposited energy increases together with the glandular mass of the irradiated volume. It is worth to note that the curves in fig. 3.10a reflect dose evaluated in sect. 2.2 for the partial breast irradiation in spot mammography (fig. 2.26).

For the MGD$_t$, the energy is deposited throughout the whole breast but the glandular mass used in the calculation of the corresponding dose is that of the irradiated volume. The MGD$_t$ is almost constant with a little decrease with the vertical dimension of the irradiated slice since as the irradiated area approximates the size of the entire breast, the energy delivered outside the slice is gradually smaller. The dependence of MGD$_V$ as a function of the height s of the irradiated volume on the photon energy is shown in fig. 3.10b, which illustrates the non-monotonic trend of MGD$_v$ vs energy at any fixed height s.
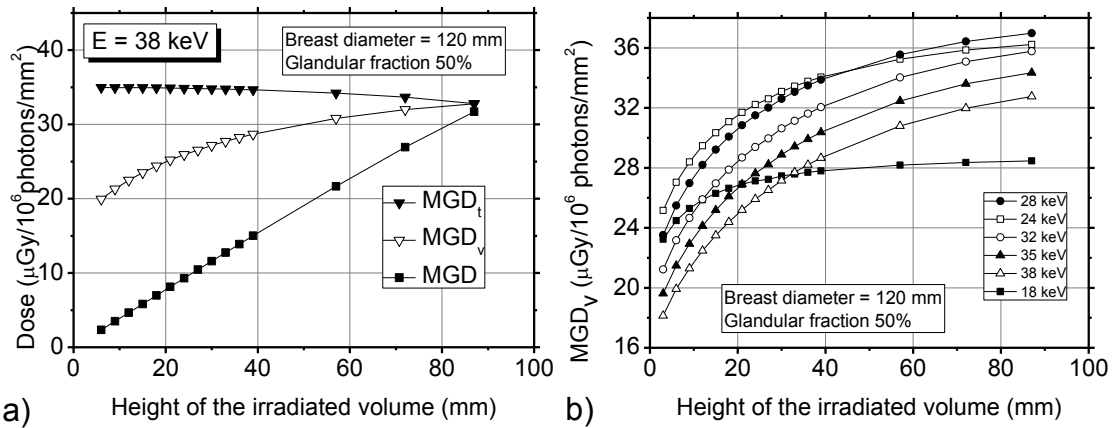
Fig. 3.10. *a) The MGD to the glandular mass present in the whole breast (solid square), or in the irradiated volume (open down triangle) or in the irradiated volume adding the contribution from scatter dose (close down triangle) for a 12-cm diameter breast phantom with a glandular fraction of 50% varying the dimension of the irradiated volume with a 3 mm-height beam. The photon energy of the monoenergetic beam was 38 keV. b) MGDv as a function of the height of the irradiated volume at different values of the photon energy.*

3.2.4. DgN$_{CT}$ evaluation

In the SYRMA-CT project, the authors plan to irradiate a breast section of height 30 mm by translating vertically ten times the patient bed in 3-mm steps. For this reason, the DgN$_{CT}$ coefficients in the case s = 30 mm with a w = 3 mm height beam were calculated and reported in fig. 3.11, 3.12 and 3.13. Figures 3.11a-c show the DgN$_{CT}$ coefficients, which will be used to calculate the MGD to the whole breast for a breast diameter from 8 to 16 cm at 0%, 50% and 100% glandular fraction, respectively. Figures 3.12a-c and figures 3.13a-c show the DgN$_{CT}$^{v} and DgN$_{CT}$^{t} coefficients, needed for calculating the MGD$_v$ and MGD$_t$ for a slice of 30-mm height (breast diameter varied from 8 to 16 cm, glandular fraction of 0%, 50% and 100%, respectively).
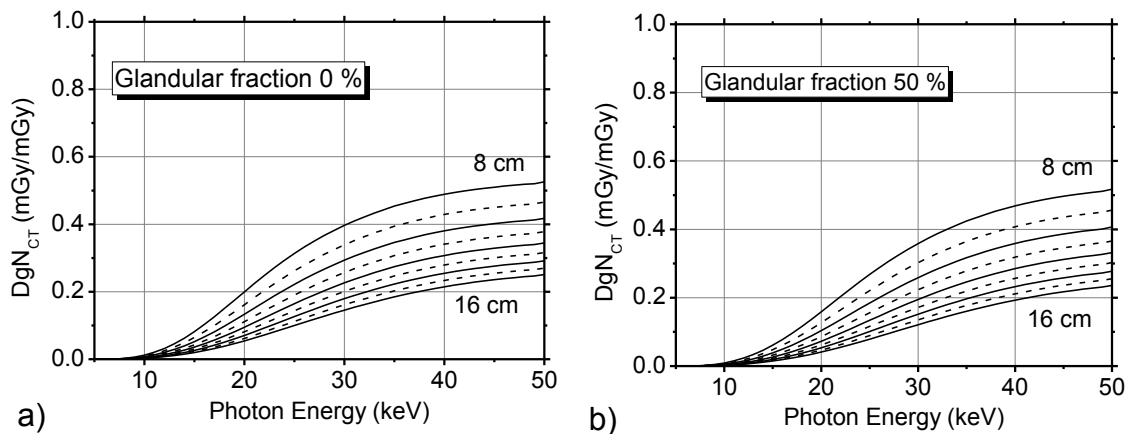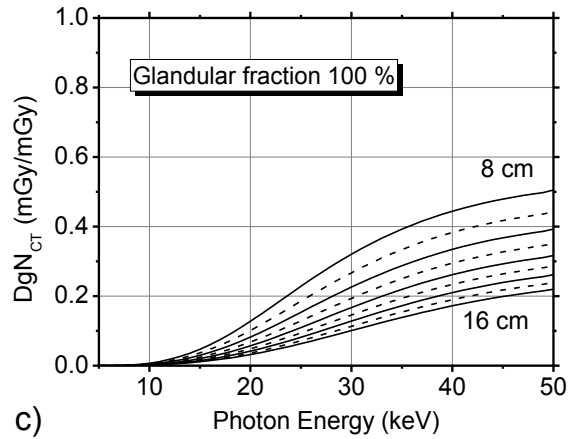
Fig. 3.11. *DgN$_{CT}$ coefficients to calculate the MGD (a, b, c) in the case of a 3 mm-height beam irradiating a 30 mm-height slice for a breast diameter from 8 to 16 cm in 1-cm step, and a glandular fraction of 0% (a), 50% (b) and 100% (c). The energy was varied from 8 to 50 keV with 1 keV step; data were represented as lines for ease of visualization.*
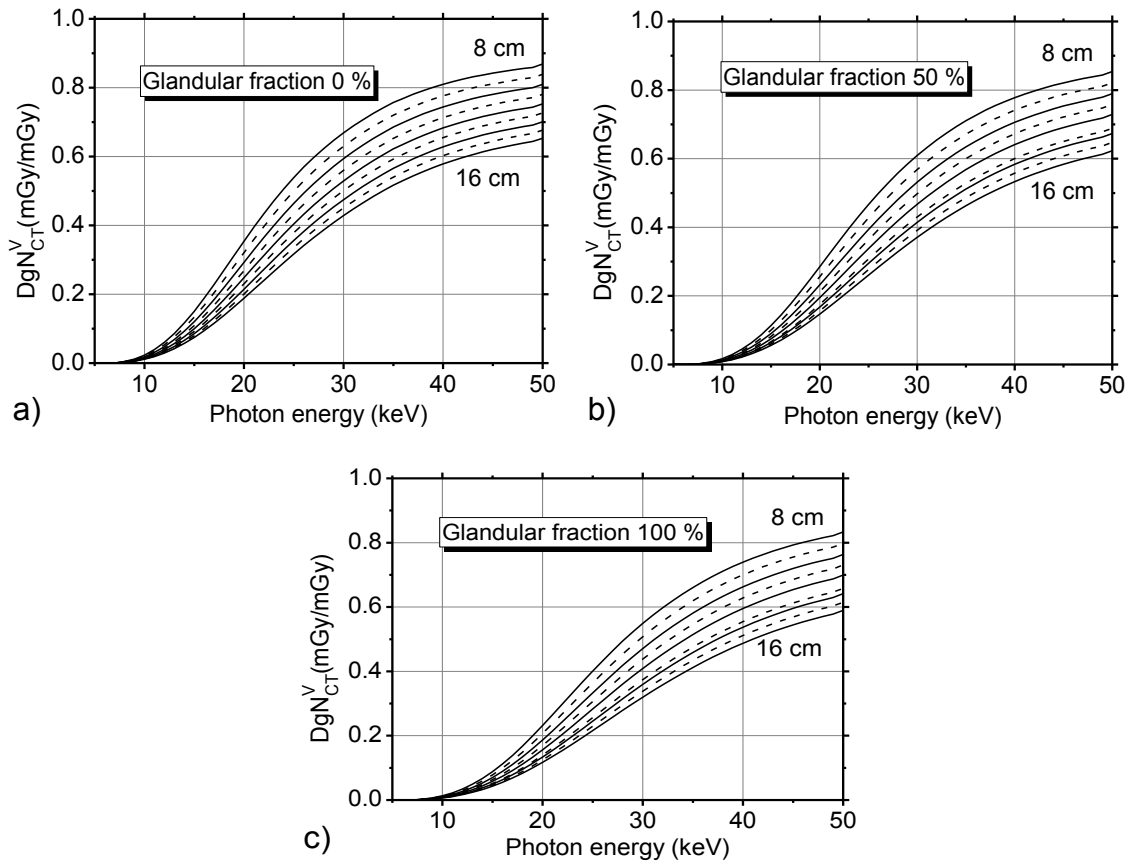
Fig. 3.12. *DgN$_{CT}$ coefficients useful to calculate the MGD$_v$ (a, b, c) in the case of a 3 mm-height beam irradiating a 30 mm-height slice for a breast diameter from 8 to 16 cm in 1-cm step, and a glandular fraction of 0% (a), 50% (b) and 100% (c). The energy was varied from 8 to 50 keV with 1 keV step; data were represented as lines for ease of visualization.*
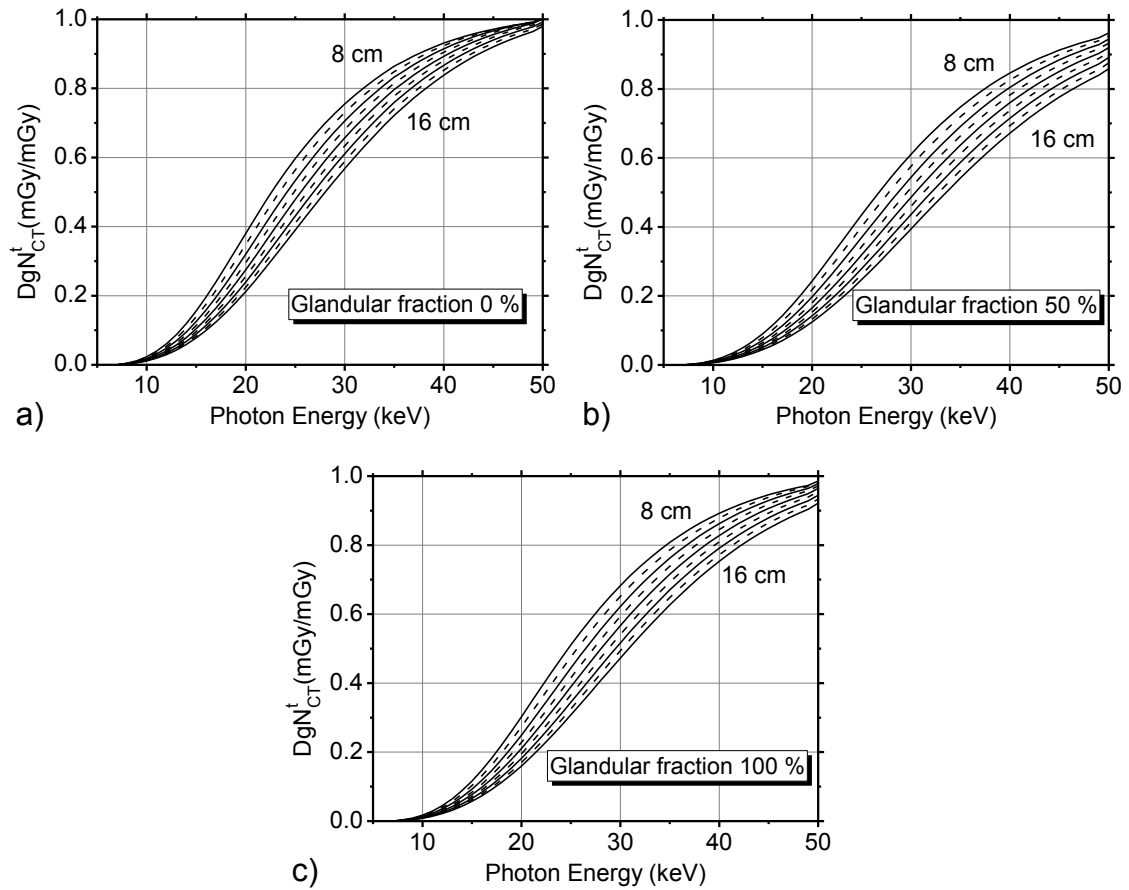
Fig. 3.13. *DgN$_{CT}$ coefficients to calculate the MGD$_t$ (a, b, c) in the case of a 3 mm-height beam irradiating a 30 mm-height slice for breast diameter from 8 to 16 cm in 1-cm step, and a glandular fraction of 0% (a), 50% (b) and 100% (c). The energy was varied from 8 to 50 keV with 1 keV step; data were represented as lines for ease of visualization.*

4. Propagation-based phase contrast breast imaging

This chapter presents investigations in which I was involved during this PhD thesis, whose results are reported in the following publications:

- *Sarno et al 2016 Imaging performance of phase-contrast breast computed tomography with synchrotron radiation and a CdTe photon-counting detector. Phys. Medica 32 681–690*
- *Longo R et al 2016 Towards breast tomography with synchrotron radiation at Elettra: first images. Phys. Med. Biol. 61 1634–1649*
- *Sarno A et al 2017 A framework for iterative reconstruction in phase-contrast computed tomography dedicated to the breast. Trans. Rad. Pl. Med. Sc. under review*
- *Sarno et al 2016 Cone-beam micro computed tomography dedicated to the breast Med. Eng. Phys. 38 1449–1457*

4.1. 3D phase contrast with synchrotron radiation (SYRMA-CT)

In the field of the PB-PhC breast imaging, BCT using synchrotron radiation (SR-BCT) may play a relevant role, both as a reference imaging technique and in order to exploit opportunities offered by a tunable, monochromatic and parallel X-ray source with extremely high spatial (lateral) coherence and high photon flux. Research groups at the SR facility ELETTRA (Trieste, Italy) (Castelli *et al* 2011; Quai *et al* 2013; Longo *et al* 2014, 2016; Pani *et al* 2004; Pacilè *et al* 2015), at the European Synchrotron Radiation Facility in Grenoble, France (Fiedler *et al* 2004; Bravin *et al* 2013; Keyriläinen *et al* 2005, 2008) and at the Imaging and Medical beamline of the Australian Synchrotron (Nesterets *et al* 2015) investigated these phase-contrast based breast imaging techniques. In particular, recent results (Pacilè *et al* 2015; Nesterets *et al* 2015; Longo *et al* 2016) showed that the PB-PhC technique offers significant improvement in image quality compared to conventional absorption-based BCT. This is a significant indication, since in the field of phase-contrast imaging free-space propagation techniques offer advantages of simplicity, reliability and feasibility of clinical implementation, compared to techniques requiring complex optical setups *(*Fiedler *et al 2004;* Keyriläinen *et al* 2005, 2008; Momose *et al* 1996; Sztrókay *et al* 2013; Takeda *et al* 1998, 2000; Zhao *et al* 2012; David *et al* 2007; Cai and Ning 2009*)*.

In this line of research, the SYRMA-CT collaboration, based at the ELETTRA SR facility, investigates the technique of phase-contrast in vivo SR tomography dedicated to the diagnosis of breast cancer, exploiting the propagation based phase-contrast technique, with a laminar and monochromatic SR X-ray source, and a large-area single-photon counting detector *(*Longo *et al* 2016*)*.

4.1.1. Experimental Setup at Elettra

The SYRMA-CT project is ongoing at the SYRMEP beamline at ELETTRA (Longo *et al* 2016), a line dedicated to medical physics applications. For the execution of CT acquisitions, the setup was modified compared to the previous one used for phase-contrast mammography (Longo *et al* 2014), in order to perform the rotation (in several turns) of the patient support, with the subject in the prone position and the breast hanging at the rotation center (fig. 4.1). The radiation source is a bending

magnet of the ELETTRA storage ring; the beam energy is selected by means of a Si(111) double crystal monochromator, which permitted the tuning of the beam energy in the range 8.5–40 keV, with an energy resolution of 0.2%. The beam shape in the radiology hutch is defined by a tungsten slits system, as a rectangle of 200 mm (horizontal width) and a height of 3 mm (vertical height). The X-ray beam transverse coherence length is of the order of 5 μm. The CT views are acquired in a simplified setup using a rotation stage in the breast position of the radiology hutch, at a distance of 2 m from the imaging detector. Mittone *et al* (2014), in a simulation study performed with monochromatic X-ray radiation, showed that the ratio between the dose to the breast and transmittance through the imaged object decreases as the photon energy increases up to about 60 keV. Based on this result, the beam photon energy chosen for the SYRMA-CT project is 38 keV, the highest photon energy possible at ELETTRA without affecting drastically the X-ray beam stability. The projections are collected over 180 deg, thanks to the negligible horizontal divergence of the beam (7 mrad) which approximates a parallel beam geometry.
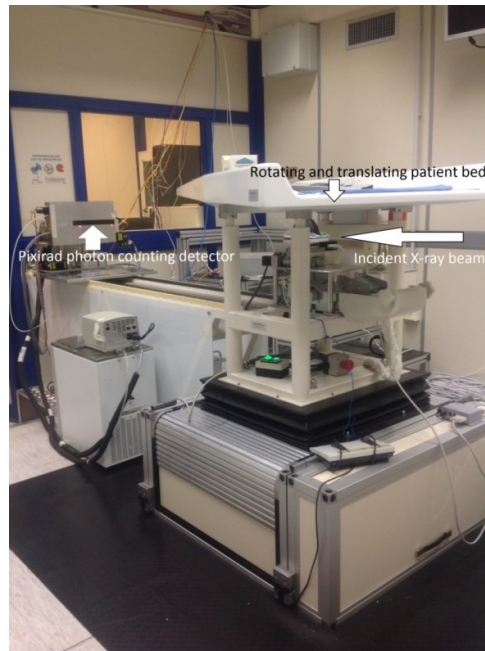
Fig. 4.1. *Photo of the SYRMA-CT setup for phase-contrast breast CT at the ELETTRA synchrotron radiation laboratory (Trieste, Italy). The horizontal beam irradiates the breast hanging from a hole in the patient bed; the transmitted beam is recorded by a high resolution photon counting detector. Rotation and translation of the bed permits to acquire in successive axial scans over 180 deg a complete dataset for CT reconstruction.*

The employed detector is PIXIRAD-8, a high efficiency, direct detection, photon counting X-ray imaging detector. PIXIRAD-8 is a multi-block, 2 Mpixel detector consisting of eight PIXIRAD detector units aligned in a row, produced by PIXIRAD Imaging Counters srl (*http://www.pixirad.com*), an INFN Pisa spin-off company. The basic block is a hybrid architecture in which the sensor and readout electronics (ASIC) are coupled with the flip-chip bump-bonding technique. For a single unit, the sensor (ACRORAD Co., Ltd.) is a cadmium telluride (CdTe) Schottky type array of diodes with a total area of 30.96 mm × 24.98 mm and a substrate thickness of

0.650 mm. The pixel arrangement is on a hexagonal honeycomb matrix with a pitch of 60 μm. Energy resolution, linearity, efficiency, noise characteristics and line spread function of the single module, as a function of energy and thresholds have been investigated (Vincenzi *et al* 2015; Delogu *et al* 2016). As outlined in Kuttig *et al* (2015), a high Detective Quantum Efficiency of a thick, direct conversion photon-counting detector (1-mm thick CdTe sensor in their study) may allow for a dose reduction with respect to energy-integrating scintillator-based detectors used in current BCT setups with polychromatic sources and cone-beam geometry. The multi-block module used in this project is an 8-unit system reaching a total active area of 250 mm × 25 mm; raw images have a size of 4608 × 476 pixels. Due to the modular structure of the device, a dead space is present between adjacent blocks, with a width of 180 μm. The detector is able to count the X-ray photons converted in each pixel of the CdTe sensor, in two counters. Each counter can be written while the other is read. By using this feature it is possible to realize the so-called Dead Time Free (DTF) modality where no events are lost over the time even with a continuous flux of photons. In DTF modality the maximum frame rate of Pixirad-8 is 30 fps. However, following, the CT scans were performed in step-and-shoot modality, with an exposure time of 50 ms per view, which implies that in this work, the system spatial resolution and noise are not affected by the blurring introduced by the continuous rotation of the object.

A low-level discriminator threshold equivalent to 19 keV (corresponding to half the energy of the incident photons) was set on the pixel signal; this permitted minimizing charge-sharing effects in the pixel signal (double counts, loss of spatial resolution) thus avoiding a loss of counts (Lopez *et al* 2014). This high-value threshold makes the dark noise of the detector negligible (Bellazzini *et al* 2013). The images were flat-field corrected to apply gain correction. Subsequently, a re-sampling of the images based on linear interpolation was performed, in order to change from a honeycomb to a square pixel array, producing images with 30-μm equivalent pixel pitch. In this acquisition setup, the average counts per pixel on the detector for a single projection was about 150: in this region the detector is completely linear (Delogu *et al* 2016).

The phase signal was retrieved by processing the projections with the algorithm proposed by Paganin *et al* (2002). This algorithm can provide a quantitative retrieval of the phase information in case of pure-phase objects, i.e. without beam attenuation. This is not the case of our experiment, in which the attenuation is relevant. However, there is a growing body of evidence showing that the Paganin algorithm can be profitably applied also in case of objects that produces both phase shift and attenuation. Although in this case the Paganin filter does not provide a quantitative reconstruction of the phase information, it yields a significant improvement in contrast-to-noise ratio on soft tissues, with a relatively small loss of resolution compared to other more conventional low-pass filters (Longo *et al* 2016).

The reconstructed slices were obtained from the pre-processed projections using Filtered Back Projection (FBP). In order to reconstruct slices with voxel size of $(60\ \mu m)^3$ and $(120\ \mu m)^3$, projections underwent a 2x2 binning and a 4x4 binning process, respectively.

4.1.2. System MTF and NPS assessment

The high-resolution detector of the SYRMA-CT system, and the practical absence of penumbra due to the almost parallel beam geometry (7 mrad beam divergence), contribute to produce high-resolution CT scans over a 180-deg angular span. The spatial resolution of the SYRMA-CT scanner was evaluated by measuring the system MTF; a limiting spatial frequency was evaluated at 10% MTF value ($MTF_{0.1}$). A sharp polymethylmethacrylate (PMMA) edge (for which $\delta(E) = 1.845 \times 10^{-7}$ and $\beta(E) = 1.219 \times 10^{-11}$ @ $E = 38$ keV - Xop 2.3; thickness = 2 mm; height = 90 mm) was imaged in order to evaluate the system edge spread function (ESF), from which the line spread function (LSF) of the system was evaluated, by numerical differentiation. In order to reduce the noise, in the case of the MTF evaluation over the PMMA edge, the ESF curves have been averaged over 10 consecutive rows. The PMMA slab introduced little attenuation but sizeable phase shifts in the X-ray beam. Then, the system MTF (normalized to the value at zero spatial frequency) was computed via numerical Fourier transform. It is worth noting that the fringes on the phase-contrast image of the PMMA edge (determining the edge enhancement effect typically observed in in-line phase-contrast imaging) may distort the MTF curves derived in the above way, introducing an artefact (i.e. normalized MTF values greater than 1) similar to the one occurring in CT reconstruction with the use of some kernels, characterized by undershoots in the kernel curve (see, e.g. Boone 2001b).

The system MTF was evaluated also by using a highly attenuating object, a 50-μm diameter tungsten wire placed parallel to the rotation axis, at 50 mm radial distance from the axis, slightly tilted (2 deg) with respect to the rotation axis in order to obtain the presampled LSF. This technique is commonly used for spatial resolution assessment in cone-beam breast CT (Kwan *et al* 2007; Mettivier and Russo 2011a). The evaluation of the system MTF was carried out with two reconstruction voxel sizes ($60 \times 60 \times 60\ \mu m^3$ and $120 \times 120 \times 120\ \mu m^3$, respectively).

The common metric for the evaluation of noise properties in attenuation based CT imaging is the (3D) NPS, which describes the spatial decomposition of noise variance in an image as a function of the spatial frequency, thus expressing the noise transfer property of the system. Assuming the applicability of linear analysis system theory for phase-contrast imaging, for the experimental determination of the NPS a scan was performed of a homogeneous mammographic phantom ($\delta(E) = 1.619 \times 10^{-7}$; $\beta(E) = 0.697 \times 10^{-11}$; @ $E = 38$ keV (CSIRO)), a CIRS phantom BR 50/50 mod. 014AD simulating a 50/50 breast tissue (i.e. a 50% glandular, 50% adipose tissue) (further details are reported in sect. 4.1.4). The 1D coronal NPS was evaluated as indicated in Yang *et al* (2008). The 2D NPS was estimated by the 2D fast Fourier transform from a region of interest (ROI), which did not include any targets, in the coronal view. Then, the 1D noise power spectrum was computed by

radially averaging the 2D NPS. Pixel values in phase-contrast CT slices represent the attenuation coefficient (proportional to the local value of β) of the imaged object, and the pixel value of images after phase retrieval is proportional to δ. Then, normalized NPS (NNPS) curves were evaluated, by dividing the NPS curves for the square root of the mean signal value in the ROI where the NPS was evaluated. These curves do not depend on the signal units of measurements, so permitting to compare noise power spectrum in the images obtained with and without phase retrieval.

4.1.4. Contrast and microcalcification visibility

In order to test the microcalcification visibility and CNR in tomographic images, the multilayer commercial test object (CIRS mod. 014AD) was imaged. Figure 4.2 shows a radiograph of this object (total thickness = 85 mm), obtained via a mammography unit (Siemens Mammomat Inspiration) at 32 kVp (W/Rh), with focal spot of 0.3 mm, pixel size of 85 μm and entrance air kerma of 15.35 mGy. The test object comprises several layers simulating the attenuation coefficient of a breast tissue with an average glandular fraction of 50%; one layer contains different targets for image quality analysis. Its target layer includes clusters of alumina and $CaCO_3$ grains simulating microcalcifications (with diameters from 130 to 390 μm), four high-contrast fibers with a diameter of 25 μm, six masses (hemispheres with diameter in the range 1.8–6.32 mm, simulating 75% glandular tissue attenuation) and a 5-mm thick contrast single step-wedge (adipose/glandular tissue). Just one rectangular slab (20-mm thick with a size of 100×125 mm^2) of the multilayer phantom was scanned with the SR setup.
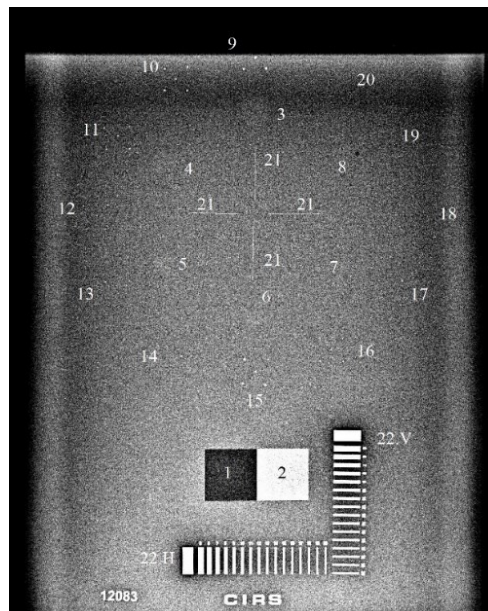
Fig. 4.2. Radiography along cranio-caudal direction of the CIRS test object BR50/50 mod. 014AD (50% glandular breast tissue attenuation), shown for the purpose of object description. It includes a contrast step-wedge target (labels 1 and 2, superimposed on the image, for adipose and glandular tissue, respectively), six 75% glandular hemispheric masses (labels 3-8) with a radius in the range 3.16-0.90 mm, clusters of alumina (labels 15-20) and CaCO₃ (labels 9-14) (from 390 to 130 μm) microcalcifications, high-contrast fibers with a diameter of 25 μm (label 21) and bar patterns (labels 22.H and 22.V). Setup: Siemens Mammomat Inspiration, 32 kVp (W/Rh), focal spot size 0.3 mm, detector pixel size 85 μm, entrance air kerma 15.35 mGy.

The image CNR was evaluted as:

$$CNR = \sqrt{A}\frac{|S_a - S_b|}{\sqrt{\frac{\sigma_a^2 + \sigma_b^2}{2}}} \qquad (4.1)$$

where S_a and S_b are the average pixel values in the selected ROIs, respectively, σ_a^2 and σ_b^2 are the corresponding variances and A is the area of the ROI (in pixels).

Two ROIs, each of 100×100 pixels, were selected in the step-wedge inclusion of the test object (one for fat and one for glandular materials, respectively): in this specific case, S_a and σ_a^2 are the signal and the variance in the glandular inclusion and S_b and σ_b^2 for the signal and the variance in the fat inclusion, respectively.

A global figure of merit (Q) was evaluated in order to compare the imaging performance of the SR system in the images obtained with and without phase retrieval. This index was proposed in Kalender WA (2005) to obtain a single figure of merit in CT images taking into account the system spatial resolution, the image noise (σ^2) and the radiation dose to the tissue (D):

$$Q = c\frac{MTF_{0.1}^4}{\sigma^2 \cdot D} \qquad (4.2)$$

where c is a constant. Q takes high values when the spatial resolution is high, the signal noise is low and the dose is low. Since the compared images were obtained with the same amount of radiation dose, the quantity c/D was fixed to 1 mm^4. The noise was evaluated as the variance in the ROI selected for the NPS evaluation, normalized to the square root of the mean signal value in the same region. It is worth noting that Q does not take into account the edge enhancement and could penalize the quality assessment in the case in which such an effect becomes noticeable.

Moreover, in order to evaluate the quality of the images produced by SYRMA-CT setup, a handmade phantom was developed. It is a polycarbonate (PC) cylindrical test object (diameter = 8 cm). This object embodies 8 inserts with a diameter of 1 cm, each one made of a different material: H_2O, $CaCl_2$, ethanol, glycerol, paraffin, breast glandular tissue, breast adipose tissue or breast cancer tissue from an autoptic specimen. The system spatial resolution in the images of such a phantom was evaluated by determining the full width at half maximum (FWHM) of the system LSF, calculated as the derivative of the ESF, obtained from the line profile across the edge PC-air. The CNR was evaluated between the PC background and the other inserts.

4.1.5. *The iterative reconstruction and ring removal algorithm*

Among the huge variety of choices, the simultaneous algebraic reconstruction technique (SART) iterative algorithm has been successfully applied to a wide range of CT applications (Camerani *et al* 2004, Golosio *et al* 2004, Cauzid *et al* 2007). It is relatively fast compared to other iterative algorithms, and its convergence properties have been well studied (Kak and Slaney 1988). Therefore, this algorithm was used for reconstructions in this preliminary study. In the SART algorithm, the

iterative corrections are made angle-by-angle, i.e. for each angular view, the corrections are evaluated and applied simultaneously to all rays of the projection. One iteration is considered to be completed when all the projections have been used. We used a random ordering for the projections in order to avoid systematic errors in the reconstruction. A few iterations are sufficient for the algorithm to converge. The reconstructions presented in this work are made using five iterations. The correction was multiplied by a relaxation factor, which grows linearly from zero to a maximum in the first few projections used by the reconstruction algorithm (the first 10 in this work) and decreases linearly from this maximum to zero with the number of projections. The relaxation factor suppresses residual oscillations, ensuring stability and convergence of the iteration (Golosio *et al* 2004). A bilateral filter was combined with the iterative reconstruction in order to improve image regularization. This type of filter takes two parameters: a spatial filter parameter, α, which controls the amount of smoothing differences in coordinates, and a range filter parameter ϕ, which accounts for smoothing differences in intensities. In this work α is expressed in pixel^{-1}, while ϕ is expressed in cm^{-1}. The latter are the same units used for the absorption coefficient distribution reconstructed by the tomographic reconstruction algorithms.

The single photon-counting detector presented in sect. 4.1.1. demonstrated excellent performance in terms of signal-to-noise ratio. However, to remove the remaining visible ring artefacts produced by slight local imperfections in the flat field correction at the gaps between different detector ASICs, an improved ring correction algorithm has been developed and coupled with the iterative reconstruction. This algorithm is based on a rank filter, which is a generalization of a median filter. For each pixel, this filter takes a window of nearest neighbors, sorts their values, excludes the largest and the smallest values, and evaluates the average of the remaining ones. Then, a Gaussian filter is applied to the not-excluded pixels, both to each 2D projections and to the projection's angular sequence, treated as a 3D image matrix.

4.1.6. Breast specimens

Two breast tissues (sample 1 and sample 2) containing cancer were studied. Both of them were fixed in formalin and sealed in a vacuum bag. The work reported in this paper was carried out following the Directive 2004/23/EC of the European Parliament and of the Council of 31 March 2004 on setting standards of quality and safety for the donation, procurement, testing, processing, preservation, storage and distribution of human tissues. The images presented in this study were acquired in order to guide the pathologist in the localization of the lesions for the histological preparation, according to the standard procedures of the Pathology Unit of the Academic Hospital of Cattinara, Trieste University, accredited by JCI (Joint Commission International). The samples were prepared from specimens of breast lumpectomy and were derived from surgical material sent to the Pathology Unit according to local guidelines for histological examination. Sample 1 contains an infiltrating ductal carcinoma, about 1.5 cm diameter. It is 8 mm thick and it was embedded in agar gel inside a plastic

cup in order to obtain an object with dimension and attenuation comparable to that of a breast section. The diameter of the holder is about 9.4 cm. The acquisition parameters were: air kerma rate 0.52 mGy s^{-1}, 1200 projections equally spaced over 180 degrees in step-and-shoot mode, 50 ms per projection, MGDv equal to 22.8 mGy evaluated with a MC conversion factor 0.73 mGy mGy^{-1}. Sample 2 contains a large (2.5 cm diameter) solid papillary carcinoma (poorly differentiated, G3 grade). Sample dimensions are about 89 × 36 mm^2, 5 mm thickness. Acquisition parameters were: air kerma rate 0.36 mGy s^{-1}, 1200 projections equally spaced over 180 degrees, 50 ms per projection, MGDv equal to 16.6 mGy evaluated with a MC conversion factor 0.77 mGy mGy^{-1}.

4.1.7. Image quality

Figure 4.3 shows the ESF curves for the images obtained without phase retrieval (fig. 4.3a) and with phase retrieval (fig. 4.3b), respectively, for a PMMA-air edge. The first shows fringes (fig. 4.3a) due to the refraction of the X-ray beam; as expected, this phenomenon is not visible after the application of the phase retrieval algorithm (fig. 4.3b). The derivative of the ESF curves produces the LSF curves in fig. 4.4; the phase effects in the ESF obtained without phase retrieval cause dips in the corresponding LSF (fig. 4.4a), at variance with phase retrieval LSF (fig. 4.4b). The high attenuation coefficient of the tungsten wire makes the phase effects less relevant: indeed, fringes are not visible in the presampled LSF evaluated from the wire image (fig. 4.5).
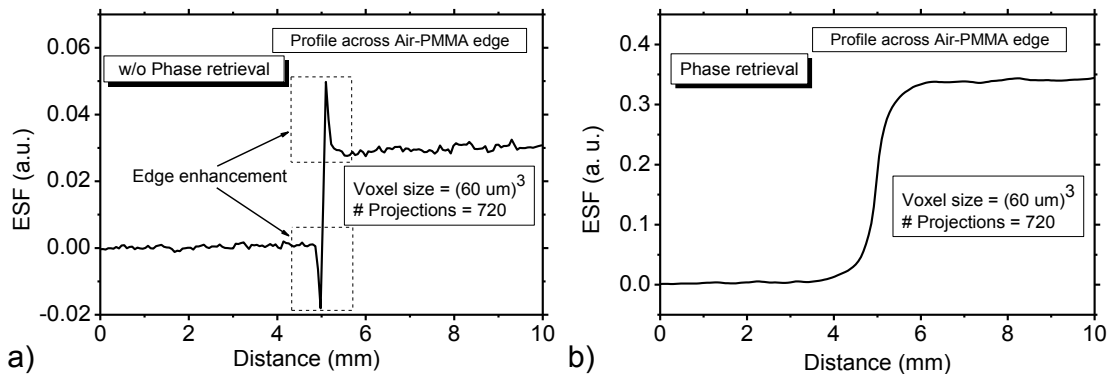
Fig. 4.3. *The ESFs across a sharp PMMA-air edge evaluated on the images without phase retrieval (a) and with phase retrieval (b) averaged over 60 rows. In the image without phase retrieval, the fringes due to phase effects are outlined. Voxel size = (60 μm)^3; number of projections = 720.*

Figure 4.6 shows the system MTF in the images obtained without phase retrieval (fig. 4.6a) and with phase retrieval (fig. 4.6b), evaluated using the PMMA edge. The curves were obtained from 720 projections equally spaced over a 180-deg scan and with an isotropic voxel of (60 μm)^3 and of (120 μm)^3. The edge-enhancement effects cause an increase in the signal, as demonstrated (fig. 4.6a).

Such effects determine MTF curves, which exceed the normalization value at zero spatial frequency. Due to the system spatial resolution reduction, such a phenomenon reduces as the voxel size increases from (60 μm)^3 to (120 μm)^3. Honda *et al* (2006) showed a similar result in

polychromatic propagation based phase-contrast mammography, related to an "improvement of sharpness caused by the edge effect" (Honda *et al* 2006).
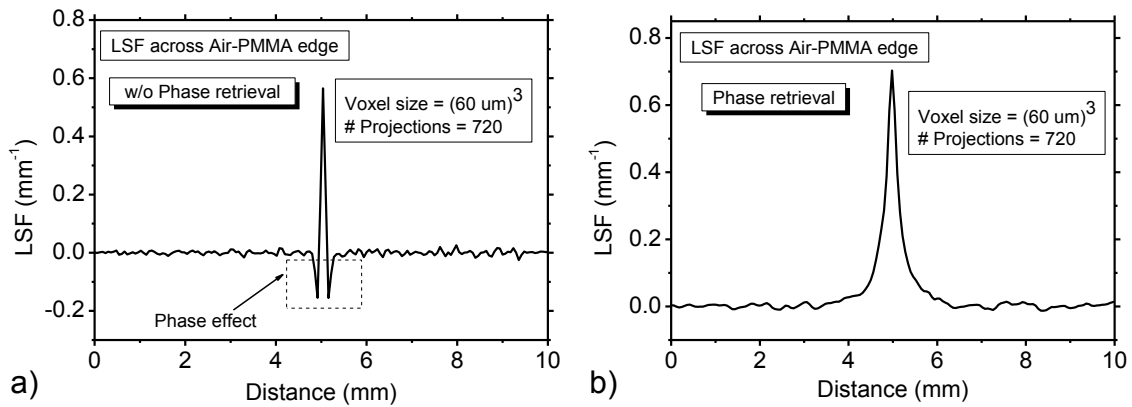
Fig. 4.4. *LSFs evaluated on the images obtained without phase retrieval (a) and with phase retrieval (b) obtained by differentiating the ESF curves in fig. 4.3. The phase-contrast fringes in the ESF without phase retrieval cause dip signals in LSF curve. Voxel size = (60 μm)³; number of projections = 720.*
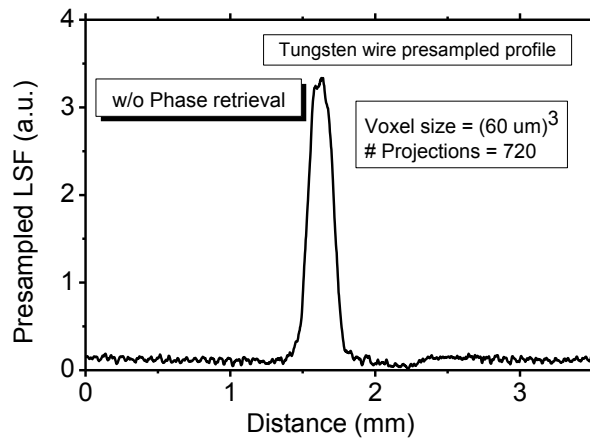
Fig. 4.5. *The presampled LSF evaluated with a 50-μm diameter tungsten wire on the image without phase retrieval. Voxel size = (60 μm)³; number of projections = 720.*
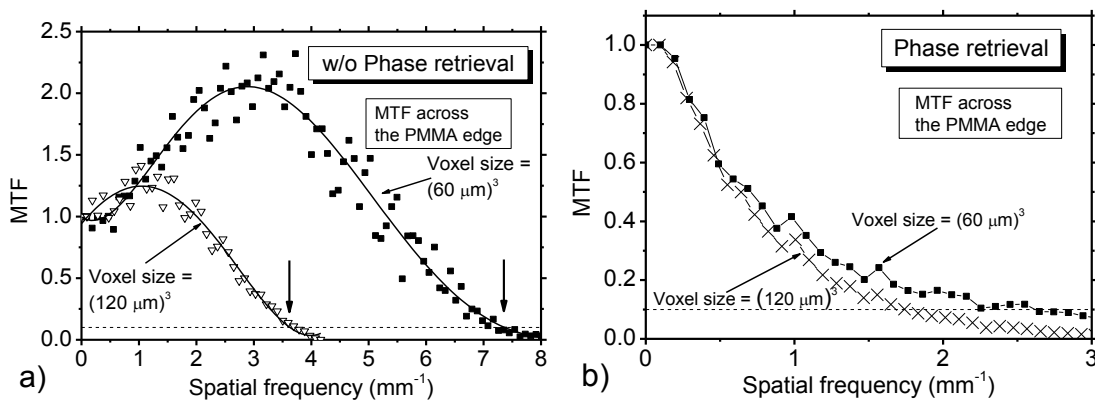
Fig. 4.6. *MTF curves evaluated on the images without phase retrieval (a) and with phase-retrieval (b), evaluated across the PMMA edge, with voxel size of (60 μm)³ and (120 μm)³ obtained with 720 projections equally spaced over 180 deg rotation scan. The dashed horizontal line indicates the 10% MTF value.*

Figure 4.7 shows system MTF curves for the images without phase retrieval (evaluated with the method of the thin tungsten wire) not influenced by the phase effects. In these curves the limiting

frequency at $MTF_{0.1}$ is 6.7 mm^{-1} with voxel of $(60 \ \mu m)^3$; it reduces to 2.5 mm^{-1} (evaluated over the PMMA edge) when a Paganin filter was applied over the projections (fig. 4.6b). Increasing the voxel size to $(120 \ \mu m)^3$ reduces the limiting spatial frequency both in the images without phase retrieval (evaluated with the tungsten wire) and with phase retrieval (evaluated over the PMMA edge) down to 4 mm^{-1} and 1.7 mm^{-1}, respectively. However, the frequency at $MTF_{0.1}$ evaluated with the method of the thin tungsten wire (6.7 mm^{-1} for a voxel size of $(60 \ \mu m)^3$) does not differ significantly from that obtained with PMMA edge (7.2 mm^{-1}); for a voxel size of $(120 \ \mu m)^3$ the limiting frequencies are 4 mm^{-1} and 3.8 mm^{-1}, respectively.

Figure 4.8 shows the MTF curves over a tungsten wire, for the images without phase retrieval, at 10 mm, 30 mm and 50 mm from isocenter. The curves do not significantly differ from each other, and the slight difference can be attributed to the uncertainty in the evaluation.
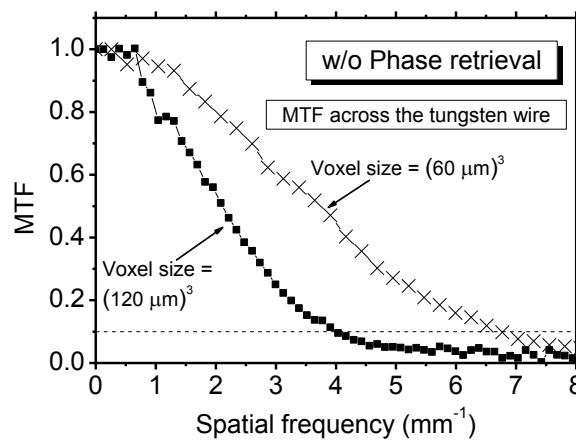
Fig. 4.7. MTF curves for the images without phase retrieval, evaluated over the thin tungsten wire, with voxel size of $(60 \ \mu m)^3$ and $(120 \ \mu m)^3$ and with 720 projections equally spaced over 180 deg rotation scan. The dashed lines indicates the 10% MTF value.
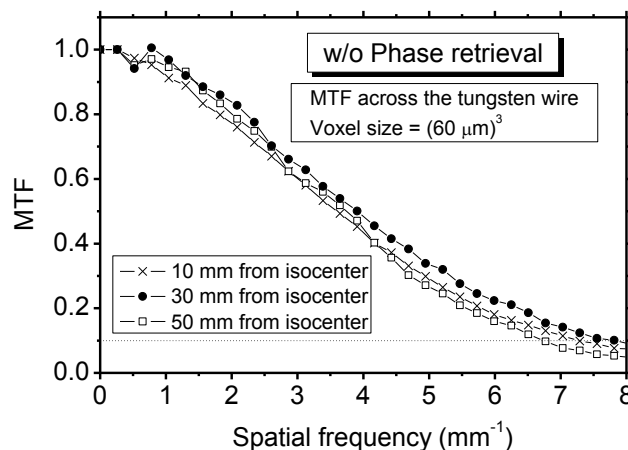
Fig. 4.8. MTF curves for the images without phase retrieval, evaluated over the thin tungsten wire, with voxel size of $(60 \ \mu m)^3$ and 720 projections equally spaced over 180 deg rotation scan at 10 mm, 30 mm and 50 mm from the scanner isocenter.

Figure 4.9 shows the NNPS curves evaluated on the images without phase retrieval (fig. 4.9a) and with phase retrieval (fig. 4.9b). Such curves were evaluated with an image voxel size of $(60 \ \mu m)^3$ as well as for a voxel of $(120 \ \mu m)^3$. Since the (raw processed) detector pixel pitch is 30 μm, the

corresponding signal bandwidth extends up to 16.7 mm^{-1} (Yang *et al* 2008), and in the case of reconstructed coronal pixel pitch of 60 μm and 120 μm, the sampling theorem indicates that signal aliasing may be present, producing signal spectra distortions. This effect was observed in the NNPS curves in the case that the Paganin filter is not applied, where the signal deviates significantly from zero for the highest frequencies (fig. 4.9a). Such a filter is a low-pass filter, which decreases signal noise as well as the influence of aliasing (fig. 4.9b). The voxel size has strong influence on NNPS for the images without phase retrieval: indeed, the maximum of the curve with voxel size of (120 μm)^3 is less than half of the maximum of the curve related to a voxel size of (60 μm)^3. The voxel size had weaker influence on NNPS obtained with phase retrieval. In this case, the NNPS curves show a drastic reduction in the noise level in comparison to that in images obtained without phase retrieval. For a voxel size of (60 μm)^3, the maximum of the NNPS curve in the images without phase retrieval is more than one order of magnitude greater than the maximum of the curve with phase retrieval. Moreover, the first curve presents a maximum at 3 mm^{-1}, and it reduces to about 1 mm^{-1} after the Paganin filter. The noise in phase retrieval imaging, being less prominent at high spatial frequencies than in the case of the images without phase retrieval, may better fit the need of detecting smaller lesions, and balance the reduction in the system spatial resolution due to the Paganin filtering.
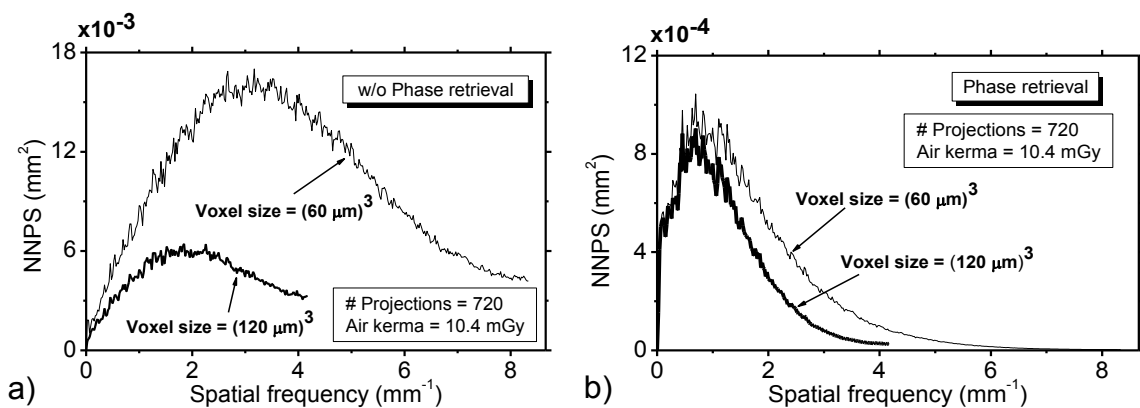
Fig. 4.9. *NNPS in the images without phase retrieval (a) and with phase retrieval (b). They were evaluated both with a voxel size of (60 μm)^3 and of (120 μm)^3 and the reconstructions were performed from 720 projections equally spaced over a 180-deg rotation scan. Air kerma at isocenter = 10.4 mGy.*

Figure 4.10 shows the CNR, as a function of the reconstructed slice thickness, both in the images with and without phase retrieval. The curve obtained in the former case takes values about one order of magnitude greater than that in the latter; in both cases the CNR increases as the slice thickness increases.

Figure 4.11 shows ROIs in CT slices (voxel size = 60×60×360 μm^3) which include the masses of the mammography test object. The CNR between masses and background, evaluated for the mass with a diameter of 3.16 mm, was 45 in the images with phase retrieval (fig. 4.11b) and less than 5 in the images obtained without phase retrieval (fig. 4.11a). The high CNR in phase retrieval makes all the six masses, with diameter ranging from 0.90 to 3.16 mm, visible. The dead spaces between

adjacent detector blocks in the eight-units photon-counting detector cause ring-like artefacts in reconstructed slices and reduces lesions visibility (e.g. lesion 6 in fig. 4.11b).
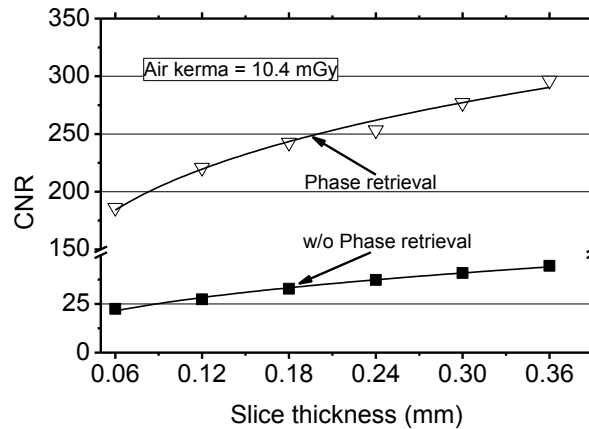
Fig. 4.10. *CNR between glandular and adipose tissue as a function of slice thickness, evaluated on the images without phase retrieval (closed square) and with phase retrieval (open triangles). Air kerma = 10.4 mGy, slice pixel size = 60×60 μm². The continuous lines show a power law fit to the data points.*
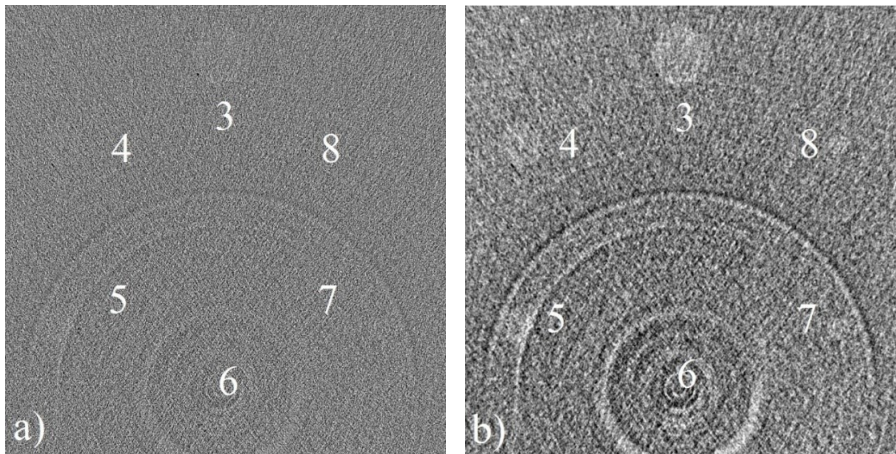
Fig. 4.11. *75% glandular hemispheric masses with radius from 3.16 to 0.90 mm (labels 3-8, respectively), in the images without phase retrieval (a) and with phase retrieval (b). Voxel size = 60×60×360 μm³; 720 projections; air kerma = 10.4 mGy.*

Figure 4.12 shows images of two microcalcification clusters each represented by five $CaCO_3$ specks, with diameter of 160 μm and 130 μm, respectively. In spite of the drastic reduction of the system spatial resolution caused by the Paganin filter, the microcalcification clusters embodied in the mammographic CIRS phantom are visible both in the images without phase retrieval (fig. 4.12a) and with phase retrieval (fig. 4.12b) (voxel size of 60×60×120 μm³). The black halos around the microcalcifications could be ascribed either to phase effects or to reconstruction artefacts. Furthermore, such an artefact might be ascribed to a manufacturing imperfection.

Figure 4.13 shows profiles over three of the five 160-μm microcalcifications labeled in fig. 4.12 as A, B and C, in the images without phase retrieval (fig. 4.13a) and with phase retrieval (fig. 4.13b), respectively. A Gaussian fit of the microcalcification profiles was performed, and then the FWHMs were evaluated from the fitting curves. The FWHMs evaluated for the 160-μm microcalcification profiles are 150 μm and 212 μm, respectively in the images without phase retrieval and with phase

retrieval. Profiles over the microcalcifications of 130-μm size labeled with D and E in fig. 4.12 are shown in fig. 4.14. In this case, the FWHM is 141 μm for the images obtained without phase retrieval (fig. 4.14a) and 207 μm for those with phase retrieval (fig. 4.14b).
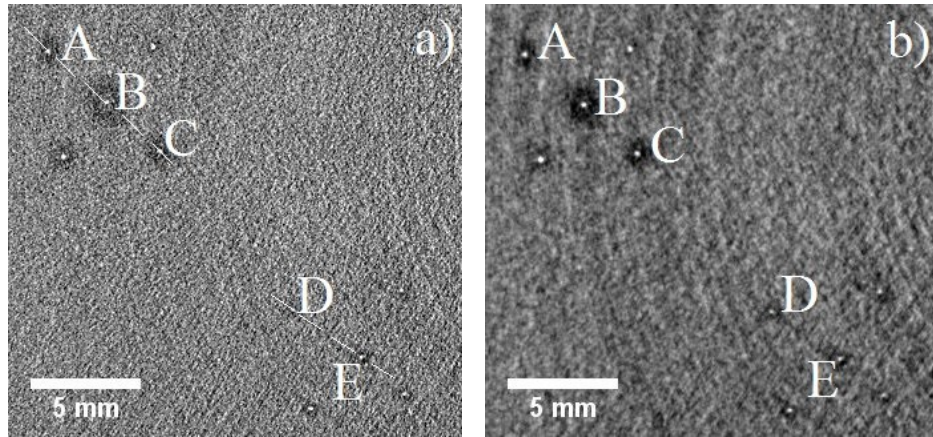
Fig. 4.12. *Microcalcification clusters with CaCO₃ specks of 160 μm and 130 μm in the images without phase retrieval (a) and with phase-retrieval (b). Voxel size = 60×60×120 μm³; 720 projections; air kerma = 10.4 mGy.*
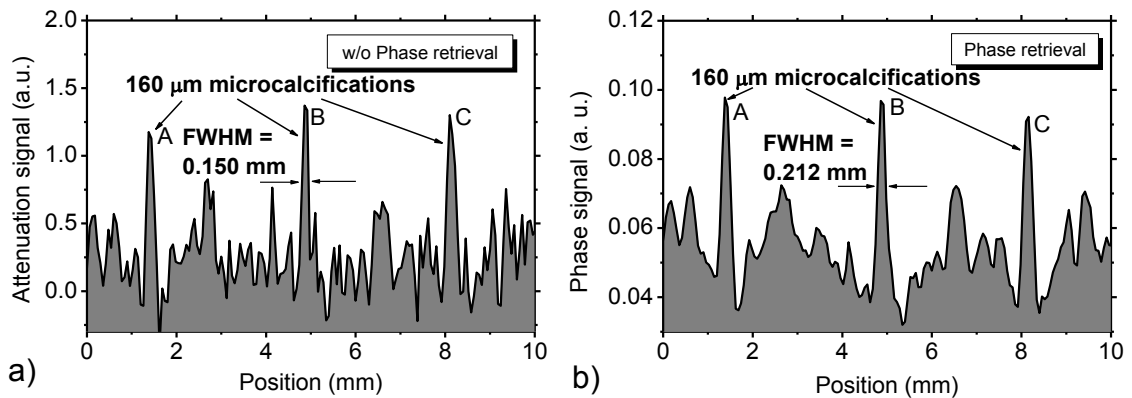
Fig. 4.13. *Profile over the 160-μm microcalcification cluster (dashed line in fig 4.12a), labeled in fig. 4.12 with A, B and C, evaluated on the images without phase retrieval (a) and with phase-retrieval (b). Voxel size = 60×60×120 μm³; air kerma = 10.4 mGy; 720 projections.*
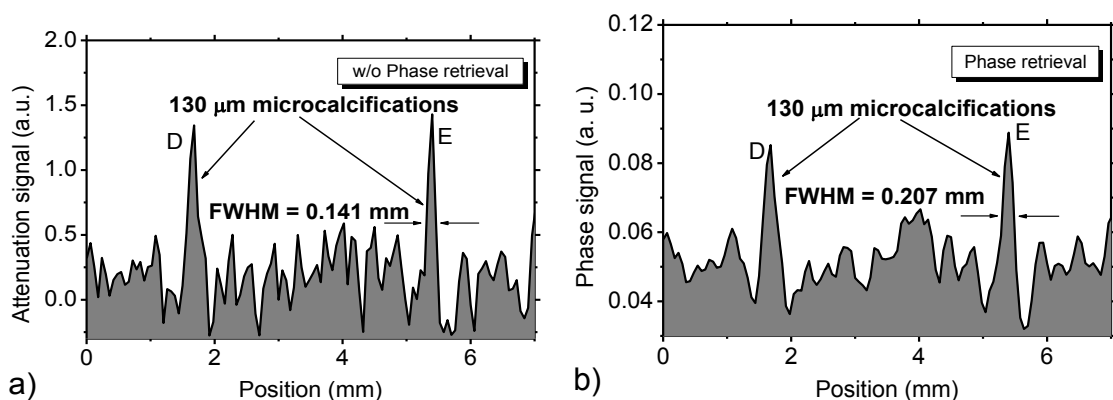
Fig. 4.14. *Profile over the 130-μm microcalcification cluster (dashed line in fig 4.12a), labeled in fig. 4.12 with D and E, evaluated on the images without phase retrieval (a) and with phase-retrieval (b). Voxel size = 60×60×120 μm³; air kerma at isocenter = 10.4 mGy; 720 projections.*

A detail of the mammographic phantom (the step-wedge inclusion) is presented in Fig. 4.15. It is the glandular-fat step-wedge and it is composed by two tissue-equivalent materials, i.e. glandular and fat tissue. The reconstruction in Fig. 4.15a was made using the FBP algorithm without phase retrieval, while the one in Fig. 4.15b was made using a Paganin filter. Figs. 4.15c and 4.15d show the signal intensity profiles of the step-wedge in the figures 4.15a and 4.15b, respectively. It can be observed that phase retrieval yields significant noise reduction. The CNR evaluated on the two tissue-equivalent materials in ROI of 100×100 pixel^2, was 23 for the reconstruction without phase retrieval, and 186 for the one with phase retrieval. The FWHM of the LSF across the edge, which was evaluated through a fit of the edge profiles with the error function (erf), was 310 μm and 375 μm, respectively. It is important to point out that, although the spatial resolution of the reconstruction without phase retrieval is (slightly) higher, it could not allow for recognition of very small details, because of the relevant noise level.
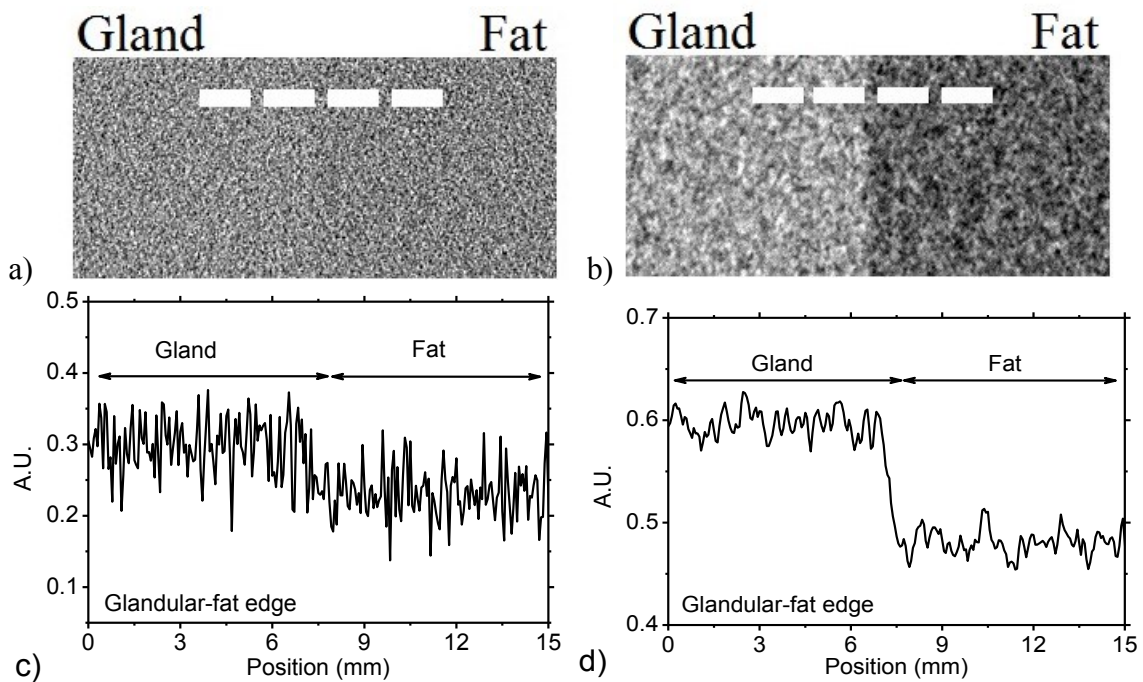
Fig. 4.15. *Glandular-fat step-wedge images without phase retrieval (a) and with phase-retrieval (b) extracted from slices with voxel size of (60 μm)³ reconstructed via FBP algorithm. Profiles across the dashed lines in (a) and (b) in attenuation imaging (c) and with phase-retrieval (d) on average over 100 consecutive rows (Longo et al 2016).*

In principle, it could be possible to reduce the noise level by applying a filter to the reconstructed image, at the cost of a reduction in spatial resolution. Fig. 4.16 compares the FWHM as a function of the CNR for the reconstruction with phase retrieval and for that without phase retrieval, the latter one unfiltered (σ=0) or filtered through a Gaussian filter with varying standard deviation (σ). It can be observed that when the FWHM of the reconstruction without phase retrieval becomes comparable to that with phase retrieval, its CNR is significantly lower.
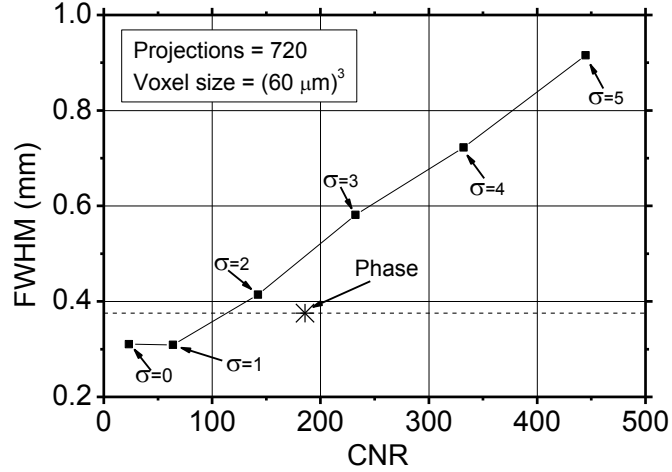
Fig. 4.16 *FWHM vs CNR with different gaussian-filter width applied to the reconstructed image without phase-retrieval compared to CNR and FWHM of the phase-retrieved slice (* symbol) (Longo et al 2016).*

Table 4.I reports the values of the global figure of merit Q for the images without phase retrieval and for those obtained with phase retrieval. Such an index was evaluated for a voxel size of $(60 \, \mu m)^3$ as well as for a voxel size of $(120 \, \mu m)^3$. The Q values indicate weak dependence of the image quality on the voxel size for the former images, where the noise reduction balances the reduction of the spatial resolution; on the other hand, the latter images with voxel size of $(60 \, \mu m)^3$ present a Q index about 2.6 times higher than for a voxel size of $(120 \, \mu m)^3$. Indeed, in this case, increasing the voxel size reduces the system spatial resolution, but determines a weak influence on image noise. Moreover, for a voxel size of $(60 \, \mu m)^3$, application of the phase retrieval algorithm increases Q by about 1.8 times. Hence, in the trade-off between system noise and system spatial resolution, this global figure of merit shows that phase retrieval may improve the system imaging performance.

Table 4.I. *Global figure of merit Q (eq. 4.2), $MTF_{0.1}$ and σ evaluated for the images obtained with and without phase retrieval, with two different reconstruction voxel sizes.*

	Voxel size					
	60×60×60 μm³			120×120×120 μm³		
	σ	MTF$_{0.1}$(mm^{-1})	Q	σ	MTF$_{0.1}$(mm^{-1})	Q
Without phase retrieval	1.15	6.7	1524	0.41	4.0	1523
With phase retrieval	0.12	2.5	2712	0.09	1.7	1031

Figure 4.17 shows the FWHM, for the SART reconstruction, determined across the PC-air edge, for different values of α and ϕ, and fig. 4.18 shows the CNR (evaluated in circular ROI with a diameter of 110 pixels, voxel size = $60 \times 60 \times 60 \, \mu m^3$) between PC and the different inserts in the PC phantom for $\phi = 1 \, cm^{-1}$ and α comprised in the range 2–30 pixel^{-1}. While the range parameter ϕ presents a weak influence both on the system spatial resolution and image CNR, the FWHM evaluated for the PC-air edge increases as α increases (Fig. 4.17). For any examined values of α and ϕ, the SART reconstruction shows FWHM values consistently lower than that obtained with FBP (=

0.85 mm). While an increase of α from 2 to 8 produces a CNR increase up to 21% between ethanol and PC (fig. 4.18); a further α increase causes a lower CNR improvement at the cost of decreasing the system spatial resolution. The best trade-off between CNR and system spatial resolution was observed for $\alpha = 4$ pixel^{-1} and $\alpha = 6$ pixel^{-1}. For comparison, table 4.II shows the CNR value evaluated for the FBP reconstruction and the SART reconstruction coupled with the bilateral filter with $\phi = 1$ cm^{-1} $\alpha = 6$ pixel^{-1}. The iterative reconstruction shows better CNR for all the inserts, but for the glandular tissue where no significant differences can be observed.
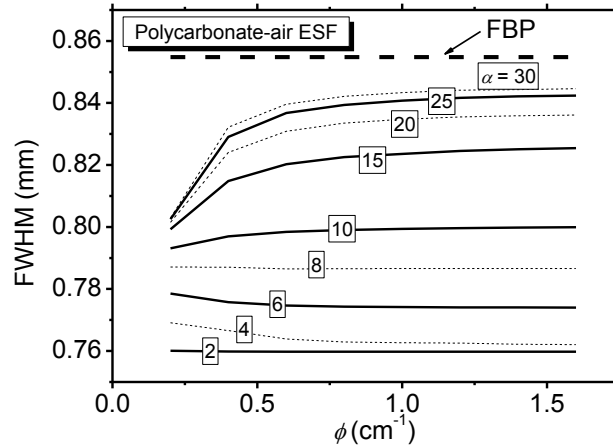
Fig. 4.17. *FWHM evaluated over the PC-air edge for different values of α and ϕ.* Number of projections over 180 deg scan angle = 1200; voxel size = $60 \times 60 \times 60$ μm^3.
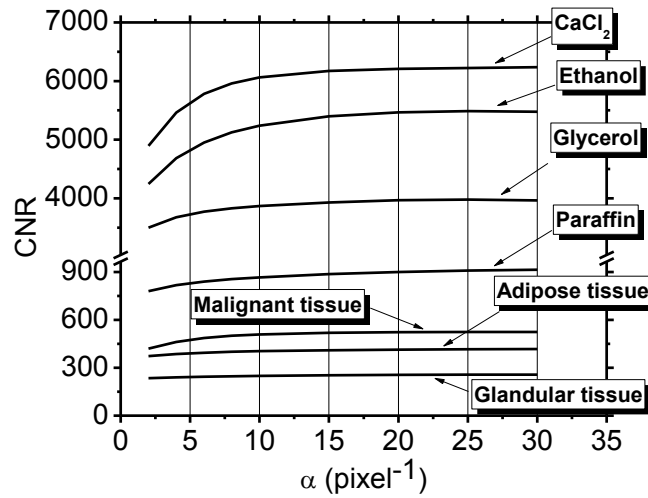
Fig. 4.18. *CNR between PC and CaCl₂, ethanol, glycerol paraffin, malignant tissue, adipose tissue and glandular tissue for model parameters ϕ = 1.0 cm^{-1} and α in the range 2–30 pixel^{-1}.* Number of projections over 180 deg scan angle = 1200; voxel size = $60 \times 60 \times 60$ μm^3.

Table 4.II. *CNR between PC test phantom and embodied inserts for FBP and SART ($\phi = 1.0$ cm^{-1}, $\alpha = 6$ pixel^{-1}) reconstruction and the ratio between the evaluated values. Number of projections over 180 deg scan angle = 1200; voxel size = 60 × 60 × 60 μm^3.*

Insert material	CNR FBP	CNR SART (ϕ=1.0 cm^{-1}, α=6 pixel^{-1})	CNR SART to FBP ratio
Adipose tissue	371	394	1.06
Ethanol	4272	4952	1.16
Glycerol	3334	3772	1.13
Paraffin	680	840	1.24
CaCl$_2$	4771	5781	1.21
Malignant tissue	291	487	1.67
Glandular tissue	245	244	0.99

Figure 4.19 shows the effect of reducing the number of projections (and hence, dose) on the image CNR. Using 600 projections (air kerma at isocenter = 8.4 mGy) instead of 1200 (air kerma at isocentre = 16.8 mGy) does not noticeably reduce the CNR in the case of SART reconstruction, while it drastically affects image quality in the case of FBP reconstruction.
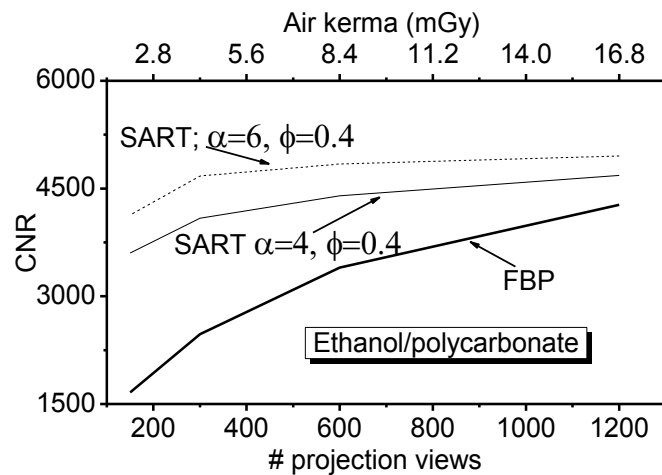
Fig. 4.19. CNR between PC and ethanol as a function of the number of projections (and hence, air kerma at isocenter) for the CT scan, in the case of SART reconstruction ($\phi = 0.4$ cm^{-1}; $\alpha = 6$ or 4 pixel^{-1}) and FBP (air kerma/projection = 14 μGy; voxel size = 60 ×60×60 μm^3).

Figure 4.20 shows CT reconstructed slice of a breast sample 1 obtained with the FBP algorithm without ring correction (Fig. 4.20a) and the corresponding image obtained using SART reconstruction ($\alpha = 4$, $\phi = 1.0$) without (Fig. 4.20b) and with the ring correction (Fig. 4.20c). While such a ring correction does not compromise the system spatial resolution (FWHM for PC-ethanol: with ring correction = 0.75 mm; without ring correction = 0.78 mm; fitting uncertainty = 0.02 mm),

it removes ring artefacts caused by block junctions in the X-ray detector. Moreover, due to the filtering process, the CNR in the test object images was slightly improved.
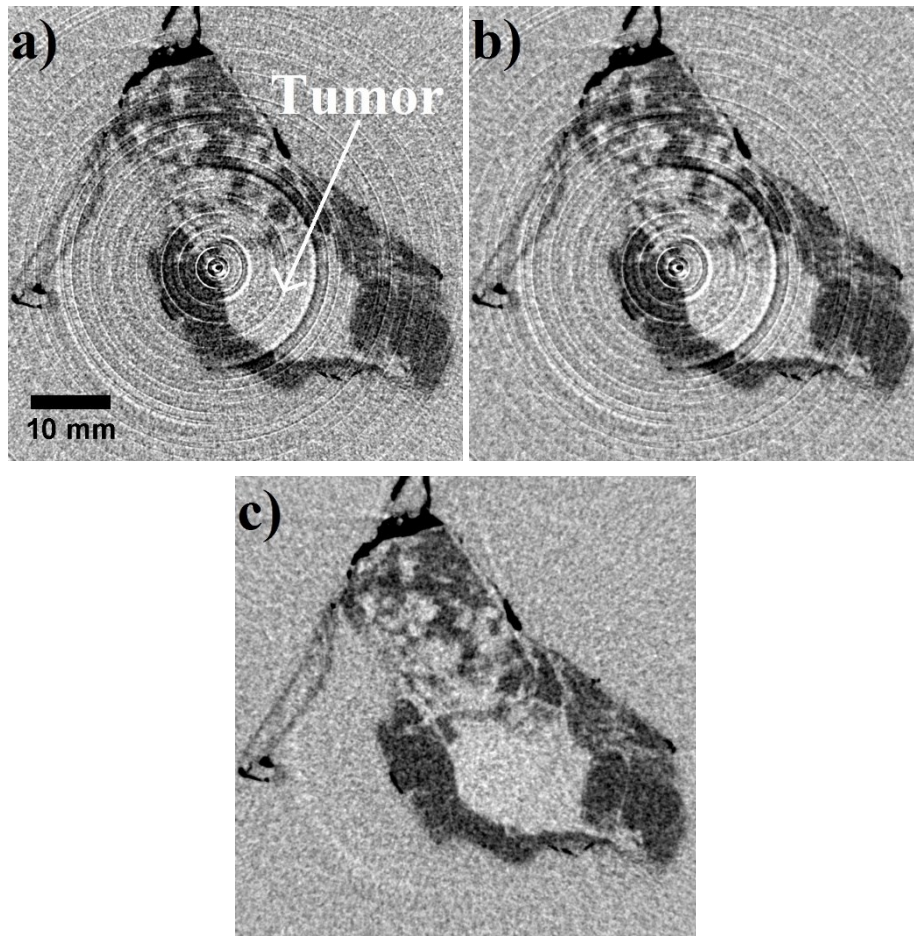
Fig. 4.20. *CT slice of a breast specimen lesion 1, obtained with FBP reconstruction and without ring removal (a), and via SART algorithm ($\alpha = 4$ pixel^{-1}, $\phi = 1.0$ cm^{-1}) without ring correction (b) and with ring correction (c). Air kerma at isocentre = 21.6 mGy; voxel size = 60 × 60 × 60 μm³; 1200 projections over 180 deg.*

In figure 4.21, image reconstructions of the breast sample 1 are presented. The figure 4.21a has been obtained using 1200 projections. The voxel is cubic and pixel pitch of the reconstructed images is 120 μm, in order to balance high spatial resolution and signal-to-noise ratio. The black details inside the object are air bubbles due to the folding of the plastic bag containing the sample; edge-enhancement effects are visible at the interface air-plastic foil. In figure 4.21b FBP reconstruction of 300 projections has been obtained, reducing the MGDv by a factor 4 with respect to figure 4.21a. In figure 4.21c the same 300 projections data set is reconstructed by means of SART ($\alpha = 4$ pixel^{-1}, $\phi = 0.2$ cm^{-1}). The image in figure 4.21d is obtained applying a phase retrieval filter prior to same SART algorithm used in figure 4.21c. Images reconstructed using SART present lower noise and a preserved spatial resolution. In contrast to figures 4.21a-c, in the phase retrieved image (figure 4.21d) the glandular tissue appears brighter than the agar gel surrounding the sample. As expected, the phase retrieved image does not show edge enhancement effects and its noise is significantly reduced. The conventional mammography of the sample 1, before agar gel inclusion, is presented in figure 4.22 to

show the fine parenchymal structures present in the sample. They are visible in both digital mammography and the CT images. However in the latter no overlapping features are presented.
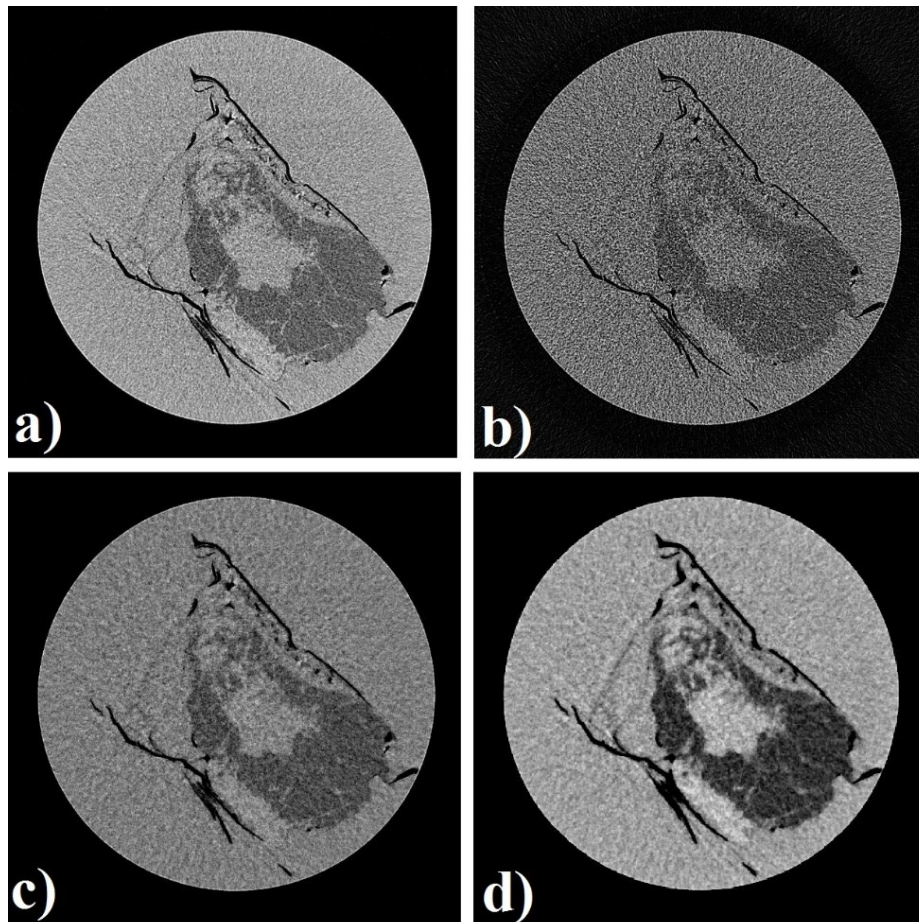
Fig. 4.21. *Sample 1(diameter: 9.4 cm).(a) FBP reconstruction of 1200 projections and (b) 300 projections, (c) SART (α = 4 pixel^{-1}, ϕ = 0.2 cm^{-1}) reconstruction of 300 projections, (d) phase retrieved SART (α = 4 pixel^{-1}, ϕ = 0.2 cm^{-1})reconstruction of 300 projections (Longo et al 2016).*
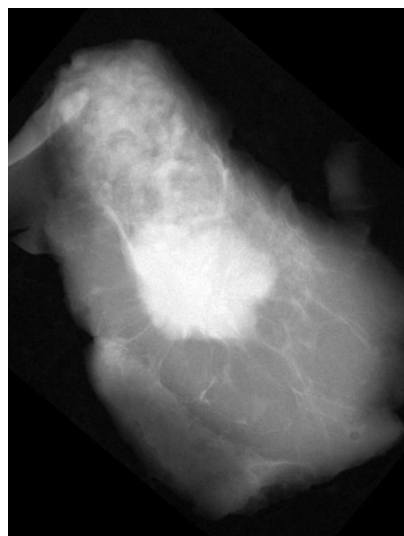
Fig. 4.22. *Digital mammography (planar image) of sample 1 (Longo et al 2016).*

The sample 2 was studied without inclusion in the agar-gel and it was acquired with delivered dose smaller than the MGDv delivered in sample 1 acquisitions. The MGDv was about 16.6 mGy

for 1200 projection over 180 degrees. According to Zhao *et al* (2015) in clinical breast CT, even if the voxel size is smaller than 1 mm, the radiologist during the image evaluation adjusts the slice thickness according to the diagnostic requirements, up to about 2 mm. In order to evaluate the potential clinical application of our low-dose images, 0.84 mm thick slices were obtained adding 7 images from the sample 2 data sets. In figure 4.23 the results are presented for the FBP reconstruction from 1200 phase-retrieved projections (4.23a) and for a low dose reconstruction obtained applying the SART technique on 300 phase retrieved projections (4.23b) with a dose reduction by a factor 4 (MGDv about 4.2 mGy). In figure 4.23c the planar image of the specimen obtained at a clinical mammographic unit is presented; the nodule thickness in the sample in not constant, therefore the contrast modulation inside the cancer in the mammographic image may be due to both its irregular shape and density inhomogeneity of the nodule

In order to quantify the effect of the dose reduction and of the application of the iterative reconstruction contrast and the CNR values were calculated in both image 4.23a and 4.23b. Moreover the possible loss in spatial resolution, due to the reduction in the number of projections for the SART image, has been investigated by measuring the signal profiles at the boundary of the lesion in both image reconstructions. In figure 4.23a, the ROIs selected for the CNR are outlined. The CNR for the FBP reconstruction with 1200 phase retrieved projections is 1.38 times higher than that evaluated for the SART reconstruction with 300 phase retrieved projections, which means that a dose sparing of 75% can be obtained with a CNR reduction of 30%.
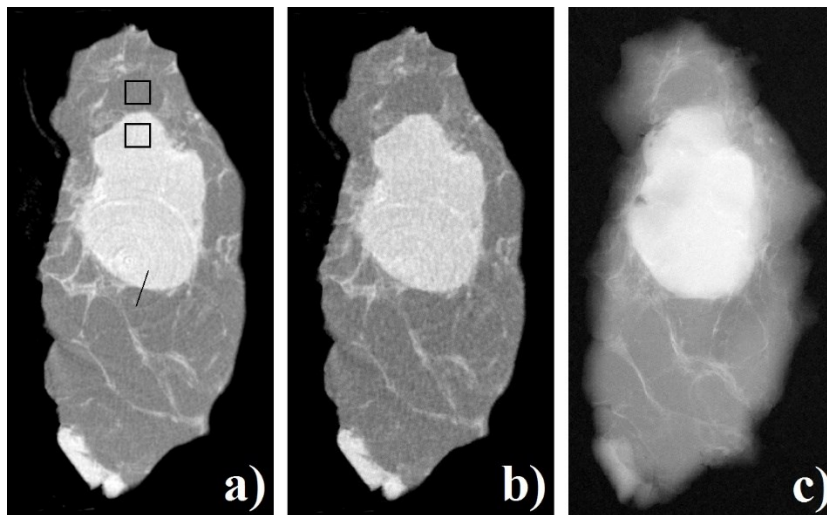
Fig. 4.23. *Images of 0.85 mm thick slices obtained (a) from FBP reconstruction of 1200 phase retrieved projections and (b) SART reconstruction of 300 phase retrieved projections (α = 2 pixel⁻¹, φ = 0.05cm⁻¹). (c) Planar image obtained from the 5-mm-thick sample at a clinical mammographic unit. In (a) the ROIs for CNR are outlined together with the line over which the profiles in fig. 4.20 are evaluated (Longo et al 2016).*

The figure 4.24 shows the signal intensity profiles of the images evaluated across the line in fig. 4.23a and the corresponding line for fig. 4.23b; they presented a FWHM of 420 μm, evaluated as in

the case of the step-wedge insert case, in both cases. These results suggest that the SART technique is a very promising candidate for the tomographic reconstruction of the SYRMA-CT images.
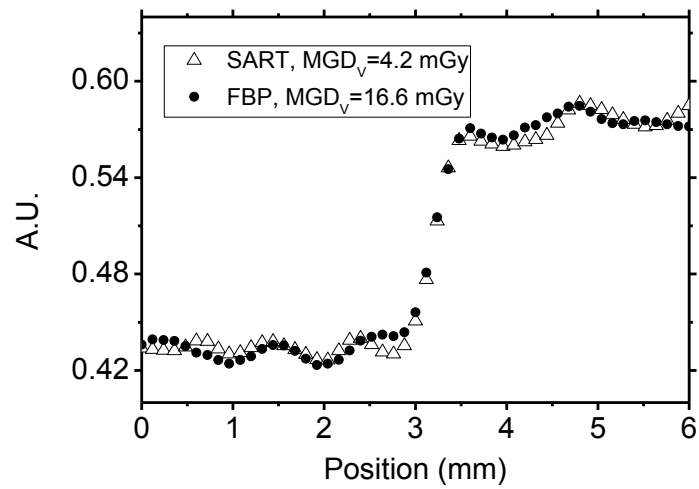
Fig. 4.24. *Profiles across the line in fig. 4.23a, obtained both with FBP reconstruction from 1200 projections and a MGD_V of 16.6 mGy and with SART algorithm ($\alpha = 2$ pixel^{-1}, $\phi = 0.05cm^{-1}$) from 300 projections and a MGD_V of 4.2 mGy. Voxel size = (120 μm)^3 (Longo et al 2016).*

4.2. Phase-contrast breast imaging with a cone-beam micro CT scanner

Although phase-contrast BCT with synchrotron radiation offers high quality images with relatively low dose to the breast it presents some limitations: 1) long scan time due to the small beam dimension in the axial direction and 2) the difficulty to adopt such a technology for general public due to large dimension of the apparatus which relies on synchrotron source. For these reasons we developed a scanner for micro computed tomography dedicated to the breast (BμCT) with a high resolution flat-panel detector and a microfocus cone-beam X-ray tube.

A limit of first-generation BCT scanners is their relatively low spatial resolution, which ranges between 1.7 mm^{-1} and 5.6 mm^{-1}, when evaluated as the spatial frequency at which the modulation transfer function (MTF) curve reaches 10% (MTF$_{0.1}$) (Boone 2001b). For comparison, the limiting resolution of full-field digital mammography (FFDM) reaches 12 mm^{-1} (Monnin *et al* 2007). This relatively low spatial resolution might present problems for the BCT performance in detecting microcalcification clusters. In clinical studies, the BCT systems developed at University of Rochester (O'Connell *et al* 2010) and at University of California Davis (Lindfors *at al* 2008) detected 84.8% and 66.7% of the microcalcification clusters embodied in the imaged breasts, respectively. Several factors limit the maximum BCT system spatial resolution: *i*) the penumbra caused by the large size of the focal spot of the X-ray source (typically in the order of $0.3 - 0.4$ mm nominal), *ii*) the relatively large flat-panel detector pixel pitch (typically about 0.2 mm), *iii*) the blurring introduced by the gantry motion, and *iv*) the scintillator layer of the flat panel detector, usually thicker than that adopted in FFDM, for the need to detect more penetrating photons than in mammography. Many efforts have been made to reduce the influence of these limiting factors. The group at the University of Rochester developed a BCT scanner with a pulsed X-ray source in order to reduce gantry motion influence on the system spatial resolution, which reached 1.9 mm^{-1} (Liu *et al* 2012). The group at UC Davis improved the spatial resolution of its BCT prototype by embodying in the setup a pulsed X-ray tube, a high resolution CMOS flat panel detector with a pixel pitch of 75 μm (which works with an effective pixel pitch of 150 μm) coupled to a thin CsI(Tl) scintillator layer (Gazi *et al* 2013). Thanks to these upgrades, the limiting spatial resolution of the first two prototypes, lower than 1.8 mm^{-1} (Boone *et al* 2010), increased up to 3.6 mm^{-1} for the fourth prototype at UC Davis (Gazi *et al* 2015). The high-resolution, direct-conversion, CdTe photon counting detector allowed the spiral BCT scanner developed at Erlangen University to reach a spatial resolution up to 5.3 mm^{-1} (Kalender *et al* 2016). This gives the potential of showing microcalcifications with a diameter down to 150 μm (Kalender WA 2010, Kalender *et al* 2012).

The medical physics group at the Dept. of Physics at University of Naples "Federico II" developed a first scanner for micro CT dedicated to the breast (BμCT). It embodied a high resolution CMOS flat panel detector with a pixel pitch of 50 μm and a 150-μm thick CsI(Tl) scintillator layer, and an

X-ray source with a micro focal spot of 40 μm nominal size (Mettivier and Russo 2011a). That prototype reached a limiting spatial resolution of 3 mm^{-1} (Mettivier and Russo 2011a). The effective detector pixel pitch, the focal spot size and the spatial resolution of the prototypes developed at UC Davis, Univ. of Rochester, Univ. of Erlangen and Univ. of Naples are summarized in Tab. D.I (in the supplementary material, sect. 9.4.). This work presents the characterization of the new BμCT scanner developed at Univ. of Naples (third prototype, tab. D.I): here, the X-ray tube has been replaced with a micro focal spot (7 μm) tube. Following, the system MTF is described and the 1D noise power spectra (NPS) have been evaluated.

The micro-focal spot of the new scanner developed at U Naples, together with a sufficient distance between source and imaged object, produces an X-ray beam with sufficient spatial coherence, which makes this BμCT scanner a viable tool for PB-PhC for future clinical applications. In this work, the edge enhancement produced by the phase effects, both in planar and in 3D reconstructed images, was investigated.

A phantom study was conducted in order to test the capability of the BμCT scanner in showing phantom microcalcifications and soft tissue lesions with a dose similar to the one used in two-views FFDM and with a long scan time still considered acceptable for in clinical use.

4.2.1. The Cone Beam BμCT system

The cone-beam microCT scanner dedicated to the breast (Fig. 4.25) is a modular benchtop system, which embodies the components described below.

Fig. 4.25. *Cone-beam microCT prototype scanner dedicated to breast imaging. (1) Microfocus X-ray tube and (2) CMOS flat panel detector, mounted on step-motor linear stages for variable-magnification imaging; (3) step-motor rotating gantry; (4) hanging PMMA breast phantom placed at isocenter and simulating a pendant breast; (5) rotating filter wheel for beam shutter; (6) post and lab jack at isocenter for hosting phantoms. Step-motor linear stages (*a-e*) and rotation stages (*f, *g*) are used for setting the acquisition geometry and for gantry rotation. The system is mounted on an optical table (1.8 m × 1.2 m) and the patient bed can be positioned at 154 cm from the floor.*

1) A 75-W microfocus X-ray tube (Hamamatsu model L8121-03) with a selectable focal spot whose size is 7, 20 or 50 µm (5 µm at 4 W tube power). This air-cooled tube has a fixed tungsten anode, a cone angle of 43 deg and it can be operated at a constant voltage between 40 kV and 150 kV; the output window is made of 0.2-mm Be and the added filtration is 1.58 mm Al. The measured half value layer (HVL) at 50 kV is 1.3 mm Al. The distance between source and isocenter is 612 mm. Figure D1 (in the supplementary material, sect. 9.4.) shows the tube output at isocenter as a function of tube voltage. Table 4.III shows the scan time necessary to deliver a mean glandular dose (MGD) of 4 mGy to a 14-cm diameter and 50% glandular breast, calculated on the basis of the tube output at isocenter and on the basis of the monoenergetic DgN_{CT} coefficients evaluated in this work (tab. 4.III, columns E and F). The X-ray spectra were simulated with SpekCalc (Poludniowski *et al* 2009). The duration of a full 360-deg scan is in the range of 135 s (@ 80 kV) to 403 s (@ 40 kV) when the focal spot is set to 7 µm, decreasing correspondingly to 32−193 s with a 50-µm focal spot. For comparison, and in order to evaluate the scan time for higher tube voltage, the same calculation was performed via the DgN_{CT} from Thacker and Glick (2004) and reported in tab. 4.IV. At 80 kV and 40 kV, with a focal spot of 7 µm, the calculated scan time reduced to 102 s and 336 s respectively. Such a difference is due mainly to the different shape of the modeled breast, which is semi-elliptical in the work of Thacker and Glick (2004) so leading to larger DgN_{CT} coefficients. Moreover, extracting data from the graph in Thacker and Glick (2004) could represent a further source of bias. The total scan time necessary to deliver 4 mGy of MGD to a 50% glandular breast (breast diameter = 14 cm, breast height = 10.5 cm) decreases to 69 s and 11 s with 7 µm and 50 µm focal spot, respectively, for 120 kV. Hence, scans in which the patient is holding her breath are not feasible, and patient specific tools capable of immobilizing the breast during the scan are necessary.

2) A CMOS flat panel detector (Hamamatsu mod. C7942CA-02) with a 150-µm thick CsI:Tl scintillator layer, with a sensitive area of 12 cm × 12 cm and a 50−µm pixel pitch. According to specifications, the C7942CA detector has a spatial resolution of 8 lp/mm (at 5% Contrast Transfer Function); the measured MTF reaches 10% at 6 mm^{-1} (Mettivier and Russo 2011a). The detective quantum efficiency of the detector is higher than 0.4 at zero frequency (at 60 kVp, mean energy = 36.3 keV) (Kim *et al* 2005). The frame rate is 2 fps at 1×1 pixel binning (2.13 fps measured rate), 4 fps at 2×2 binning and 9 fps at 4×4 binning. The analog-to-digital conversion produces 12 bit/pixel signals in analog to digital units (ADU). Figure D2a (in the supplementary material, sect. 9.4.) shows the results of a test for assessing the detector lag, confirming the limited relevance of this effect for the CMOS flat panel detector. We acquired four hundred consecutive frames and then calculated the average pixel value in a 400×400 pixels region of interest (ROI). The curves for 50, 80 and 100 kV were normalized to their starting values. The results showed a weak upward trend where the mean signal increases up to 0.7% (at 80 kV) from its starting value after 400 consecutive projections. Previous studies (Mettivier *et al* 2011b) showed an asymptotic trend for this curve. Figure D2b (in

the supplementary material, sect. 9.4.) shows linearity of detector signal (evaluated as the mean value in a 400×400 pixels ROI) as a function of tube loading. The detector shows a mean value of the dark signal of 80.6 ADU. Figure D2c (in the supplementary material, sect. 9.4.) shows the percentage coefficient of variation (COV=100×signal standard deviation/signal mean value) evaluated in a 400×400 pixels ROI as a function of the mean signal, showing little dependence of the COV on the tube voltage.

Table 4.III. The evaluated scan times necessary to deliver 4 mGy MGD to a breast of 14-cm diameter (breast height = 1.5x breast radius) and 50% glandular tissue based on the modeled X-ray spectra, on the monochromatic DgNCT evaluated in this work and on the assessed X-ray tube output. A = tube output at isocenter (μGy/mAs); B = DgNCT for a breast with 14-cm diameter and 50% glandular fraction (mGy/mGy); C = max tube current (mA) for 7-μm focal spot; D = max tube current (mA) for 50-μm focal spot; E = scan time (s) with 7-μm focal spot; F = scan time (s) with the 50-μm focal spot.

kV	A Tube output (μGy/mAs)	B DgN_{CT} (mGy/mGy)	C I_{max} – 7 μm (mA)	D I_{max} – 50 μm (mA)	E Scan time – 7 μm (s)	F Scan time – 50 μm (s)
40	141.6	0.29	0.240	0.500	403	193
50	228.0	0.36	0.200	0.500	245	98
60	315.8	0.41	0.160	0.500	193	62
70	407.0	0.45	0.140	0.500	155	43
80	501.0	0.49	0.120	0.500	135	32

Table 4.IV. The evaluated scan times necessary to deliver 4 mGy MGD to a breast of 14-cm diameter breast height = 1.5x breast radius) and 50% glandular tissue based on the modeled X-ray spectra, on the monochromatic DgN evaluated by Thacker and Glick (2004) and on the assessed X-ray tube output. A = DgNCT for a breast with 14-cm diameter and 50% glandular fraction (mGy/mGy); B = scan time (s) with 7-μm focal spot; C = scan time (s) with the 50-μm focal spot.

kV	A DgN_{CT} (mGy/mGy)	B Scan time – 7 μm (s)	C Scan time – 50 μm (s)
40	0.35	336	161
50	0.45	195	78
60	0.54	147	47
70	0.60	117	33
80	0.65	102	25
90	0.70	87	19
100	0.73	78	16
110	0.76	72	13
120	0.79	69	11

3) The mechanical hardware is composed of two rotating arms hosting the detector and the X-ray tube, respectively: during the scan they describe a circular path in the coronal plane. Five computer-controlled step-motor linear stages (items *a-e* in fig. 4.25) and one rotation stage (item *f* in fig. 4.25) (Velmex Inc., Bloomfield, NY, USA, Bi-Slide series) allow the independent setting of the source-to-isocenter distance, detector-to-isocenter distance, lateral displacement of the X-ray tube and of the detector, height of the detector with respect to the fixed focal spot height and rotation of the detector around a horizontal axis for the detector alignment with the axis of rotation. Hence, the image magnification factor can be varied, and offset-detector geometries can be adopted (Mettivier *et al* 2012). A high-torque step-motor rotation stage (item *g* in fig. 4.25) (Newport Corp. mod. RV240) is used for gantry rotation.

4) A custom software has been realized using ANSI-C in a LabWindows/CVI (National Instruments) environment in order to control acquisition procedures and to set the scanner geometry.

5) A commercial software (COBRA v.6.8.2, EXXIM Computing Corp., Pleasanton, CA, USA) is used for 3D reconstruction. It allows the implementation of FDK algorithms (Feldkamp *et al* 1984) with different filter-kernels, taking into account geometric calibration parameters of the scanner.

4.2.2. Measurement of the system 3D MTF and NPS

A thin gold wire (25 μm diameter) was imaged in order to simulate a point input to the system. The images were sampled in the direction perpendicular to wire length to extract the point spread function (PSF). Using PSF Fourier transform, the MTF was evaluated. With the purpose of reducing aliasing in MTF assessment we estimated the presampled PSF (Mettivier and Russo 2011a, Boone 2001b, Kwan *et al* 2007).

Cone beam CT resolution changes with distance from the isocenter and with cone angle: many measurements in different points of the FOV are necessary to achieve thorough system spatial resolution characterization. Moreover the spatial resolution depends on the spatial direction: different acquisitions are necessary with different wire orientations to assess resolution in vertical direction (parallel to the rotation axis), radial direction (from the isocenter to the FOV periphery) and tangential direction (perpendicular to the others) (Mettivier and Russo 2011a, Yang *et al* 2007).

A PMMA frame, holding several parallel gold wires, placed both in the coronal plane and perpendicular to them, was predisposed to obtain an exhaustive system characterization by one single acquisition sequence. The wires were spaced 10 mm apart and tilted by about 2 deg and the phantom was placed at the system isocenter. Since the PSF is well described by the Gaussian function (Nickoloff *et al* 1985), a Gaussian fitting was performed before the Fourier transform, to reduce artefacts and noise.

In order to characterize the noise properties of the CT scans, we evaluated the system NPS. We selected a region of interest (ROI) of 35×35 mm^2 in a reconstructed coronal slice of the uncompressed breast phantom (described in sect 4.2.5), where both masses and calcification clusters

were not present. In order to avoid ring artefacts caused by defective detector columns, as well as cupping artefacts by scattering and beam hardening, we selected a second ROI at 0.4 mm from the first one along the direction of the rotation axis. The latter ROI was subtracted from the former and the 2D NPS was evaluated as proposed by Yang *et al* (2008). The 1D NPS was evaluated by performing the radial averaging of the 2D NPS.

4.2.3. Acquisition sequences

We evaluated the system MTF at two different magnification factors, $M = 1.21$ (attenuation based imaging) and $M = 1.93$ (phase contrast imaging), keeping constant the source–to–isocenter distance at 612 mm (and then the lateral coherence of the X-ray beam). In order to have a larger FOV, we performed two times the acquisition at $M = 1.21$ with the detector shifted by 10 cm horizontally in the second acquisition run. The two projection sets were joined into one with a dimension of 3648×2344 pixels per projection matrix so allowing for a reconstructed volume of 150×150×95 mm³. In phase contrast imaging, 360 projections equally spaced over 360 deg were acquired in a single scan and a volume of 58×58×60 mm³ was reconstructed. In order to have reconstructed images with low noise level, high dose acquisitions were performed. The air kerma at the detector plane for each projection was 0.1 mGy in both cases. The tube voltage was fixed at 50 kV and the focal spot size was 7 μm.

4.2.4. Phase contrast and edge-enhancement

The micro focal spot (7 μm) and the sufficient distance from source to object (612 mm) determined a lateral coherence length of 3.5 μm of the X-ray beam in the object plane. The magnification factor of 1.93 with a distance between object and detector of 572 mm permits sufficient X-ray propagation in order to produce some degree of phase effects in detector space. Following the notation introduced by Wu and Liu (2007), the ratio between the shearing length and the lateral coherence length, for a structure component of spatial frequency of 10 mm⁻¹, is 0.034, i.e. sufficiently less than 1 to make phase contrast effects visible in this setup.

Figure D4 in the supplementary material, sect. 9.4., shows the area under the curve of the Relative Phase-Contrast Factor (RPF) (Wu and Liu 2003) evaluated as follows:

$$RPF\ area = \int \left(c^2 h^2 * \left(\int \frac{\pi R f^2}{ME^2} S_{ext}(E) dE \right) * MTF_d(f) * MTF_s(f) \right) df \qquad (4.3)$$

where c is the speed of light, h is the Planck constant, R is the distance between the object and the detector, E is the photon energy, f is the spatial frequency, and $MTF_d(f)$ and $MTF_s(f)$ are the detector MTF and the modulus of the focal spot optical transfer function, respectively. The focal spot was modeled as a 2D Gaussian curve. $S_{ext}(E)$ is the normalized X-ray spectrum at the exit surface of the irradiated object. The curves in fig. D4 were evaluated in cases where no beam shaping is introduced by objects, and in the cases where the X-ray beam passes through a 5-cm or a 10-cm water layer. For

a focal spot size of 7 μm, such functions monotonically increase in the considered range of object-to-detector distances. In our setup, in order to have a tradeoff between the transferred phase signal and the FOV, the distance between the irradiated object (isocenter) and the detector was set to 572 mm.

The presence of phase effects was quantified via the edge enhancement index (EEI) and edge enhancement to noise ratio (EE/N) presented by Donnelly *et al* (2003) and defined below:

$$EEI = \frac{(P-T)/(P+T)}{(H-L)/(H+L)} \qquad\qquad EE/N = \frac{P-T}{\sqrt{\sigma_H{}^2 + \sigma_L{}^2}} \tag{4.4}$$

Here, P is the peak intensity and T is the trough intensity at the edge; H and L are the intensities that at these locations in the absence of edge; σ_H and σ_L represent the standard deviation of the pixels in the region of interest used to calculate H and L values, respectively.

4.2.5. Breast phantom study

We conducted a phantom study in order to evaluate the performance of the BμCT scanner in continuous mode and with low radiation dose. The continuous mode acquisition reduces the MTF in the tangential direction at the periphery of the FOV but it does not influence the system spatial resolution in the radial direction (Yang *et al* 2007). The anthropomorphic breast phantom used in such a test is the mod. 1272-00-00 by CIRS Inc. (Norfolk, VA., USA) (fig. D3 in the supplementary material, sect. 9.4.). It embodies simulated soft masses (with attenuation coefficient similar to that of 100% glandular breast tissue) with diameters from 1 mm to 10 mm and microcalcification clusters. The phantom diameter at the chest wall is $\cong$ 11 cm and the nipple-to-chest distance is 82 mm. The phantom composition presents an attenuation coefficient similar to that of a 50% glandular breast tissue. It is worth noting that, although the used phantom is appropriate in attenuation based imaging evaluation, its physical properties in phase-contrast imaging (i.e. the real part of the material refractive index) are unknown.

A number of 300 projection views, equally spaced over 360 deg, was acquired in 141 s (effective detector frame rate, 2.13 Hz; tube current, 200 μA; tube voltage, 50 kV). This is the maximum number of projections that the frame grabber can acquire in continuous mode before filling the memory buffer, for the 5.2 Mpixel images of the flat panel. The total air kerma at the isocenter was 6.30 mGy (2.27 mGy MGD for 50% glandular breast with a diameter of 14 cm from DgN_{CT} of sect. 3.1).

4.2.6. 2D images quality

Figure 4.26a shows a projection of the MTF phantom. It was collected at magnification $M = 1.21$. Figures 4.26b and 4.26c show line profiles across horizontal and vertical wires, respectively, evaluated across dashed white lines in fig. 4.26a. The distances in the detector plane were scaled to the object plane by using the measured magnification. Figure 4.26d shows a horizontal profile across

a PMMA edge indicated by the white rectangle in fig. 4.26a. Phase effects are not visible either in wire profiles or in the PMMA edge profile.

Figure 4.27a shows a projection of the MTF phantom acquired at $M = 1.93$. Figure 4.27b shows a horizontal profile (with distances scaled to the object plane) evaluated across the dashed white line in fig. 4.27a. Figure 4.27c shows a horizontal profile (averaged over 20 rows) across a PMMA edge indicated by the white ROI in fig. 4.27a. The PMMA edge enhancement is more prominent in this case than for 1.21 magnification: the EEI index was 1.115 and the EE/N was 5.09. Phase-contrast effects are not visible in the profiles of the gold wires.
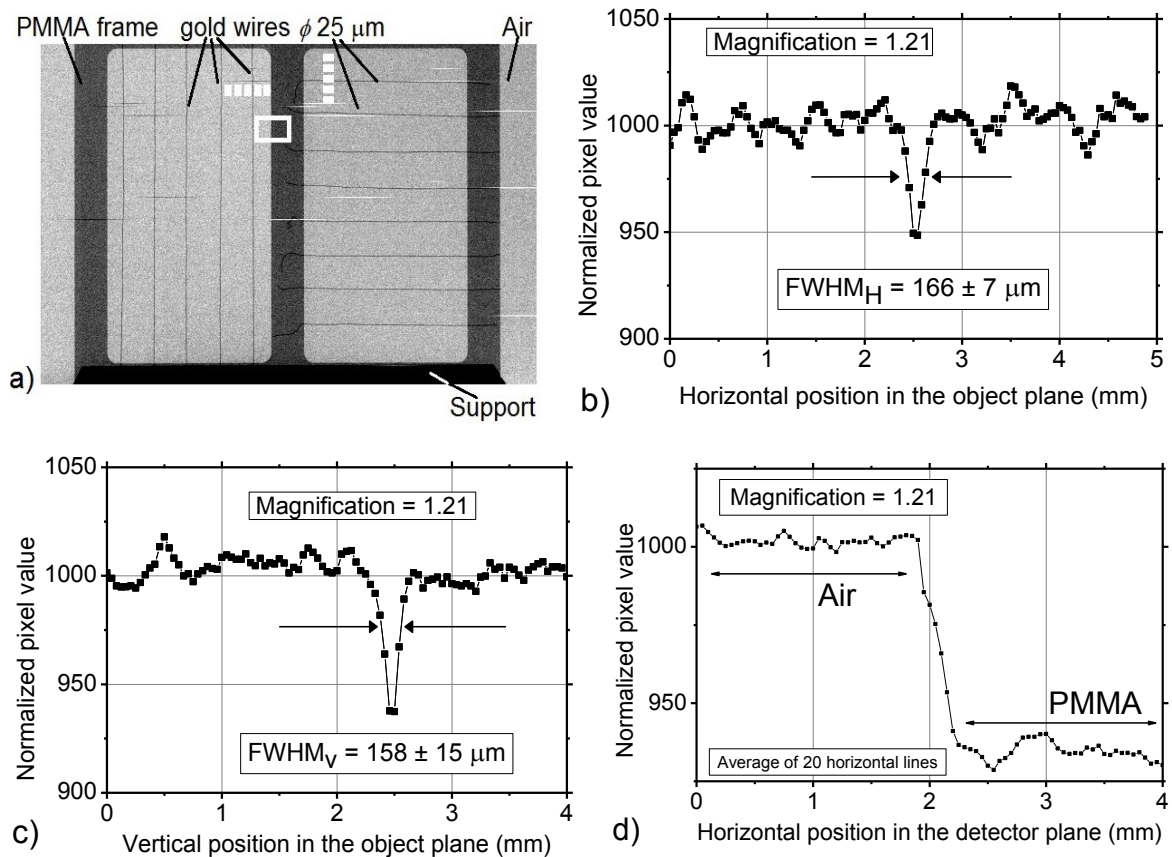
Fig. 4.26. *a) A projection of the MTF test object (3648×2344 pixels, 50 kV, M = 1.21). After flat-field correction of the raw images, the pixel values have been normalized to the arbitrary value of 1000. b) Horizontal and c) vertical profiles drawn along the two line segments indicated by the dashed white lines in (a), across the 25-μm gold wires. d) Horizontal line profile, an average of 20 consecutive horizontal rows, across the edge of the PMMA frame evaluated in the ROI indicated in (a). The distances in the detector plane were scaled to the object plane by using the measured magnification.*
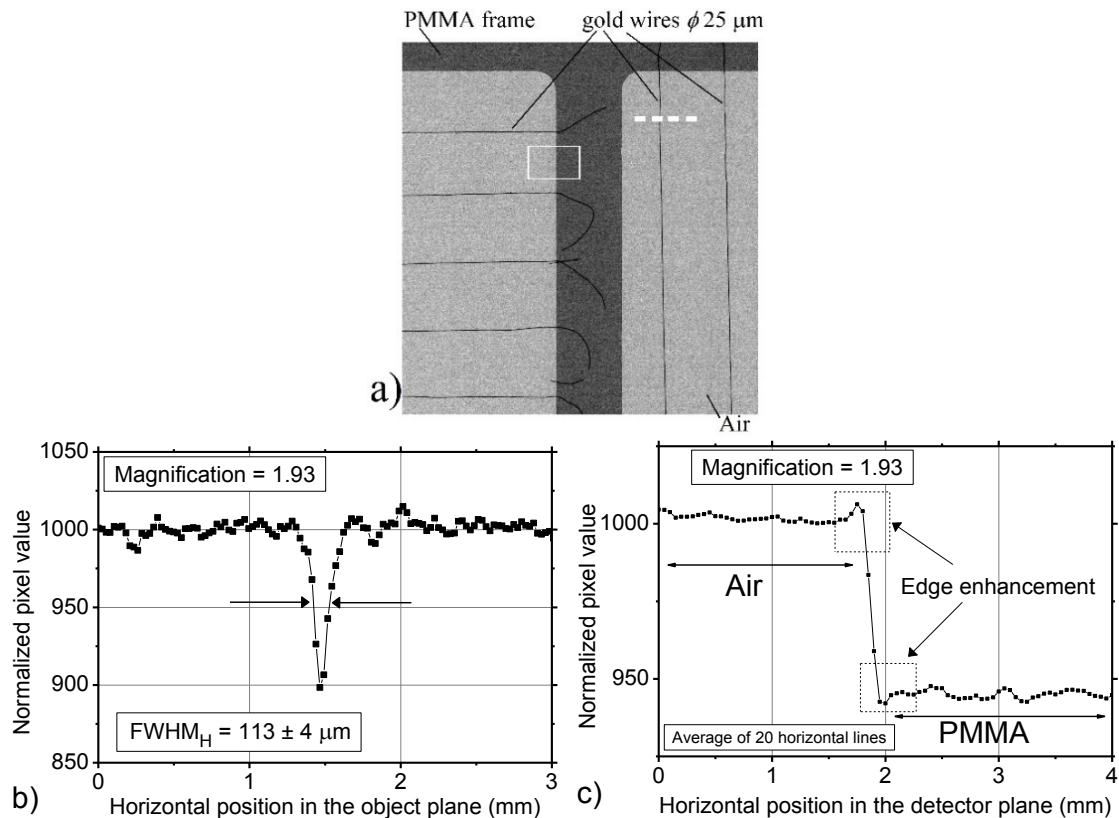
Fig. 4.27. *a) Sample projection (2240x2344 pixels) of the MTF test object. b) Horizontal line profile of a vertical wire (the distances in the detector plane were scaled to the object plane by using the measured magnification). c) Horizontal profile, an average of 20 consecutive horizontal rows, across the edge of the PMMA frame. It shows edge enhancement effects related to propagation based phase contrast.*

4.2.7. 3D images quality

Figure 4.28 shows reconstructed slices of the MTF phantom. Coronal (fig. 4.28a), axial (fig. 4.28b) and sagittal (fig. 4.28c) slices are shown. The magnification factor is 1.21 and 1440 projections were acquired. Figure 4.28 shows the three spatial directions along which MTF assessment was performed. Figures 4.29a and 4.29b show presampled radial and vertical PSFs at 1.8 deg cone angle and at 10 mm from isocenter. The FWHM of the radial profile was 220 μm and the FWHM of the vertical profile was 128 μm.
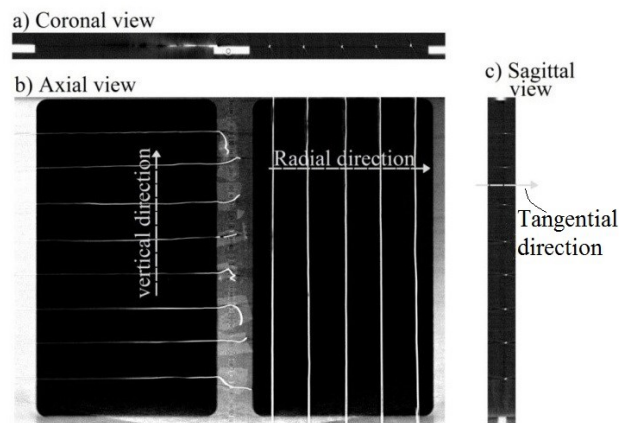
Fig. 4.28. *Reconstructed slices of the MTF test object (1440 views, M = 1.21, slice thickness of 50μm). Coronal (a), axial (b) and sagittal (c) slices. The arrows show the direction for the evaluation of radial, vertical and tangential MTF curves.*
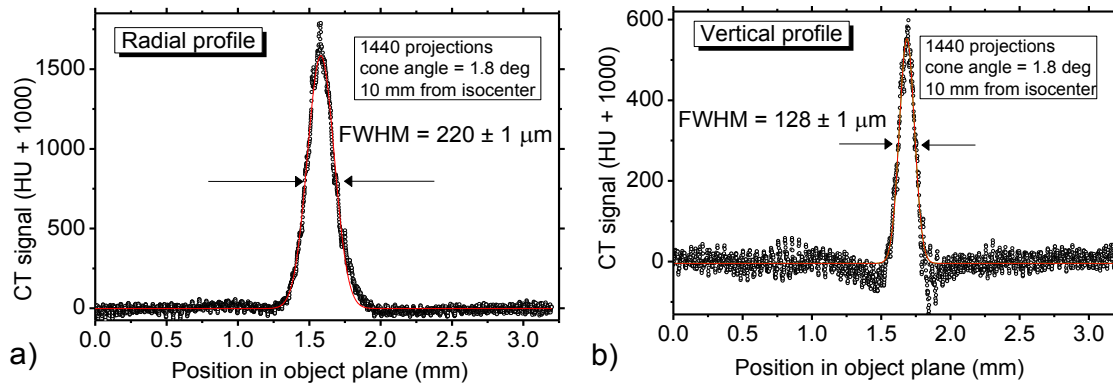
Fig. 4.29. *The presampled radial (a) and vertical (b) wire profiles at 1.8 deg cone angle and 10 mm from the isocenter. M=1.21, 1440 views. Continuous lines (in red) are Gaussian fit of the profiles. The radial profile presents a full width at half maximum of 220 µm, larger than that showed in the vertical profile (128 µm).*

Tables D.II and D.III (in the supplementary material, sect. 9.4.) show the $MTF_{0.1}$ in the radial, vertical and tangential directions (1440 projections, $M = 1.21$, voxel size $= 50 \times 50 \times 50$ μm^3). The $MTF_{0.1}$ in the radial direction decreases as the X-ray cone beam angle increases. Specifically, at 10 mm from the isocenter, $MTF_{0.1}$ decreases from 3.8 mm^{-1} (cone angle, 1.8 deg) to 2.5 mm^{-1} (cone angle 5.6 deg). In the same direction, the $MTF_{0.1}$ decreases to 3.1 mm^{-1} at 1.8 deg cone angle and at 50 mm from the isocenter. The MTF curves in the vertical direction show strong dependence on the cone angle aperture. $MTF_{0.1}$ ranges between 6.2 mm^{-1} at 1.8 deg cone angle down to 4.0 mm^{-1} at 5.6 deg; $MTF_{0.1}$ decreases to 5 mm^{-1} at 50 mm from the isocenter at 1.8 deg cone angle. The tangential MTF has a weak dependence on the cone angle: the slight differences shown in tab. D.III(in the supplementary material, sect. 9.4.), last column, could be ascribed to the statistical uncertainty in the measured data. The tangential $MTF_{0.1}$ decreases as the distance from the isocenter increases, ranging between 3 mm^{-1} (at 10 mm from the isocenter) and 2.1 mm^{-1} (at 50 mm from the isocenter), at 1.8 deg cone angle.

Reconstructing the 3D volume with 360 projections instead of 1440 does not affect the MTF curves significantly, both in radial and vertical directions; a reduction in the number of the projections produces a weak influence in the tangential direction. In this case, the $MTF_{0.1}$ at 10 mm from isocenter and at 1.8 deg cone angle aperture decreases from 3 mm^{-1} for 1440 projections down to 2.8 mm^{-1} for 360 projections (fig.4.30). For comparison, the UC Davis group showed that the slight difference between MTF curves of the BCT scanners obtained with different number of projections was not statistically relevant (Gazi *et al* 2015).

Figure 4.31 shows how the MTF curves depend on the system magnification factor. The MTF was evaluated at 1.8 deg cone angle and at 10 mm from the isocenter. The magnification does not influence the MTF in the tangential direction. The $MTF_{0.1}$ in the vertical direction reduces from 6.2 mm^{-1} to 4.9 mm^{-1} by increasing the magnification from 1.21 to 1.93. Increasing the magnification causes a reduction in the system MTF also in radial direction: $MTF_{0.1}$ is 3.8 mm^{-1} in case of $M = 1.21$ and 3.3 mm^{-1} for $M = 1.93$.
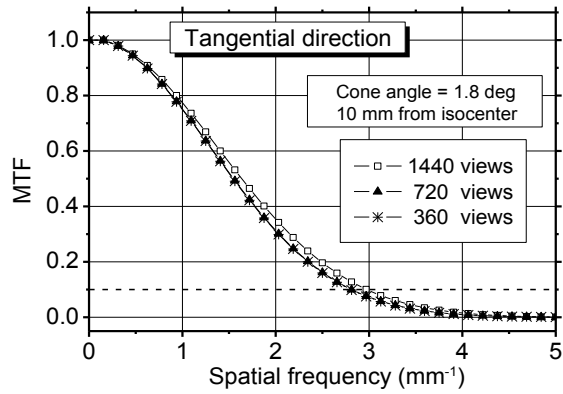
Fig. 4.30. *Tangential presampled MTF curves evaluated by reconstructing 3D images with 360, 720 and 1440 equally spaced projections. Cone angle = 1.8 deg; 10 mm from the isocenter; M = 1.21, voxel size = 50×50×50 μm³.*
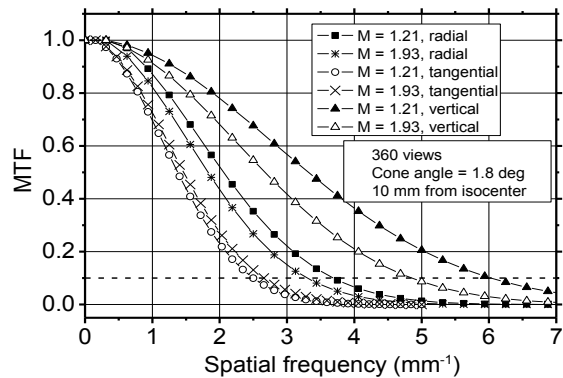
Fig. 4.31. *MTF at different magnification factors (1.20 and 1.93), at 10 mm from the isocenter and at 1.8 deg cone angle aperture; 360 projections, voxel size = 50×50×50 μm³.*

The voxel size has a strong influence on the spatial resolution, which reduces as the voxel size increases (fig. 4.32). In the radial direction (at 10 mm from isocenter, cone aperture of 1.8 deg, 360 projections and $M = 1.93$) the $MTF_{0.1}$ is 3.3 mm^{-1} for a voxel size of (50 μm)^3, and it reduces to 2.5 mm^{-1} and 1.5 mm^{-1} for a voxel size of (100 μm)^3 and (200 μm)^3, respectively.
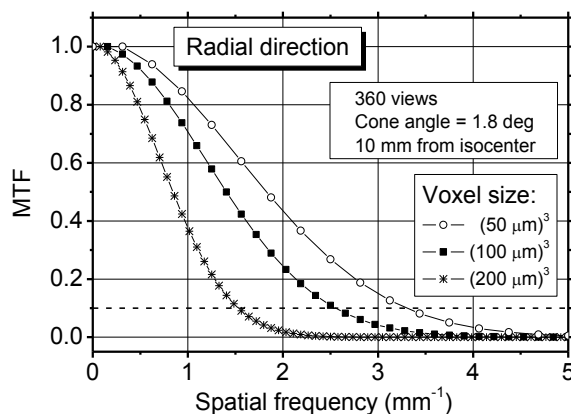
Fig. 4.32. *MTF at different effective voxel size (50×50×50 μm³, 100×100×100 μm³ and 200×200×200 μm³), at 10 mm from the isocenter and at 1.8 deg cone angle (360 projections).*

Figure 4.33 shows radial profiles (averaged over 40 horizontal lines) across a PMMA edge in attenuation imaging (fig. 4.33a) and in phase contrast imaging (fig. 4.33b). The voxel size was (50

μm)^3 and the reconstruction was performed with 360 projections. For M = 1.21, there are no phase effects that may cause contrast enhancement. On the other hand, phase contrast in projections (fig. 4.27c) causes a slight edge enhancement in the reconstructed volume (fig. 4.33b). Due to the absence of phase effects for M = 1.21, the EEI in 3D attenuation imaging was 1.00, whereas in phase contrast imaging EEI = 1.20: this indicates an edge enhancement of about 20% by increasing the magnification from 1.21 to 1.93. The EE/N (EE/N$_{M=1.21}$) in attenuation imaging was 13.14 (in this case it corresponds to the contrast to noise ratio); when M = 1.93 (EE/N$_{M=1.93}$) it was 18.36. The relative EE/N ((EE/N$_{M=1.93}$)/(EE/N$_{M=1.21}$)) was 1.40.
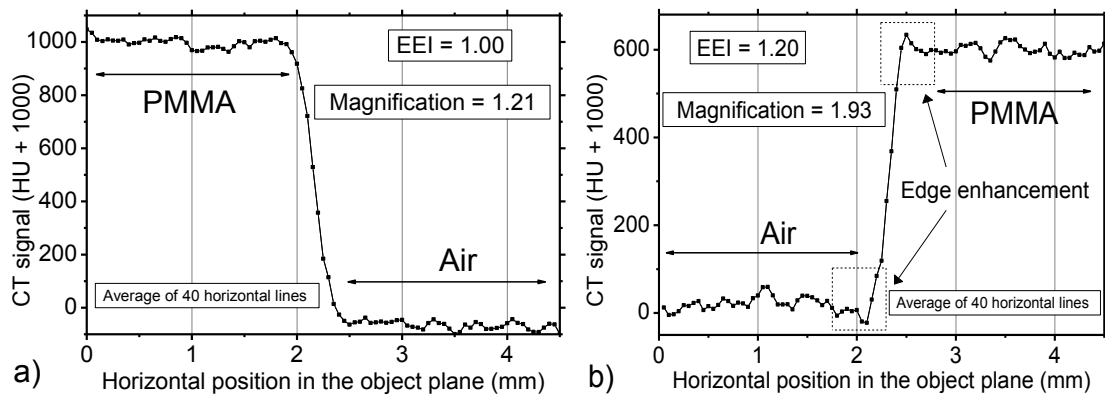
Fig. 4.33. *Horizontal line profiles across the edge of the PMMA frame in 3D images. 360 projections; voxel size = 50×50×50 μm^3. a)* M *= 1.21: invisibility of phase-contrast fringes in projections (fig. 4.26d) reflects the behavior in 3D slices. b)* M *= 1.93: phase-contrast in projections (fig. 4.27c) causes edge enhancement in 3D images.*

Figure 4.34 shows reconstructed coronal slices (voxel size = 200×200×200 μm^3) of the CIRS phantom in correspondence to the black arrows in fig. D3. Figure 4.34a shows such a slice obtained with 7 μm focal spot size and a distance between isocenter and detector of 572 mm (phase contrast imaging). Figure 4.34b shows the reconstructed slice obtained with a larger focal spot size (50 μm) and a distance between isocenter and detector of 129 mm (attenuation based imaging). The air kerma at isocenter is 6.3 mGy in both cases. Three masses of 1 mm, 2 mm and 6 mm are visible as well as the microcalcification cluster. This test aims at showing the differences in details visibility between the conventional attenuation based imaging to that obtained in phase-contrast. It is worth of noting that the use of larger focal spot in attenuation based CT could reduce the system spatial resolution and so microcalcification visibility. However in figs. 4.34 and 3.35, the use of a voxel size (200×200×200 μm^3) larger than the system spatial resolution limits the effect due to the difference in spatial resolution.

Figure 4.35 shows profile across a microcalcification in the two cases. The difference between the microcalcification signal peak and the background signal is 2.6 times higher in the former case. Figure 4.36 shows the NPS curves, evaluated both in phase contrast imaging and in attenuation based imaging, for a voxel size of 200×200×200 μm^3. The noise level is significantly higher in the first case (see also fig. 4.34). The difference in the noise level can be related to the lower photon fluence

at the detector plane for the phase contrast CT caused by the larger distance between isocenter and detector than in attenuation based CT. Indeed, once the distance between the source and the isocenter is fixed, the X-ray cone-beam intensity reduces as the inverse of the square of the image magnification. Moreover, even though it presents a slight influence, the larger is the distance between the imaged object and the detector, the larger is the attenuation introduced by the interposed air so further reducing the photon fluence at the detector plane. Such a high noise level makes it difficult to detect a 1-mm mass for voxel sizes smaller than $200 \times 200 \times 200$ μm^3. In phase contrast imaging, the microcalcification cluster and the 6-mm mass are visible both for a voxel size of $100 \times 100 \times 100$ μm^3 (figs. 4.37a and 4.37c, respectively) and for a voxel size of $200 \times 200 \times 200$ μm^3 (figs. 4.37b and 4.37d, respectively).
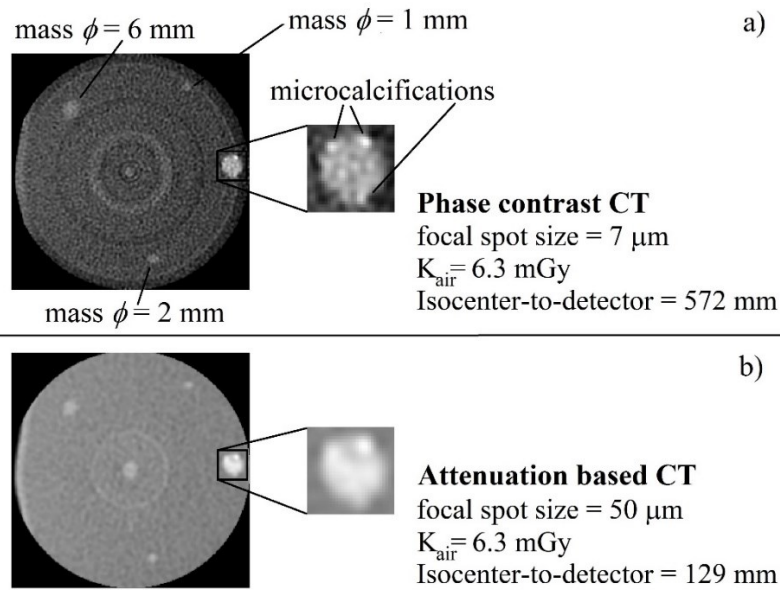
Fig. 4.34. *A coronal slice of a CIRS phantom mod. 1272-00-00. Projections = 300; total exposure time 141 s; total air kerma at isocenter 6.30 mGy; source to isocenter distance 612 mm; voxel size (200 μm)³. a) Phase contrast CT obtained with 7 μm focal spot size (M = 1.93). b) Attenuation based CT obtained with 50 μm focal spot size (M = 1.21). Better visibility of calcifications is shown by phase contrast CT.*
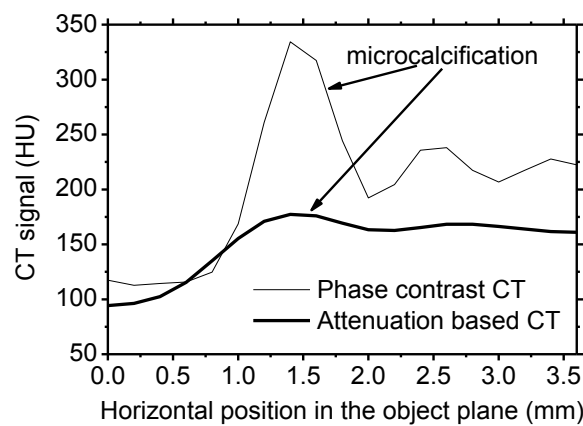
Fig. 4.35. *Profiles across a microcalcification in phase contrast CT (7 μm focal spot size; M = 1.93) and in attenuation based CT (50 μm focal spot size; M = 1.21). Projections = 300; total exposure time 141 s; total air kerma at isocenter 6.30 mGy; source to isocenter distance 612 mm; voxel size (200 μm)³.*
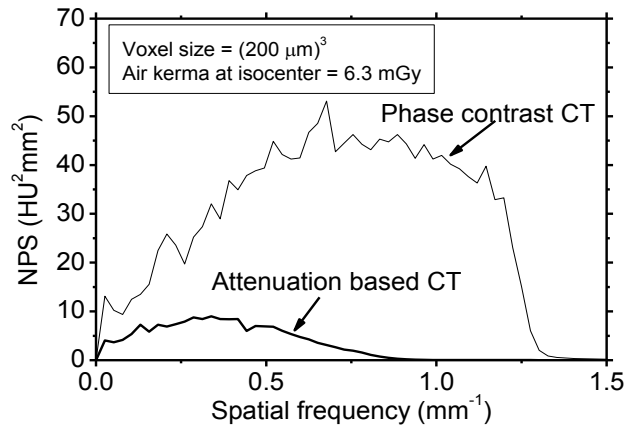
Fig. 4.36. *1D NPS curves in phase-contrast CT and attenuation based CT for a voxel size of (200 μm)³ and an air kerma at isocenter of 6.3 mGy.*
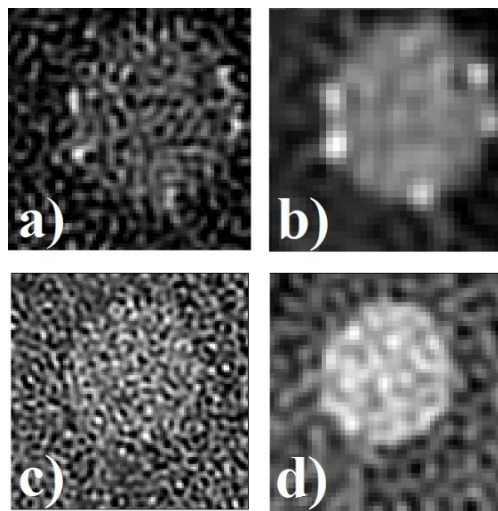
Fig. 4.37. *Details of the reconstructed CT slices of the anthropomorphic breast phantom, showing a microcalcification cluster (a-b) and a mass with a diameter of 6 mm (c-d) from slices with a isotropic reconstructed voxel of (100 μm)³ (a,c) and (200 μm)³ (b,d). Total air kerma at isocenter 6.3 mGy; 300 projections; M = 1.93; 50 kV, 0.2 mA.*

5. Conclusions

5.1. Discussions of the results of this work

5.1.1. Dosimetry in 2D and 3D X-ray breast imaging

A Monte Carlo code has been developed (sects. 2 and 3.1) in order to estimate the dose in X-ray breast imaging, in particular in breast CT, both in the case of full breast irradiation and in partial irradiation.

First of all the adopted models were revisited in mammographic geometry, with particular attention to the skin thickness, the influence of the compression paddles and the bremmstrahlung radiation produced by secondary electrons in the breast tissue. The availability of breast anatomy determinations in patients via BCT scans showed that the detected skin layer had an average thickness as low as 1.45 mm (range 0.8 − 2.5 mm), instead 4−5 mm as commonly assumed in MGD calculations on the basis of histology. By extending the results of Huang *et al* (2008), we showed the influence of the skin model on the DgN values. Adopting a skin thickness of 4 mm causes an underestimation up to 32% in DgN(E) with respect to adopting a skin thickness of 1.45 mm, for mammographic spectra routinely adopted in breast imaging. The presence of a subcutaneous fat tissue layer has also been investigated: the inclusion of a 2-mm thick adipose layer between the skin layer (1.45-mm thick) and the part of the breast containing the glandular tissue, causes a DgN_p underestimation in the range 2−12%. The relevance of this finding highlights the interest on additional measurement on density and composition of breast tissues, which are scarce (Dance and Sechopoulos 2016). The presence of compression paddles presents a maximum influence in the order of 2% on the calculation of DgN(E)*,* in the explored energy range 8−80 keV. In order to compute the polyenergetic DgN coefficients by weighting the monoenrgetic ones on the spectrum shape (eq. 2.7), this last should be computed with monoenergetic beams impinging on the breast surface (and so on the air kerma scoring surface). However, the inclusion of the top compression paddle could produce scattered photons with energy different from the primary beam. For this reason, the top compression paddle should not be simulated but opportunely taken into account in the spectra calculation. The inclusion of the top compression paddle in the MC calculation of DgN(E) causes a DgN_p underestimation of less than 1.5%. The inclusion of bremsstrahlung processes in the MC simulations have a weak influence (up to 1.1% at 48 keV) on DgN(E) evaluation and its effect is negligible in the mammographic energy range (photon energies less than 40 keV). In order to validate the homogeneous breast model, we simulated a heterogeneous breast model where the breast tissue is a heterogeneous mixture of gland and fat. In the range 15−80 keV, DgN(E) coefficients evaluated with a homogeneous breast model differ by 1−3% from those evaluated with a heterogeneous breast model. A MC model which includes a breast with 1.45 mm skin thickness, bremsstrahlung processes as well as X-ray spectra tuned on the basis of the added filter thickness, shows a difference up to

19% in DgN_p with respect to recent data for DgN_p in mammography (Nosratieh *et al* 2015). In conclusion, the estimate dose strongly depend on the adopted model, in particular on the modeled skin thickness and material. The different models studied led to a difference in dose estimate up to 32% (evaluated between a breast model with a 1.45 mm skin thickness and a breast with 4 mm skin thickness). A particular interest should be adopted in air kerma computation, both in taking properly into account the scattered radiation from the compression paddle and in simulating the real air kerma measurement procedures. A comparison between standard models and specific breast phantoms is necessary and planned for future work, in order to furnish additional information to the work in literature (Sechopoulos *et al* 2012 and Hernandez *et al* 2015) and to furnish a complete model insight for future dosimetry protocols (e.g. AAPM TG–282, website accessed online on 04/04/2017: https://www.aapm.org/org/structure/?committee_code=TG282).

The effect of partial irradiation was then investigated in 2D partial breast irradiation. This work has characterized how normalized dose coefficients, DgN, behave under various different imaging conditions and breast models during spot compression mammography. For this scope, we introduced the MGD_V, the mean glandular dose evaluated exclusively into the directly irradiated portion of the breast. Due to the partial breast irradiation, the characteristics of DgN change somewhat compared to full-field imaging. For example, in this modality, DgN does vary considerably with breast size, a factor usually considered not to have an effect on DgN in full field mammography. We also showed that, by employing a homogeneous breast model as used in full field mammography, DgN does not vary considerably, as long as the directly irradiated portion does not extend beyond the edges of the breast. More surprisingly perhaps, the relation between the thicknesses of the compressed and uncompressed portions of the breast does not affect DgN. On the other hand, due to the low dose in the non-directly irradiated portion of the breast (about 5% of the absorbed energy is in the not directly irradiated tissue), the DgN_V presented a weaker dependence on the breast model and irradiation geometry than that presented by the DgN. This characterization will be useful in the development of a new breast dosimetry model for mammography and breast tomosynthesis imaging, a task currently being undertaken by a joint task group of the American Association of Physicists in Medicine (AAPM – TG282) and the European Federation of Organizations for Medical Physics (EFOMP). Considering the large variation in *local* dose deposition throughout the breast due to the use of relatively low X-ray energies (Thacker and Glick 2004, Sechopoulos *et al* 2010), it could be debated if averaging the glandular dose over the entire breast is really the most appropriate risk-related metric for full field mammography. In a related fashion, the results for DgN_V show that this might also be a valid discussion point for imaging that involves partial field irradiation of the breast. The use of the average dose to the whole breast implies that during acquisition of a spot compression image, the radio-induced risk is lowered if the breast is larger even when the extra tissue is located well beyond the field of view. Although the appropriateness of the current risk model is beyond the scope of this work, the insight gained here on DgN_V might be useful in the future if the local variations in dose

during breast imaging become part of the accepted dosimetry model. The metric DgN_M, proposed to avoid the need for new MC simulations and data tables, was found to underestimate the dose by up to 14% for monoenergetic photons at 45 keV, although such underestimation reduces with photon energy and is 6.7% for a W/Rh spectrum at 28 kVp. Therefore, until new results are available, the use of DgN_M can provide an adequate estimate of the mean glandular dose.

Once the models were reviewed, both in full-field digital mammography and in spot compression mammography, the results were extended to the case of 3D CT dedicated to the breast. Due to the greater energies adopted in such a breast modality than in mammography, the skin thickness resulted in a lower influence on the conversion factor and we adopted the skin thickness of 1.45 mm. In the case of full-field BCT, the DgN_{CT} coefficients were calculated, both for monoenergetic beam, for the spectra adopted in clinical practice. Moreover, the adopted model was validated vs. patient specific phantoms. For a homogeneous standard breast model the estimated dose to the breast resulted, on average, only 4.5% higher.

Finally, the conversion factors for the SYRMA-CT setup were computed. In a future SR-BCT exam, the limited vertical dimension of the SR beam and the necessity to translate and rotate the patient pose practical limits to the *in-vivo* exam of the breast, also affecting the duration of the exam and the discomfort for the patient. In order to overcome these limitations the SYRMA-CT collaboration plans to image only a fraction of the pendant breast, by investigating only regions where a suspicious lesion has been previously located. As noticed for the case of spot compression mammography, the use of the MGD in the case of the irradiation of a limited fraction of the breast could lead to an underestimation of the delivered dose. The value of this underestimation depends on the dimensions of the irradiated breast: specifically, it increases with the decrease of the irradiated volume up to 97% in the case of irradiation of a single slice of 3 mm height. On the basis of these results, in addition to the MGD and the MGD_V, a new parameter was introduced: the MGD_t. It is defined as the ratio between the deposited energy in the glandular mass of the whole breast and the glandular mass in the irradiated volume. These quantities (MGD, MGD_V and MGD_t) were evaluated as a function of the dimension of the scanned breast and of the beam energy, for geometrical conditions of interest for the SYRMA-CT SR-BCT study. It can be noted that the MGD_t is almost independent of the height of the irradiated volume and it can be a valid alternative to MGD for partial breast irradiation in BCT, due also to its similarity to the CTDI metric in whole body CT. However, the most appropriate dose metric should be selected in order to relate to the risk. In addition, the large dose non-uniformity in partial breast irradiation, which are not usually taken into account in the dose risk evaluation in medical imaging (Samei *et al* 2012), should be opportunely considered in the risk estimation. This last is the aim of an ongoing work (Sarno *et al* 2016d)

5.1.2. Image quality in phase-contrast breast imaging

The combination of several features of the SYRMA-CT scanner (fine pixel pitch, high resolution X-ray detector, high-spatial coherence of the monochromatic X-ray beam and large distance between scanned object and detector plane) permitted to detect phase-contrast effects produced by X-ray beam refraction in free-space propagation based imaging. No phase-contrast effects were present in CT slices of a breast specimen in a previous study at ELETTRA with the same geometry: this was attributed to the larger pixel pitch (200 μm) of the detector used in that previous study, which hindered the visibility of the signal overshoot and undershoot at object edges (Pani *et al* 2004). In this work, with a 60-μm pitch detector, reconstruction voxel size of $(60 \ \mu m)^3$ and $(120 \ \mu m)^3$ preserved the phase-contrast information. In previous investigations at ELETTRA with monochromatic SR film-screen mammography, propagation-based phase-contrast imaging showed higher contrast detail visibility than conventional mammography at a comparable or lower dose (Castelli *et al* 2007).

In this new SR setup at ELETTRA, the fine pitch featured by the single-photon counting detector determined a spatial resolution as high as 6.7 mm^{-1} at 10% MTF, in slices with voxel size of $(60 \ \mu m)^3$ reconstructed via FBP algorithm and without phase retrieval. This system spatial resolution is significantly higher than that of polychromatic cone-beam BCT scanners (Sarno *et al* 2015), and compares well with the 5.6 mm^{-1} limiting frequency of the helical BCT scanner developed at University of Erlangen equipped with a high-resolution single-photon counting detector (Steiding *et al* 2014). The spatial resolution limit of the SYRMA-CT setup reduced to 2.5 mm^{-1} when a Paganin filter was applied on the projections, in the application of the phase retrieval algorithm.

The edge enhancement effects seen in phase-contrast images of test objects increased the MTF curve to values higher than its zero-frequency value; Honda *et al* (2006), in propagation-based phase-contrast mammography, reported a similar effect in their images, showing an improvement of the edge sharpness of the object in projected images due to the phase effects.

The Paganin filter reduced drastically the image noise: the NNPS curves for images without phase retrieval had a maximum value several times greater than those in phase retrieval images. The voxel size had weak influence on noise in images obtained with phase retrieval. The NNPS curves in the images without phase retrieval reached their maximum value at about 3 mm^{-1}; on the other hand, the curves in the images with phase retrieval had their maximum at 1 mm^{-1}, balancing in part the reduction of the system spatial resolution due to the Paganin filter. With the phase retrieval algorithm here adopted, the filter smoothing produced a FWHM size of the microcalcifications slightly higher than the actual size, but reduced the background signal fluctuation and preserved microcalcification visibility. In the phantom study, $CaCO_3$ microcalcifications with a diameter down to 130 μm were visibile.

In this work, the CNR in the images without phase retrieval was several times lower than that obtained with phase retrieval. The soft masses embodied in the mammographic test object were detected with high CNR when the phase retrieval process was applied to the projections. Correspondingly, for a CT slice thickness of 360 μm and a slice pixel of $(60 \text{ μm})^2$, raw phase-contrast CT imaging without phase retrieval produced a significantly lower masses visibility (CNR about six times lower).

A global figure of merit, which takes into account spatial resolution and noise in CT slices, was evaluated. The analysis of this Q-index showed that in the trade-off between spatial resolution and noise in propagation-based phase-contrast imaging, the phase retrieval processing – with voxel size of $(60 \text{ μm})^3$ – produced higher imaging performance than raw (i.e. without phase retrieval) phase-contrast imaging. The voxel size did not change significantly the Q-index in the images without phase retrieval, where reduction in the image noise balanced the reduction in the system spatial resolution. On the other hand, increasing the voxel size from $(60 \text{ μm})^3$ to $(120 \text{ μm})^3$ did not significantly reduce the noise in phase retrieval images but a reduction of the limiting spatial resolution from 2.5 mm^{-1} to 1.7 mm^{-1} was observed, with the global figure of merit reducing by as much as 2.6 times.

In the SYRMA-CT setup, in order to image a whole breast with a monochromatic thin laminar beam, consecutive slices should be acquired (sequential CT). After the first 180 deg scan, the patient support is translated vertically by a step corresponding to the beam height (about 3 mm) and a successive rotational (circular orbit) scan can be performed. The image dose to the "glandular tissue" of the breast phantom used in this work (CIRS test object BR50/50 mod. 014AD) was less than 4.2 mGy (Mettivier *et al* 2015). The MGD to the breast in the case of whole breast SR-BCT irradiation (breast diameter = 12 cm, breast height = 9 cm, glandular fraction = 50%) with an air kerma at isocenter of 10.4 mGy, was estimated at 7.3 mGy (Mettivier *et al* 2015). Such a glandular dose is higher than, but comparable to, the one used in a two-view mammography exam. For a 12-cm diameter, uncompressed 50/50 breast – which corresponds to a 3.2-cm thick compressed breast according to the determinations of Boone *et al* (2005) – the MGD for two-view mammography is approximately 2.5 mGy (data from fig. 4 in Boone *et al* (2005)). An MGD of 7.3 mGy is comparable to that used for diagnostic (non screening) mammography exams, where the MGD could be between 6 and 36 mGy (mean = 16.9 mGy, st.dev. = 6.9 mGy) (O'Connell and O'Connor 2012). An estimated MGD of 7.3 mGy is also lower than that evaluated for the Koning commercial BCT scanner – recently approved by FDA in USA for diagnostic imaging and having the CE mark in the European Union since 2012 – which released to the breast a mean glandular dose ranging between 5.6 mGy and 17.5 mGy (Sechopoulos *et al* 2010).

The results in this work showed that, by applying SART iterative reconstruction to a reduced number of projections (300 instead of 1200, producing a decrease of 75% in the exam dose), images

can be obtained which present the same spatial resolution and a CNR decrease by 30% using SART instead of FBP reconstruction. Moreover, the SART algorithm coupled with a ring artefacts removal algorithm is effective in reducing artefacts caused by detector block junction and pixel instability.

In this thesis, a prototype of compact micro-CT scanner dedicated to the breast has been presented, featuring a small detector pitch (50 μm), a micro focal spot (7 μm) and the capability of producing phase effects in a moderate degree. The scanner presented here − showing higher performance than the previous setup (Russo *et al* 2010) − is a laboratory prototype, and both the small detector sensitive area and the low detector frame rate represent an issue for clinical work: we plan an upgrade to a high-resolution (75-μm pitch), large area, high frame rate CMOS detector. The use of a microfocus X-ray tube imposes low tube currents: the time necessary to deliver 4 mGy MGD to a breast with a diameter of 14 cm at chest wall and a glandular fraction of 50% is 245 s at 50 kV and it decreases as the tube voltage increases. Hence, breast scanning in breath-hold modality is not feasible; motion artefacts caused by chest wall movement and movements of the freely hanging breast will be limited via a patient-specific breast holder capable of immobilizing the pendant breast (Fig. D5 the supplementary material, sect. 9.4.). The scanner presents a high spatial resolution, which depends on the spatial direction, on the distance from the isocenter, and on the X-ray cone angle. For a voxel size of (50 μm)^3 and an image magnification of 1.21, the $MTF_{0.1}$ reaches 6.2 mm^{-1} in the vertical direction, 3.8 mm^{-1} in the radial direction and 3 mm^{-1} in the tangential direction. Increasing the magnification from 1.23 to 1.91 reduces the MTF 0.1 both in the vertical (from 6.2 mm^{-1} to 4.9 mm^{-1}) and in the radial directions (from 3.8 mm^{-1} to 3.3 mm^{-1}); substantial differences were not observed in the tangential direction. The system spatial resolution measured in this work is higher than that of clinical BCT systems developed by other groups (Liu *et al* 2012), except for the spiral BCT developed at U Erlangen (which adopts a direct-conversion photon-counting detector with pixel pitch of 100 μm and an active area of 51.2 ×25.6 mm^2 (Kuttig *et al* 2015)) featuring an $MTF_{0.1}$ as high as 5.3 mm^{-1} (Kalender *et al* 2016). In spite of a short distance (about 572 mm) between object and detector, the lateral spatial coherence length of the X-ray beam (3.5 μm) permitted to reveal − to some degree − phase effects on a PMMA phantom edge, both in planar and in 3D images. These effects were not visible in images acquired with a shorter distance between the isocenter and the detector. An anthropomorphic phantom test showed the capability of the BμCT in terms of improved microcalcifications visibility and soft lesions visibility with a low radiation dose. Mass lesions with a diameter of 1 mm, 2 mm or 6 mm were detected together with a microcalcification cluster. By fixing the dose to the breast, phase contrast imaging determines less photon fluence on the detector than in contact imaging. Despite the higher noise level, the microcalcification cluster was better imaged with a focal spot size of 7 μm and large magnification rather than with a focal spot size of 50 μm and at ×1.21 magnification.

5.2. Concluding remarks

In summary, the results reported in this PhD thesis lead to the following information in the field of the X-ray breast dosimetry and imaging, with a particular focus on the 3D phase-contrast based imaging of the breast.

1) Monte Carlo simulations showed that breast models present a significant influence on the estimated glandular dose in mammography. In particular, a breast model which includes a 1.45 mm thick skin layer instead of the usually adopted 4−5 mm leads to an MGD estimation up to 19% higher. This maximum difference reduces to 12% if a 2-mm thick adipose layer is added between the skin and the radiosensitive tissues of the breast. On the other hand, in CT dedicated to the breast, where higher photon energies are employed, the skin thickness does not play such a fundamental role in the dose estimation.

2) The geometry of the partial breast irradiation needs a specific dose evaluation. To this purpose, we analyzed the case of partial irradiation in 2D spot compression mammography and the case of the uncompressed breast adopted in SYRMA-CT. In addition to the conventional MGD definition (i.e. the energy absorbed in the whole glandular tissue contained in the breast divided by total glandular mass), two other dosimetric parameters have been introduced: MGD_V and MGD_T. The first is the average dose absorbed exclusively in the directly irradiated breast, and the second is the energy absorbed in the whole breast glandular tissue divided by the directly irradiated glandular mass. In full-field mammography, the DgN coefficients (i.e. the measured air kerma to MGD conversion factors) are supposed to be independent of the compressed breast radius, but dependent on the breast thickness and glandularity. On the other hand, in the case of partial irradiation, the breast dimension plays a fundamental role. For the same irradiated breast area, the estimated MGD does considerably change with the breast dimension, differently to what happens for the MGD_V and MGD_T.

3) In this work, the DgN_{CT} (i.e. DgN for the BCT imaging) dose coefficients were computed both for cone-beam full irradiation and for partial parallel beam irradiation. The computation has been done for various breast sizes and glandular fractions, as well as for various photon energies (monoenergetic and polyenergetic beams), and for various breast area coverage in the case of partial irradiation. In the latter case, the conversion coefficients from the measured air kerma to MGD_V and MGD_t have been calculated.

4) The image quality for the SYRMA-CT setup has been assessed both without and with a phase retrieval algorithm. The system spatial resolution, evaluated as the frequency which reduces the MTF curve at 10% of the 0-frequency value, is up to 6.7 mm^{-1}, higher than the compact BCT scanner presented in literature. Such a spatial resolution reduces to 2.5 mm^{-1} with the phase retrieval algorithm. This value is higher than the one obtained with a commercial BCT scanner. On the other

hand, the retrieval algorithm reduces the noise level by one order of magnitude and a global index quality outlines that it improves the image quality, at least for a voxel size of $60\times60\times60$ μm^3. Both soft masses lesions with a diameter down to 0.9 mm and microcalcifications with a diameter down to 130 μm were well depicted in a breast phantom irradiated with a dose level as low as that adopted in diagnostic mammography, both with and without the phase retrieval algorithm.

5) We tested the iterative CT reconstruction (SART) developed by the University of Sassari group within the SYRMA-CT collaboration. This algorithm produced images with detailed contrast-to-noise ratio (CNR) and spatial resolution higher than those presented by the images reconstructed via the FBP reconstruction. It permits to spare up to 25% of dose to the breast, without altering the image quality, a typical features of iterative reconstruction algorithms. Similar results were not replicable for the FBP reconstruction. The ring removal algorithm, coupled with the SART reconstruction, reduced drastically the ring artefacts. These findings, together with those at the above points 3 and 4, will be considered in the clinical protocols for the *in vivo studies* scheduled for the near future in an upgrade of the SYRMA-CT project at the SYRMEP beamline.

6) A BCT scanner which relies on a high resolution flat panel detector and a micro-focus source (focal spot dimension = 7 μm) has been developed. The scanner employs a relatively high-coherent source, with a lateral coherence length of 3.5 μm (the SYRMA-CT source presents a lateral coherence length of 5 μm). The system spatial resolution is up to 3.8 mm^{-1} in the radial direction and up to 6.2 mm^{-1} in the vertical direction. This value is higher than that presented by the scintillator-based BCT scanners and comparable with the spatial resolution presented by the helical BCT scanner developed at Univ. of Erlangen which relies on a photon-counting detector. The scan time would not permit a scan in breath-hold modality, as possible with larger focus sources, hence a specific tool with the purpose of immobilizing the breast during the projections acquisitions has been developed. The scan time will be a few minutes, for delivering a dose equal to two-view MGD in mammography. A breast phantom study showed that both microcalcification clusters and soft lesions are visible with dose comparable to that used in two-view screening mammography. With a slight reduction of the spatial resolution due to the increased magnification ($\times1.93$) the developed scanner showed that phase-contrast based imaging can be performed with such a compact scanner. The phase-contrast effects permitted an edge enhancement up to 20% and the finer details in the CT slices resulted better depicted than in the absorption based BCT. We plan to update the system with a larger X-ray detector.

6. Acknowledgments

7. References

AAPM 2010 Report 11 Comprehensive Methodology for the Evaluation of Radiation Dose in X-Ray Computed Tomography

AAPM 2015 Sechopoulos I et al Report no. 195 Monte Carlo Reference Data Sets for Imaging Research. The Report of AAPM Task Group 195

Auweter S D et al 2014 X-ray phase-contrast imaging of the breast—advances towards clinical implementation. Br. J. Radiol. **87** 1–8

BCSC 2009a – web site: http://www.bcsc-research.org/statistics/benchmarks/screening/2009/tableSensSpec.html, data upload on 09-23-2013 (accessed on 11.23.2016)

BCSC 2009b Website: http://breastscreening.cancer.gov/statistics/performance/screening/2009/perf_age.html. (accessed on 07.03.2015).

Bellazzini R et al 2013 Chromatic X-ray imaging with a fine pitch CdTe sensor coupled to a large area photon counting pixel ASIC *J Instrum* **8** C02028

Boone J M et al 1997 Molybdenum, rhodium, and tungsten anode spectral models using interpolating polynomials with application to mammography *Med. Phys.* **24** 1863–1874

Boone J M and Seibert J A 1997 An accurate method for computer-generating tungsten anode x-ray spectra from 30 to 140 kV *Med. Phys.* **24** 1661−70

Boone J M 1999 Glandular Breast Dose for Monoenergetic and High-Energy X-ray Beams: Monte Carlo Assessment 1 *Radiology* **213** 23–37

Boone J M and Chavez A E 1996 Comparison of x-ray cross sections for diagnostic and therapeutic medical physics. *Med. Phys.* **23** 1997–2006

Boone J M et al 2001a Dedicated Breast CT: Radiation Dose and Image Quality Evaluation. Radiology **221** 657–667

Boone J M 2001b Determination of the presampled MTF in computed tomography Med. Phys. **28** 356–360

Boone J M 2002 Normalized glandular dose (DgN) coefficients for arbitrary x-ray spectra in mammography: Computer-fit values of Monte Carlo derived data *Med. Phys.* **29** 869–875

Boone J M et al 2004 A comprehensive analysis of DgN CT coefficients for pendant-geometry cone-beam breast computed tomography *Med. Phys.* **31** 226–235

Boone JM et al 2005 Technique factors and their relationship to radiation dose in pendant geometry breast CT *Med. Phys.* **32** 3767–3776

Boone J M et al 2010 An X-ray computed tomography/positron emission tomography system designed specifically for breast imaging *Technol. Cancer Res. T* **9** 29–44

Bravin A et al 2013 X-ray phase-contrast imaging: from pre-clinical applications towards clinics *Phys. Med. Biol.* **58** R1–R35

Cai W and Ning R 2009 Dose efficiency consideration for volume-of-interest breast imaging using x-ray differential phase-contrast CT *Proc SPIE 7258, Med. Imag. 2009: Physics of Medical Imaging* 72584D

Camerani M C et al E 2004 X-ray *fluorescence* tomography of individual municipal solid waste and biomass fly ash particles *Anal. Chem.* **76** 1568-95

Castelli E et al 2007 Clinical mammography at the SYRMEP beam line Nucl. Instrum. Meth. A **572** 237–240

Castelli E et al 2011 Mammography with synchrotron radiation: first clinical experience with phase-detection technique *Radiology* **259** 684–94

Cauzid J et al 2007 3D imaging of vapour and liquid inclusions from the Mole Granite, Australia, using helical fluorescence tomography *Spectrochim. Acta B* **62** 799–806

Chen B and Ning R 2001 Cone-beam volume CT mammographic imaging: feasibility study. *Proc SPIE 2001* **4320** 655–664

CSIRO – website: https://ts-imaging.net/Services/Simple/ICUtilXdata.aspx. [accessed on 15.10.2015].

Dance D R 1990. Monte-Carlo calculation of conversion factors for the estimation of mean glandular breast dose *Phys. Med. Biol.* **35** 1211–1219

Dance D R et al 2000 Additional factors for the estimation of mean glandular breast dose using UK mammography dosimetry protocol *Phys. Med. Biol.* **45** 3225–3240

Dance D R et al 2009 Futher factors for the estimation of mean glandular breast dose using United Kingdom, European and IAEA breast dosimetry protocols *Phys. Med. Biol.* **54** 4361–4372

Dance D R and Young K C 2014 Estimation of mean glandular dose for contrast enhanced digital mammography: factors for use with the UK, European and IAEA breast dosimetry protocols *Phys. Med. Biol.* **59** 2127–2137

Dance D R and Sechopoulos I 2016 Dosimetry in x-ray-based breast imaging *Phys. Med. Biol.* **61** R271-R304

David C et al 2007 Hard X-ray phase imaging and tomography using a grating interferometer *Spectr Acta B* **62** 626–630

Delogu P et al 2016 Characterization of Pixirad-1 photon counting detector for X-ray imaging *JINST* **11** P01015

Diemoz P et al 2016 A method for high-energy, low-dose mammography using edge illumination x-ray phase-contrast imaging *Phys. Med. Biol.* **61** 8750–8761

Donnelly E F et al 2003 Quantification of the effect of system and object parameters on edge enhancement in phase-contrast radiography *Med. Phys.* **30** 2888–2896

Dreossi D et al 2008 The mammography project at the SYRMEP beamline *Eur J Radiol* **68** S58–S62

European Commission 2006 4th edition of the European Guidelines for Quality Assurance in Breast Cancer Screening and Diagnosis

Fedon C et al 2015 GEANT4 for breast dosimetry: parameters optimization study *Phys. Med. Biol.* **60** N311−N323

Fedon C 2016 Simulations and experimental assessment of dosimetric evaluations for breast imaging studies with Synchrotron Radiation *PhD thesis University of Trieste (Italy)*

Feldkamp L A et al 1984 Practical cone-beam algorithm *J. Opt. Soc. Amer. A* **6** 612−619

Fiedler S et al 2004 Imaging lobular breast carcinoma: comparison of synchrotron radiation DEI-CT technique with clinical CT, mammography and histology *Phys. Med. Biol.* **49** 175–188

Gazi P et al 2013. Development and spatial resolution characterization of a dedicated pulsed X-ray, cone-beam breast CT system. *Proc SPIE* **8668** 86681D–86681D-7

Gazi P et al 2015 Evolution of spatial resolution in breast CT at UC Davis. Med. Phys. **42** 1973–1981

Globocan 2012 – web site: http://globocan.iarc.fr/Pages/fact_sheets_population.aspx (accessed on 11-22-2016)

Golosio B et al 2004 Algorithmic techniques for quantitative Compton tomography *Nucl. Instrum. Methids B* **213** 108-11

Gureyev T E *et al.* 2014 Investigation of Imaging Quality of Synchrotron-Based Phase-Contrast Mammographic Tomography *J. Phys. D: Appl. Phys.* **47** 365401

Hammerstein R G et al 1979 Absorbed radiation dose in mammography *Radiology* **130** 485–491

Hernandez A M and Boone J M 2014 Tungsten anode spectral model using interpolating cubic splines: Unfiltered x-ray spectra from 20 kV to 640 kV *Med. Phys.* **41** 042101-1–15

Hernandez A M et al 2015 Breast dose in mammography is about 30% lower when realistic heterogeneous glandular distributions are considered *Med. Phys.* **42** 6337–6348

Honda C et al 2006 Image qualities of phase-contrast mammography. *Digital Mammography 8th International Workshop, IWDM 2006 Manchester, UK, June 18-21, 2006 Proceedings* **4046** 281–288

Honda C and Ohara H 2008 Advantages of magnification in digital phase-contrast mammography using a practical X-ray tube *Eur. J. Rad.* **68** S69–S72

Huang S-Y et al 2008 The effect of skin thickness determined using breast CT on mammographic dosimetry *Med. Phys.* **35** 1199–1206

Hubbell JH and Seltzer SM 2004 Tables of X-Ray Mass Attenuation Coefficients and Mass EnergyAbsorption Coefficients from 1 keV to 20 MeV for Elements Z = 1 to 92 and 48 Additional Substances of Dosimetric Interest *from http://www.nist.gov/pml/data/xraycoef/index.cfm* (accessed on 05-23-2016)

ICRU (International Commission on Radiation Units and Measurements) 1989 Report 44, Tissue Substitutes in Radiation Dosimetry and Measurement (Bethesda, MD)

IPEM (Institute of Physics and Engineering in Medicine) 2005 The commissioning and routine testing of mammographic X-ray systems. *IPEM Report 89* (York, United Kingdom: IPEM)

Kak A C and Slaney M 1988 Principles of Computerized Tomographic Imaging (New York: IEEE)

Kalender W A 2005 Computed tomography. 2nd rev. *Ed. Publicis Corporate Publishing*

Kalender W A 2010. Concepts for high-resolution CT of the breast. *Digital mammography* **6136** 421–427

Kalender W A et al 2012 High-resolution spiral CT of the breast at very low dose: concept and feasibility considerations *Eur. Radiol.* **22** 1–8

Kalender W A 2014 Dose in x-ray computed tomography *Phys. Med. Biol.* **59** R129–R150

Kalender W A et al 2016 Technical feasibility proof for high-resolution low-dose photon-counting CT of the breast *Eur. Radiol.* 1–6

Keyriläinen J et al 2005 Visualisation of calcifications and thin collagen strands in human breast tumour specimens by the diffraction-enhanced imaging technique: a comparison with conventional mammography and histology *Eur. J. Radiol.* **53** 226–237

Keyriläinen J *et al* 2008 Toward high-contrast breast CT at low radiation dose *Radiology* **249** 321–327

Kim H K et al 2005. Use of a flat-panel detector for microtomography: A feasibility study for small-animal imaging *IEEE Trans. Nucl. Sci.* **52** 193–198

Koutalonis M et al 2006 Monte Carlo generated conversion factors for the estimation of average glandular dose in contact and magnification mammography *Phys. Med. Biol.* **51** 5539–5548

Koukou V et al 2017 Dual energy subtraction method for breast calcification imaging *Nucl. Instrum. Meth. A* **848** 31–38

Kuttig J D et al 2015 Comparative investigation of the detective quantum efficiency of direct and indirect conversion detector technologies in dedicated breast CT *Phys. Medica* **31** 406–413

Kwan A L C et al 2007 Evaluation of the spatial resolution characteristics of a cone-beam breast CT scanner *Med. Phys.* **34** 275–281

Lång K et al 2016 Performance of one-view breast tomosynthesis as a stand-alone breast cancer screening modality: results from the Malmö Breast Tomosynthesis Screening Trial, a population-based study *Eur. Rad. 26* 184–190

Lindfors K K et al 2008 Dedicated breast CT: initial clinical experience *Radiology* **246** 725–733

Liu B et al 1995 Normalized average glandular dose in magnification mammography *Radiology* **197** 27–32

Liu J et al 2012 Enhancement of breast calcification visualization and detection using a modified PG method in Cone Beam Breast CT *J. X-ray Sci. Technol.* **20** 107–120

Longo R et al 2014 Clinical study in phase-contrast mammography: image-quality analysis *Phil. Trans. R. Soc. A* **372** 1–8

Longo R et al 2016 Towards breast tomography with synchrotron radiation at Elettra: first images *Phys. Med. Biol.* **61** 1634–1649

Lopez F C et al 2014 Comparator threshold settings and the effective pixel width of the PICASSO detector *JINST* **9-C05056** 1–8

Mettivier G and Russo P 2011a Measurement of the MTF of a cone-beam breast computed tomography laboratory scanner *IEEE Trans Nucl Sci* **58** 703–713

Mettivier G et al 2011b Dedicated scanner for laboratory investigations on cone-beam CT/SPECT imaging of the breast *Nucl. Instrum. Meth.* A **629** 350–356

Mettivier G et al 2012 Cone-beam breast computed tomography with a displaced flat panel detector array *Med Phys* **39** 2805–2819

Mettivier G et al 2015 Glandular dose in synchrotron radiation breast computed tomography *Phys. Med. Biol.* **61** 569–587

Mittone A et al 2014 Radiation dose in breast CT imaging with monochromatic x-rays: simulation study of the influence of energy, composition and thickness *Phys. Med. Biol.* **59** 2199-2206

Momose A et al 1996 Phase-contrast X-ray computed tomography for observing biological soft tissues *Nat. Med.* **2** 473–75

Monnin P et al 2007 A comparison of the performance of digital mammography systems *Med. Phys.* **34** 906–914

Nesterets Y I et al 2015 A feasibility study of X-ray phase-contrast mammographic tomography at the Imaging and Medical beamline of the Australian Synchrotron *J. Synchrotron Rad.* **22** 1509–1523

Nickoloff E L and Riley R 1985 A simplified approach for modulation transfer function determinations in computed tomography *Med. Phys.* **12** 437–442

Nosratieh A et al 2015 Mean glandular dose coefficients (DgN) for x-ray spectra used in contemporary breast imaging systems *Phys. Med. Biol.* **60** 7179–7190

Nowotny R 1998 XMuDat: Photon Attenuation Data on PC. IAEANDS-195 *International Atomic Energy Agency, Vienna(Austria)*

O'Connell A et al 2010 Cone-Beam CT for breast imaging: radiation dose, breast coverage, and image quality *Am. J. Roentgenol* **195** 496–509

O'Connell A and O'Connor DK 2012 Dedicated Cone-beam Breast Computed Tomography and Diagnostic Mammography: Comparison of Radiation Dose, Patient Comfort, And Qualitative Review of Imaging Findings in BI-RADS 4 and 5 Lesions *J. Cli. Imaging Sci.* **2** 1–8

Pacilè S et al 2015 Clinical application of low-dose phase contrast breast CT: methods for the optimization of the reconstruction workflow *Biomed. Opt. Express* **6** 3099–3112

Pani S et al 2004 Breast tomography with synchrotron radiation: preliminary results *Phys. Med. Biol.* **49** 1739-54

Paganin D et al 2002 Simultaneous phase and amplitude extraction from a single defocused image of a homogeneous object *J Microsc* 2002 **206** 33–40

Poludniowski G et al 2009 SpekCalc: a program to calculate photon spectra from tungsten anode x-ray tubes *Phys. Med. Biol.* **54** N433–N438

Quai E et al 2013 First application of computed radiology to mammography with synchrotron radiation *Radiol. Med.* **118** 89–100

Russo P et al 2010 X-ray cone-beam breast computed tomography: Phantom studies *IEEE Trans. Nucl. Sci* **57** 160–172.

Samei E et al 2012 The effect of dose heterogeneity on radiation risk in medical imaging *Radiat. Prot. Dosim.* **155** 42–58

Sarno A et al 2015 Dedicated breast computed tomography: basic aspects *Med. Phys.* **42** 2786–2804

Sarno A et al 2016a Imaging performance of phase-contrast breast computed tomography with synchrotron radiation and a CdTe photon-counting detector *Phys. Medica* **32** 681–690

Sarno A et al 2016b Monte Carlo evaluation of normalized glandular dose coefficients in mammography *In: Breast Imaging.* Proc. of 13th International Workshop, IWDM 2016, Malmö, Sweden, June 19-22, 2016, *Lecture Notes in Computer Science, Springer International Publishing, vol 9699,* 190–196

Sarno A et al 2016c A Monte Carlo study of monoenergetic and polyenergetic normalized glandular dose (DgN) coefficients in mammography *Phys. Med. Biol.* **62** 306–325

Sarno A et al 2016d Volume Distribution in Digital Breast Tomosynthesis: a Phantom Study *oral presentation at IEEE NSS/MIC congress, Strasburg (France) 29th October – 4th November 2016.*

Scherer K et al. 2016 Toward clinically compatible phase-contrast mammography *Springer International Publishing* 95–109

Sechopoulos I et al 2007 Computation of the glandular radiation dose in digital tomosynthesis of the breast *Med. Phys.* **34** 221–232

Sechopoulos I et al 2010 Dosimetric characterization of a dedicated breast computed tomography clinical prototype *Med. Phys.* **37** 4110–4120

Sechopoulos I et al J 2012 Characterization of the homogeneous tissue mixture approximation in breast imaging dosimetry *Med. Phys.* **39** 5050–5059

Sechopoulos I 2013a A review of breast tomosynthesis. Part I. The image acquisition process *Med. Phys.* **40** 014301

Sechopoulos I 2013b A review of breast tomosynthesis. Part II. Image reconstruction, processing and analysis, and advanced application *Med. Phys.* **40** 014302-17

Sechopoulos I et al 2015 Monte Carlo reference data sets for imaging research: Executive summary of the report of AAPM Research Committee Task Group 195 *Med. Phys.* **42** 5679–5691

Sempau J et al 2011 Monte Carlo simulation of electron beams from an accelerator head using PENELOPE *Phys. Med. Biol.* **46** 1163–1186

Shi L et al 2013 Technical Note: Skin thickness measurements using high-resolution flat-panel cone-beam dedicated breast CT *Med. Phys.* **40** 031913 1–6

Siegel R L et al 2016 Cancer statistics, 2016 *CA: a cancer journal for clinicians* **66** 7–30

Steiding C et al 2014 Quantitative assessment of the spatial dependence of non-stationary high-contrast spatial resolution, low-contrast detectability, and noise behavior in 3D imaging of the breast *20th European Congress of Radiology (ECR) 2014, March 6 – 10, Vienna, Austria*

Sutradhar A and Miller M J 2013 In vivo measurement of breast skin elasticity and breast skin thickness *Skin Res. & Technol.* 19 e191–199

Sztrókay A et al 2013 Assessment of grating-based X-ray phase-contrast CT for differentiation of invasive ductal carcinoma and ductal carcinoma in situ in an experimental ex vivo set-up *Eur. Radiol.* **23** 381–87

Takeda T et al 1998 Phase-contrast X-ray CT image of breast tumor *J. Synchrotron Radiat.* **5** 1133–35

Takeda T et al 2000 Human Carcinoma: Early Experience with Phase-Contrast X-ray CT with Synchrotron Radiation—Comparative Specimen Study with Optical Microscopy *Radiology* **214** 298–301

Tanaka T et al 2005 The First Trial of Phase Contrast Imaging for Digital Full-Field Mammography Using a Practical Molybdenum X-Ray Tube. *Invest. Radiol.* **40** 385–396

Thacker SC and Glick SJ 2004 Normalized glandular dose (DgN) coefficients for flat-panel CT breast imaging *Phys. Med. Biol.* **49** 5433–5444

Van Engen R E, Bouwman R, Dance D, Heid P, Lazzari B, Marshall N et al 2016 Protocol for the quality control of the physical and technical aspects of digital breast tomosynthesis system *Vers. 1.01 EUREF, European Guidelines for Quality Assurance in Breast Cancer Screening and Diagnosis*

Vedantham S et al 2013 Personalized estimates of radiation dose from dedicated breast CT in a diagnostic population and comparison with diagnostic mammography *Phys. Med. Biol.* **58** 7921–7936

Vincenzi A et al 2015 Energy characterization of Pixirad-1 photon counting detector system *JINST* **10** C04010

World Health Organization

Wilkinson L and Heggie C P 2001 Glandular breast dose: Potential errors *Radiology* **213**

Wu X et al 1991 Spectral dependence of glandular tissue dose in screen-film mammography *Radiology* **179** 143–148

Wu X et al 1994 Normalized average glandular dose in molybdenum target-rhodium filter and rhodium target-rhodium filter mammography *Radiology* **193** 83–89

Wu X and Liu H 2003 Clinical implementation of x-ray phase-contrast imaging: Theoretical foundations and design considerations *Med. Phys.* **30** 2169–2179

Wu X and Liu H 2007 Clarification of aspects in in-line phase-sensitive x-ray imaging *Med. Phys.* **34** 737–743

Xop 2.3 – website: http://www.esrf.eu/Instrumentation/software/data-analysis/xop2.4. (accessed on 15.10.2015).

Yaffe M J et al 2009 The mith of the 50/50 breast *Med. Phys.* **36** 5437–5443

Yang K et al 2007 Computer modeling of the spatial resolution properties of a dedicated breast CT system *Med. Phys.* **34** 2059–2069

Yang K et al 2008 Noise power properties of a cone-beam CT system for breast cancer detection *Med. Phys.* **35** 5317–5327

Yang X et al 2012 Cupping artifact correction and automated classification for high-resolution dedicated breast CT images *Med. Phys.* **39** 6397–6406

Yi Y et al 2011 Radiation doses in cone-beam breast computed tomography: a Monte Carlo simulation study *Med. Phys.* **38** 589–597

Zhao Y et al 2012 High-resolution, low-dose phase contrast X-ray tomography for 3D diagnosis of human breast cancers *PNAS* **109** 18290-4

Zhao B et al 2015 Cone beam breast CT with multiplanar and three dimensional visualization in differentiating breast masses compared with mammography *Eur. J. Radiol.* **84** 48–53

Zyganitidis C et al 2007 A novel simulation algorithm for soft tissue compression *Med. Biol. Eng. Comp.* **45** 661–669

8. Included papers and attributions

The following published papers arose from the work of this thesis:

1. **Sarno A**, Mettivier G and Russo P. Dedicated breast computed tomography: basic aspects *Med. Phys.* (2015) **42** 2786–2804

2. Mettivier G, Fedon C, Di Lillo F, Longo R, **Sarno A**, Tromba G and Russo P. Glandular dose in synchrotron radiation breast computed tomography *Phys. Med. Biol.* **61** (2015) 569–587

3. Longo R, Arfelli F, Bellazzini R, Bottigli U, Brez A, Brun F, Brunetti A, Delogu P, Di Lillo F, Dreossi D, Fanti V, Fedon C, Golosio B, Lanconelli N, Mettivier G, Minuti M, Oliva P, Pinchera M, Rigon L, Russo P, **Sarno A**, Spandre G, Tromba G and Zanconati F. Towards breast tomography with synchrotron radiation at Elettra: first images *Phys. Med. Biol.* **61** (2016) 1634–1649

4. **Sarno A**, Mettivier G, Golosio B, Oliva P, Spandre G, Di Lillo F, Fedon C, Longo R and Russo P. Imaging performance of phase-contrast breast computed tomography with synchrotron radiation and a CdTe photon-counting detector *Phys. Medica* (2016) **32** 681–690

5. Di Lillo F, Mettivier G, **Sarno A**, Tromba G, Tomic N, Devic S and Russo P. Energy dependent calibration of XR-QA2 radiochromic film with monochromatic and polychromatic x-ray beams *Med. Phys.* **43** (2016) 583–588

6. **Sarno A**, Mettivier G, Di Lillo F and Russo P. Monte Carlo evaluation of normalized glandular dose coefficients in mammography *In: Breast Imaging.* Proc. of 13th International Workshop, IWDM 2016, Malmö, Sweden, June 19-22, 2016, *Lecture Notes in Computer Science, Springer International Publishing, vol 9699,* 190–196 DOI 10.1007/978-3-319-41546-8_25

7. Giovanni M, Bliznakova K, Di Lillo F, **Sarno A** and Russo P. Evaluation of the BreastSimulator Software Platform for Breast Tomography: Preliminary Results. Proc. of 13th International Workshop, IWDM 2016, Malmö, Sweden, June 19-22, 2016, *Lecture Notes in Computer Science, Springer International Publishing, vol 9699,* 145–151

8. **Sarno A**, Mettivier G, Di Lillo F, Cesarelli M, Bifulco P and Russo P. Cone-beam micro computed tomography dedicated to the breast *Med. Eng. Phys.* **38** (2016) 1449–1457

9. **Sarno A**, Mettivier G, Di Lillo F and Russo P. A Monte Carlo study of monoenergetic and polyenergetic normalized glandular dose (DgN) coefficients in mammography *Phys. Med. Biol.* (2016) **62** 306–325

10. Delogu P, Golosio B, Fedon C, Arfelli F, Bellazzini R, Brez A, Brun F, Di Lillo F, Dreossi D, Mettivier G, Minuti M, Oliva P, Pichera M, Rigon L, Russo P, **Sarno A**, Spandre G, Tromba G and Longo R. Imaging study of a phase-sensitive breast-CT system in continuous acquisition mode *J. Instrum* **12** (2017) C01016.

The following ongoing papers arose from the work of this thesis:

1. **Sarno A**, Dance D R, van Engen R E, Young K C, Russo P, Di Lillo F, Mettivier G, Bliznakova K, Fei B W and Sechopoulos I. A Monte Carlo model for mean glandular dose evaluation in spot compression mammography. *Med. Phys.* (2017) *under review.*

2. **Sarno A**, Golosio B, Russo P, Arfelli F, Bellazzini R, Brez A, Brun F, Delogu P, Di Lillo F, Dreossi D, Fedon C, Longo R, Mettivier G, Oliva P, Rigon L, Spandre G and Tromba G. A framework for iterative reconstruction in phase-contrast computed tomography dedicated to the breast. *Trans. Rad. Pl. Med. Sc.(2017) under review*.

3. **Sarno A,** Mettivier G and Russo P. Air kerma calculation in Monte Carlo simulations for deriving normalized glandular dose coefficients in mammography. *Phys. Med Biol.* (2017) *under review*.

4. **Sarno A**, Masi M, Antonelli N, Di Lillo F, Mettivier G, Castriconi R and Russo P. Dose Volume Distribution in Digital Breast Tomosynthesis: a Phantom Study. *Trans. Rad. Pl. Med. Sc. (2017) under review*.

The following presentations at congresses arose from the work of this thesis:

1. Specifications of a computed tomography dedicated to the breast with synchrotron radiation, oral presentation at SIF congress, Rome (Italy) 24th September 2015

2. Image quality in synchrotron radiation breast CT, poster at AIFM congress, Perugia (Italy) 25th – 28th February 2016

3. Geant4 calculation of normalized glandular dose coefficients in computed tomography dedicated to the breast, oral presentation at the European Congress of Medical Physics, Athens (Greece) 1st – 4th September 2016.

4. A framework for iterative reconstruction in phase-contrast computed tomography dedicated to the breast, poster at IEEE NSS/MIC congress, Strasburg (France) 29th October – 4th November 2016.

5. Volume Distribution in Digital Breast Tomosynthesis: a Phantom Study, oral presentation at IEEE NSS/MIC congress, Strasburg (France) 29th October – 4th November 2016.

9. Supplementary Material

9.1. Appendix A

The Monte Carlo code used for the results reported in sections 2.1., 2.2. and 3.1. has been tested by performing cases I, II, III of the American Association of Physicists in Medicine Task Group Report 195 (AAPM 2015; Sechopoulos *et al* 2015).

A.1. Case I

Four beams were simulated: *a*) a monoenergetic beam at 30 keV, *b*) a monoenergetic beam at 100 keV, *c*) a polyenergetic spectrum produced by Mo anode and 0.0386 mm Mo added filtration at 30 kVp, and *d*) a spectrum produced by W anode and 2.708 mm Al filtration at 100 kVp. The air kerma was evaluated on a disc of 10 mm diameter at 1000 mm from the source, both by placing an aluminum layer in the X-ray beam path and without it. In each case, the thickness of the Al layer was equal to the HVL or to the quarter value layer (QVL) of the beam under examination. Finally, two quantities were calculated: the ratio between the scored air kerma evaluated with the HVL of Al (quantity R_3) or the QVL of Al (quantity R_4), to the air kerma evaluated without the Al layer in the beam path.

Figure A1 shows values of R_3 (Fig. A1a) and R_4 (Fig. A1b) calculated by our MC code, in comparison with TG-195 data. The air kerma contribution due to the scattered radiation was taken into account. This figure indicates a reasonable agreement between the results of the two simulation codes. The TG-195 proposes, additionally, to compute such values without taking into account the scattered radiation (quantities R_1 and R_2): for brevity, the corresponding results were not reported.

Table A.I shows the absolute value of the difference between data from TG-195 and data in this work. The discrepancies are not statistically significant. It is worth noting that the highest difference, both for R_3 and R_4, were obtained with a monoenergetic beam at 30 keV and that in both cases the results obtained with the MC code presented in this work are closer to the theoretical values than that proposed in TG-195 (0.500 for R_3 and 0.250 for R_4, respectively).
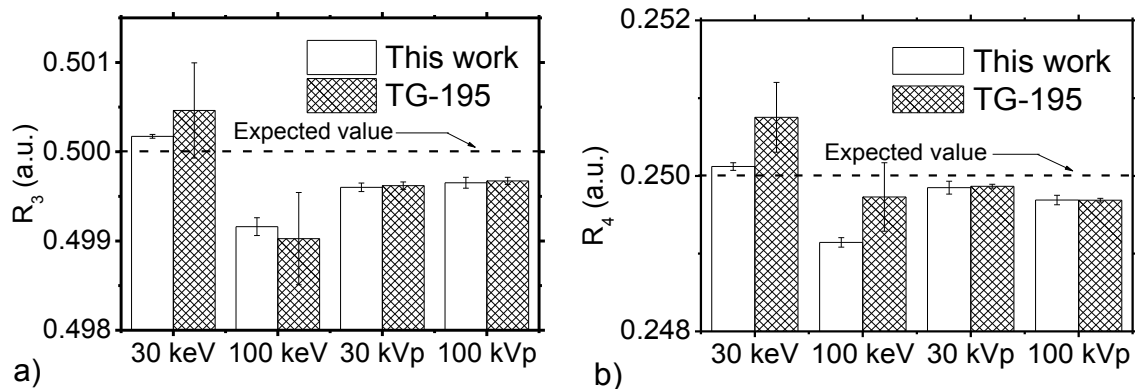
Fig. A1*: Air kerma ratio for (a) HVL and (b) QVL Al layers. Results were obtained our MC code and that adopted in AAPM TG report 195.*

Table A.I. Comparison of R3 and R4 values computed with our MC code and data reported in the TG-195 report.

		30 keV	100 keV	30 kVp	100 kVp
R_3	**This work**	0.5002±0.0001	0.4992±0.0001	0.4996±0.0001	0.4997±0.0001
	TG-195	0.5005±0.0005	0.4990±0.0005	0.4996±0.0000	0.4997±0.0000
	Absolute difference ($\times 10^{-4}$)	3 ± 6	1 ± 6	0 ± 1	0 ± 1
R_4	**This work**	0.2501±0.0001	0.2491±0.0001	0.2499±0.0001	0.2497±0.0001
	TG-195	0.2508±0.0004	0.2497±0.0004	0.2499±0.0000	0.2497±0.0000
	Absolute difference ($\times 10^{-4}$)	6 ± 5	6 ± 5	0 ± 1	0 ± 1

A.2. Case II

A soft-tissue body of $390\times390\times200$ mm^3 was irradiated by a monoenergetic point source at 56.4 keV or by a polyenergetic point source at 120 kVp (W anode and added filtration of 2.861 mm Al), both placed at 1550 from the upper surface. A pencil beam and then a full field beam were simulated, which irradiated a scoring plane of 390×390 mm^2 placed at 50 mm beyond the body. The TG-195 report scored the energy deposited per photon in the nine volumes of interest (VOIs, from VOI1 to VOI9) and the energy fluence through seven scoring planar regions of interest (ROIs, from ROI1 to ROI7). We scored both the primary and secondary photon fluence in the ROIs, on the whole detector area.

Tables A.II and A.III show results for MC validation relative to the TG-195, case II. These tables report the energy per photon released in four out of nine VOIs (VOIs 1, 2, 3 and 9) in the case of full field irradiation at 56.4 keV (Tab. A.II) and with a polyenergetic spectrum at 120 kVp (Tab. A.III), respectively.

Table A.II. *Released energy per photon (eV) in the body VOIs # 1, 2, 3 and 9, in full field irradiation at 56.4 keV and the absolute difference between data simulated via our MC code those reported in TG-195.*

	VOI$_1$	VOI$_2$	VOI$_3$	VOI$_9$
This work	26.94±0.25	27.08±0.22	36.74±0.27	14.51±0.27
TG-195	27.10±0.01	27.08±0.01	36.44±0.02	14.80±0.01
Absolute Difference	0.16±0.26	0±0.23	0.30±0.29	0.29±0.28

Tables A.IV and A.V show the photon energy fluence at the detector plane, evaluated in the ROI$_5$ (at the center of the detector plane) and in the ROI$_1$ (at the edge of the detector plane). Table A.IV shows energy fluence per generated photon, due by the primary or by the secondary photons, in the

detector's ROI_5, in the case of full field and of a pencil beam. Table A.V shows the energy fluence for secondary photons through the detector's ROI_1. Tables A.II−A.V show that the discrepancies with respect to the AAPM TG report195 are within the statistical uncertainty.

Table A.III. Released energy per photon in the body VOIs # 1, 2, 3 and 9, in full field irradiation at 120 kVp and the absolute difference between data simulated via our MC code and those reported in TG-195.

	VOI_1	VOI_2	VOI_3	VOI_9
This work	24.96±0.31	24.89±0.23	33.54±0.32	13.29±0.17
TG-195	24.99±0.01	24.99±0.01	33.18±0.02	13.75±0.01
Absolute Difference	0.03±0.32	0.10±0.24	0.36±0.34	0.46±0.18

Table A.IV. Energy fluence due to primary and secondary photons on the detector ROI5 in full field irradiation and the absolute difference between data simulated via our MC code and those reported in TG-195. Values in parentheses refer to the case of pencil beam irradiation.

	Primary		**Secondary**	
	56.4 keV	**120 kVp**	**56.4 keV**	**120 kVp**
This work	4.40±0.05	5.19±0.05	15.59±0.06	17.65±0.12
	(736.73±0.70)	(863.89±0.75)	(116.94±0.20)	(119.13±0.28)
TG-195	4.42±0.01	5.17±0.01	15.82±0.01	17.70±0.01
	(737.09±0.09)	(863.49±0.11)	(117.02±0.04)	(118.68±0.04)
Absolute Difference	0.02±0.06	0.02±0.06	0.23±0.07	0.05±0.13
	(0.36±0.79)	(0.40±0.86)	(0.08±0.24)	(0.45±0.32)

Table A.V. Energy fluence due to the secondary photons on the detector ROI1, both in full field irradiation and in pencil beam irradiation and absolute difference in values computed with our code and data reported in TG-195.

	Full field		**Pencil beam**	
	56.4 keV	**120 kVp**	**56.4 keV**	**120 kVp**
This work	4.22±0.14	4.84±0.20	26.79±0.35	29.80±0.40
TG-195	4.13±0.01	4.61±0.01	26.75±0.02	29.73±0.02
Absolute Difference	0.09±0.15	0.23± 0.20	0.04± 0.37	0.07±0.42

A.3 Case III

We modeled a compressed breast as reported in sect. 2.1, and calculated the MGD per incident photon at 16.8 keV as well as with a polyenergetic spectrum at 30 kVp (Mo anode and added filtration of 0.0386 mm Mo).

Figure A2 shows the results relative to the validation of case III. The discrepancies are 0.1% and 0.5% at 16.8 keV and for a 30-kVp spectrum, respectively, largely contained in the statistical uncertainty of the MC simulations.
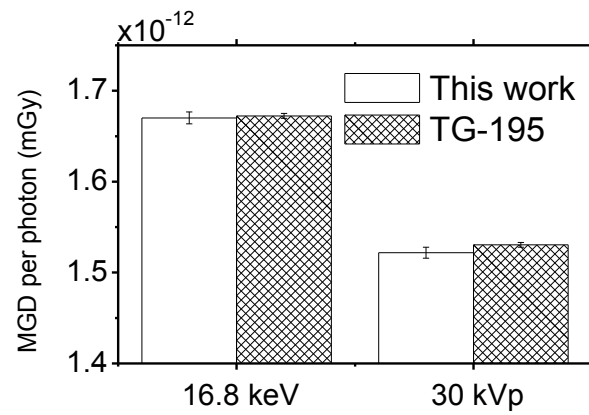
Fig. A2. MGD per photon in mammographic setup for monoenergetic X-rays at 16.8 keV and for a polyenergetic spectrum at 30 kVp (Mo/Mo).

9.2. Appendix B
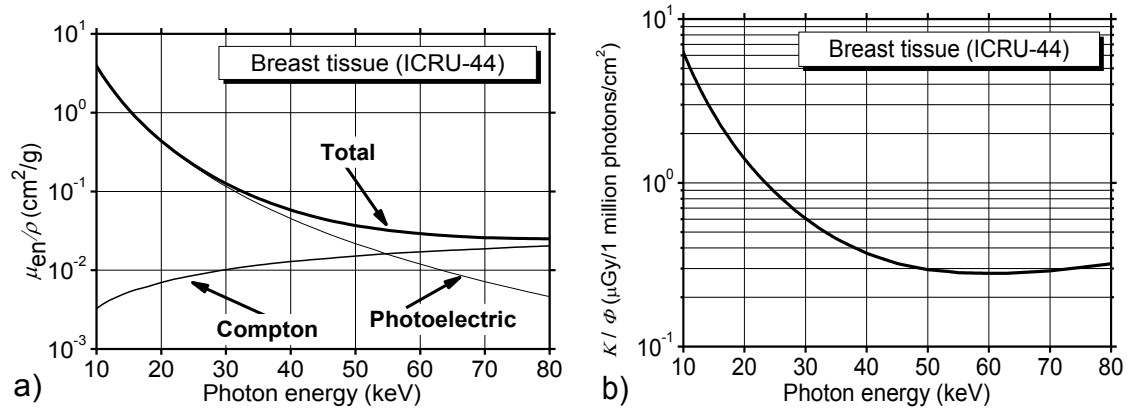
Fig. B1: *a) Mass energy absorption coefficients for breast tissue (with composition from the ICRU-44 report, ICRU), and the mass energy absorption coefficients calculated with XMuDat (Nowotny 1998) with interaction cross section data from Boone and Chavez (1996). b) Monoenergetic kerma in breast tissue for a fluence of 10^6 photons/cm^2.*

9.3. Appendix C

The DgN$_{CT}$ fitting function is the following:

$$DgN_{CT}(E) = a * 10^{-14} * E^8 + b * 10^{-11} * E^7 + c * 10^{-9} * E^6 + d * 10^{-7} * E^5 + e * 10^{-5} * E^4 + f * 10^{-4} * E^3 + g * E^2 + h * E$$

The energy, E, is in keV. For the cases presented in this work, the fitting R^2 is higher than 0.9998.

In the sect C.1 the fitting parameters for the cases in which the breast height is modeled as long as the breast radius are reported. In sect. C.2 and C.3 are reported the cases in which the breast height is respectively 1.5 and 2 times the breast radius. The breast is modeled with a skin thickness of 1.45 mm and the chest-wall to the central beam distance is 0 mm.

In sect. C4, C.5 and C.6 the polyenergetic DgN$_{CT}$ for breast height equal to 1, 1.5 and 2 times the breast radius are reported. They have been evaluated for 49 kVp W spectra, as used in the koning apparatus, with the HVL comprised in the range 1.25–1.50 mm Al. The breast is modeled with a skin thickness of 1.45 mm and the chest-wall to the central beam distance is 0 mm.

C.1. Monoenergetic DgN$_{CT}$ - Breast height = 1 x Breast radius

	Glandular fraction by mass = 0%					
	Breast diameter					
	8	10	12	14	16	18
a	-21.2249	-15.118	-12.1114	-8.6325	-5.9438	-2.5415
b	7.53265	5.54748	4.53644	3.33854	2.40003	1.23986
c	-10.9225	-8.33617	-6.97949	-5.30985	-3.97894	-2.36505
d	8.24699	6.54386	5.63166	4.43632	3.46096	2.29178
e	-3.39187	-2.81148	-2.50107	-2.04408	-1.65822	-1.19424
f	7.05976	6.16129	5.72053	4.85799	4.08627	3.12659
g	-0.00546	-0.00512	-0.0051	-0.00449	-0.00386	-0.00299
h	0.01316	0.01375	0.01515	0.01399	0.01225	0.00945

Glandular fraction by mass = 14.3%

Breast diameter

	8	10	12	14	16	18
a	-18.9275	-14.2754	-9.74201	-6.97586	-4.51621	-1.54007
b	6.77391	5.26277	3.72935	2.77563	1.88913	0.857547
c	-9.92318	-7.96006	-5.86519	-4.53506	-3.23866	-1.77559
d	7.58755	6.30494	4.8392	3.88824	2.90922	1.82503
e	-3.17041	-2.743	-2.19811	-1.83732	-1.43792	-0.996027
f	6.7358	6.12565	5.13763	4.47635	3.64892	2.7039
g	-0.00538	-0.00529	-0.00465	-0.00424	-0.00353	-0.00263
h	0.01358	0.01494	0.01394	0.01351	0.01151	0.00839

Glandular fraction by mass = 25%

Breast diameter

	8	10	12	14	16	18
a	-17.0422	-13.2066	-8.62982	-5.65986	-3.07909	-1.39897
b	6.16958	4.90336	3.35665	2.30072	1.39852	0.78399
c	-9.14411	-7.47699	-5.36506	-3.84178	-2.55624	-1.63671
d	7.07577	5.97998	4.50175	3.36776	2.41736	1.70013
e	-2.993	-2.63325	-2.0825	-1.62739	-1.24616	-0.940475
f	6.43933	5.97703	4.97206	4.04911	3.27083	2.59825
g	-0.00521	-0.00531	-0.00464	-0.00388	-0.00323	-0.00259
h	0.01326	0.01572	0.01463	0.01247	0.01076	0.00865

Glandular fraction by mass = 50%

Breast diameter

	8	10	12	14	16	18
a	-15.43170	-9.64893	-5.46673	-2.57946	-0.891419	1.04082
b	5.62744	3.70319	2.25201	1.24421	0.601712	-0.0859162
c	-8.42412	-5.84345	-3.80283	-2.36604	-1.37303	-0.367464
d	6.61022	4.84345	3.36427	2.29919	1.50505	0.733077
e	-2.85302	-2.21476	-1.63739	-1.20831	-0.863638	-0.536258
f	6.33414	5.23254	4.0965	3.21694	2.44874	1.71916
g	-0.00546	-0.00485	-0.00395	-0.00321	-0.00248	-0.00177
h	0.01537	0.01512	0.01277	0.01083	0.00839	0.00585

Glandular fraction by mass = 75%

	Breast diameter					
	8	10	12	14	16	18
a	-10.5296	-7.68077	-3.03223	-0.625102	0.851724	1.78676
b	4.01079	3.00827	1.40367	0.527167E	-0.0346021	-0.392628
c	-6.27773	-4.85586	-2.59673	-1.29475	-0.423704	0.141413
d	5.15418	4.12848	2.47428	1.46926	0.766814	0.298722
e	-2.32828	-1.94267	-1.28144	-0.859178	-0.549714	-0.336678
f	5.40619	4.74195	3.37486	2.465	1.75905	1.25669
g	-0.00485	-0.00457	-0.00335	-0.00253	-0.00184	-0.00133
h	0.01447	0.01492	0.01111	0.00867	0.00625	0.00445

Glandular fraction by mass = 100%

	Breast diameter					
	8	10	12	14	16	18
a	-8.9488	-4.68938	-1.25665	1.67429	2.14137	3.10801
b	3.46912	1.97307	0.73955	-0.290499	-0.507394	-0.877788
c	-5.53306	-3.39503	-1.58909	-0.1031110	0.292036	0.875523
d	4.63874	3.05768	1.68438	0.56091	0.19665	-0.285593
e	-2.14704	-1.51537	-0.946339	-0.478334	-0.299279	-0.0796923
f	5.13999	3.86457	2.64934	1.62936	1.18677	0.665263
g	-0.00484	-0.0038	-0.00269	-0.00172	-0.00128	-0.0007426
h	0.01546	0.01255	0.00906	0.00586	0.00428	0.00236

C.2. Monoenergetic DgN$_{CT}$ - Breast height = 1.5 x Breast radius

Glandular fraction by mass = 0%

	Breast diameter					
	8	10	12	14	16	18
a	-21.9406	-16.9424	-10.9843	-6.82949	-3.94221	-0.888935
b	7.80357	6.17134	4.18877	2.76827	1.73724	0.675773
c	-11.3525	-9.23426	-6.56733	-4.59788	-3.10281	-1.59318
d	8.61466	7.24856	5.40737	3.99959	2.87956	1.7585
e	-3.5706	-3.13341	-2.45489	-1.91359	-1.46049	-1.00349
f	7.52642	6.98624	5.75078	4.7056	3.77678	2.80461
g	-0.00599	-0.00612	-0.00526	-0.00445	-0.00367	-0.00276
h	0.01508	0.01789	0.01619	0.01417	0.01204	0.009

Glandular fraction by mass = 14.3%

Breast diameter

	8	10	12	14	16	18
a	-19.9782	-13.885	-9.13756	-4.59112	-2.59897	-0.247185
b	7.17493	5.1587	3.5565	1.99031	1.24452	0.407535
c	-10.5525	-7.87598	-5.69528	-3.49983	-2.36701	-1.14717
d	8.11	6.31073	4.79362	3.19837	2.31109	1.38205
e	-3.41419	-2.78569	-2.22697	-1.59734	-1.22331	-0.834814
f	7.3498	6.33957	5.34578	4.07062	3.27622	2.42975
g	-0.00607	-0.00563	-0.00502	-0.00393	-0.00324	-0.00244
h	0.01626	0.01669	0.01596	0.01266	0.01077	0.00804

Glandular fraction by mass = 25%

Breast diameter

	8	10	12	14	16	18
a	-17.6096	-11.8145	-7.49196	-3.01081	-0.576202	0.935136
b	6.41224	4.45834	2.9777	1.43631	0.553613	-0.0043237
c	-9.57118	-6.92326	-4.87128	-2.70832	-1.40359	-0.558633
d	7.4737	5.64955	4.19023	2.61205	1.61068	0.941563
e	-3.20107	-2.54237	-1.98976	-1.36176	-0.943911	-0.653564
f	7.02375	5.900	4.87673	3.58688	2.69369	2.04258
g	-0.00594	-0.00533	-0.00465	-0.00351	-0.00271	-0.00208
h	0.0164	0.01602	0.01492	0.01141	0.00899	0.0069

Glandular fraction by mass = 50%

Breast diameter

	8	10	12	14	16	18
a	-13.6441	-8.84617	-4.86725	-1.94025	2.23767	2.49169
b	5.08277	3.44528	2.0584	0.99773	-0.443452	-0.607887
c	-7.78024	-5.52659	-3.5635	-1.99499	0.0434721	0.393605
d	6.24716	4.66581	3.23157	2.02523	0.512606	0.162396
e	-2.76003	-2.17764	-1.61383	-1.10778	-0.485989	-0.306698
f	6.26878	5.26127	4.15175	3.05582	1.69771	1.24805
g	-0.00551	-0.00499	-0.00414	-0.00312	-0.00176	-0.00131
h	0.0159	0.01602	0.01406	0.01069	0.00578	0.00422

Glandular fraction by mass = 75%

	Breast diameter
	8	10	12	14	16	18
a	-10.9882E	-6.24845	-1.49793	0.580191	1.96489	3.61167
b	4.18397	2.52908	0.879397	0.104925	-0.433458	-1.03831
c	-6.55691	-4.21716	-1.87863	-0.696205	0.158355	1.07121
d	5.40185	3.70251	1.97694	1.03528	0.329008	-0.394961
e	-2.45613	-1.79767	-1.10216	-0.692607	-0.373551	-0.0555436
f	5.76873	4.51408	3.06493	2.14763	1.40134	0.663911
g	-0.0053	-0.00442	-0.00312	-0.00225	-0.0015	-0.0007378
h	0.01622	0.01457	0.01061	0.00774	0.00504	0.00225

Glandular fraction by mass = 100%

	Breast diameter
	8	10	12	14	16	18
a	-8.31369	-2.93656	1.06755	2.31123	3.38073	3.68448
b	3.25346	1.38491	-0.0363802	-0.529256	-0.956394	-1.10085
c	-5.24857	-2.605	-0.541286	0.257489	0.953284	1.22625
d	4.46008	2.52122	0.958147	0.284098	-0.305789	-0.568584
e	-2.09677	-1.3253	-0.677103	-0.367133	-0.0938392	0.04.15122
f	5.10476	3.53825	2.14383	1.41254	0.757349	0.407185
g	-0.00488	-0.00355	-0.00226	-0.00153	-0.0008553	-0.0004909
h	0.01576	0.01186	0.00775	0.00522	0.00277	0.00146

C.3. Monoenergetic DgN$_{CT}$ - Breast height = 2 x Breast radius

Glandular fraction by mass = 0%

	Breast diameter
	8	10	12	14	16	18
a	-19.1804	-14.7264	-9.77147	-5.42967	/	/
b	6.93335	5.46624	3.80492	2.30221	/	/
c	-10.258	-8.33515	-6.08915	-3.97583	/	/
d	7.91921	6.6656	5.11591	3.57935	/	/
e	-3.33791	-2.93246	-2.36911	-1.76523	/	/
f	7.13529	6.63122	5.65664	4.45128	/	/
g	-0.00568	-0.0058	-0.00526	-0.00426	/	/
h	0.01426	0.01673	0.0165	0.01365	/	/

Glandular fraction by mass = 14.3%

Breast diameter

	8	10	12	14	16	18
a	-17.8928	-13.0133	-7.49351	-4.19366	/	/
b	6.50841	4.89093	3.02224	1.84862	/	/
c	-9.70139	-7.56029	-5.00097	-3.30172	/	/
d	7.56001	6.13854	4.33812	3.06499	/	/
e	-3.22661	-2.74806	-2.07131	-1.55632	/	/
f	7.02515	6.34648	5.08868	4.03725	/	/
g	-0.00579	-0.00572	-0.00484	-0.00397	/	/
h	0.01528	0.01719	0.01548	0.01317	/	/

Glandular fraction by mass = 25%

Breast diameter

	8	10	12	14	16	18
a	-16.7017	-12.1823	-5.7306	-3.53933	/	/
b	6.12967	4.59784	2.40028	1.59518	/	/
c	-9.23152	-7.14923	-4.11003	-2.90824	/	/
d	7.2806	5.85253	3.67883	2.75431	/	/
e	-3.15244	-2.65009	-1.80768	-1.42701	/	/
f	6.99598	6.22244	4.55179	3.77794	/	/
g	-0.00598	-0.00578	-0.00438	-0.00379	/	/
h	0.01663	0.01823	0.0141	0.01286	/	/

Glandular fraction by mass = 50%

Breast diameter

	8	10	12	14	16	18
a	-12.5066	-7.2782	-3.15468	-0.339208	/	/
b	4.74957	2.94213	1.49243	0.460011	/	/
c	-7.40394	-4.8803	-2.80745	-1.26191	/	/
d	6.04904	4.24598	2.71329	1.50914	/	/
e	-2.71778	-2.03505	-1.42357	-0.911261	/	/
f	6.27825	5.02486	3.79612	2.66867	/	/
g	-0.00563	-0.00481	-0.00383	-0.00275	/	/
h	0.01678	0.01553	0.01305	0.00942	/	/

Glandular fraction by mass = 75%

	Breast diameter					
	8	10	12	14	16	18
a	-11.2482	-6.4829	-0.568603	2.12966	/	/
b	4.2791	2.59329	0.563029	-0.432077	/	/
c	-6.70799	-4.29143	-1.43884	0.057985	/	/
d	5.53784	3.75515	1.66006	0.488523	/	/
e	-2.53004	-1.82511	-0.978771	-0.47771	/	/
f	5.99863	4.60807	2.81749	1.70766	/	/
g	-0.00564	-0.00456	-0.00288	-0.00182	/	/
h	0.018	0.01521	0.00966	0.00618	/	/

Glandular fraction by mass = 100%

	Breast diameter					
	8	10	12	14	16	18
a	-8.31578	-1.8799	0.336007	4.07096	/	/
b	3.28223	1.03091	0.177346	-1.12805	/	/
c	-5.33175	-2.1303	-0.791067	1.0876	/	/
d	4.55871	2.19994	1.1107	-0.314099	/	/
e	-2.15714	-1.21267	-0.732103	-0.131258	/	/
f	5.29729	3.35258	2.26944	0.922474	/	/
g	-0.00514	-0.00343	-0.00241	-0.00104	/	/
h	0.01692	0.01175	0.00842	0.00342	/	/

C.4. Polyenergetic DgN$_{CT}$ - Breast height = 1 x Breast radius

Glandular fraction by mass = 0%

HVL (mm Al)	Breast diameter					
	8	10	12	14	16	18
1.25	0.4848	0.4417	0.4036	0.3723	0.3485	0.3261
1.30	0.4945	0.4512	0.4128	0.3811	0.3570	0.3344
1.35	0.5039	0.4605	0.4218	0.3898	0.3654	0.3424
1.40	0.5130	0.4695	0.4306	0.3982	0.3736	0.3503
1.45	0.5219	0.4782	0.4391	0.4065	0.3816	0.3580
1.50	0.5305	0.4868	0.4475	0.4146	0.3895	0.3656

Glandular fraction by mass = 14.3%

HVL	Breast diameter					
(mm Al)	8	10	12	14	16	18
1.25	0.4655	0.4224	0.3833	0.3529	0.3294	0.3074
1.30	0.4751	0.4318	0.3923	0.3615	0.3376	0.3153
1.35	0.4844	0.4409	0.4010	0.3699	0.3457	0.3231
1.40	0.4935	0.4498	0.4095	0.3781	0.3537	0.3307
1.45	0.5024	0.4585	0.4179	0.3862	0.3615	0.3382
1.50	0.5109	0.4669	0.4261	0.3941	0.3691	0.3455

Glandular fraction by mass = 25%

HVL	Breast diameter					
(mm Al)	8	10	12	14	16	18
1.25	0.4520	0.4090	0.3743	0.3414	0.3173	0.3010
1.30	0.4615	0.4182	0.3832	0.3499	0.3254	0.3088
1.35	0.4707	0.4272	0.3919	0.3582	0.3334	0.3165
1.40	0.4797	0.4360	0.4005	0.3663	0.3412	0.3241
1.45	0.4885	0.4447	0.4088	0.3743	0.3488	0.3315
1.50	0.4970	0.4530	0.4170	0.3821	0.3563	0.3389

Glandular fraction by mass = 50%

HVL	Breast diameter					
(mm Al)	8	10	12	14	16	18
1.25	0.4279	0.3806	0.3434	0.3186	0.2943	0.2684
1.30	0.4374	0.3896	0.3519	0.3268	0.3021	0.2757
1.35	0.4467	0.3984	0.3603	0.3348	0.3097	0.2828
1.40	0.4557	0.4070	0.3685	0.3427	0.3172	0.2898
1.45	0.4645	0.4154	0.3765	0.3505	0.3246	0.2967
1.50	0.4730	0.4237	0.3844	0.3581	0.3318	0.3035

Glandular fraction by mass = 75%

HVL (mm Al)	Breast diameter					
	8	10	12	14	16	18
1.25	0.4042	0.3556	0.3222	0.2930	0.2672	0.2512
1.30	0.4136	0.3644	0.3305	0.3008	0.2745	0.2581
1.35	0.4227	0.3730	0.3386	0.3084	0.2816	0.2649
1.40	0.4316	0.3814	0.3466	0.3159	0.2886	0.2716
1.45	0.4403	0.3896	0.3544	0.3233	0.2955	0.2782
1.50	0.4488	0.3977	0.3621	0.3306	0.3024	0.2848

Glandular fraction by mass = 100%

HVL (mm Al)	Breast diameter					
	8	10	12	14	16	18
1.25	0.3798	0.3331	0.3000	0.2723	0.2456	0.2289
1.30	0.3889	0.3416	0.3079	0.2797	0.2524	0.2354
1.35	0.3978	0.3499	0.3157	0.2869	0.2592	0.2417
1.40	0.4065	0.3580	0.3233	0.2941	0.2658	0.2480
1.45	0.4151	0.3660	0.3308	0.3011	0.2723	0.2542
1.50	0.4234	0.3738	0.3383	0.3081	0.2788	0.2603

C.5. Polyenergetic DgN$_{CT}$ - Breast height = 1.5 x Breast radius

Glandular fraction by mass = 0%

HVL (mm Al)	Breast diameter					
	8	10	12	14	16	18
1.25	0.5023	0.4571	0.4228	0.3931	0.3646	0.3419
1.30	0.5125	0.4672	0.4327	0.4027	0.3738	0.3507
1.35	0.5225	0.4771	0.4424	0.4121	0.3828	0.3594
1.40	0.5321	0.4867	0.4519	0.4213	0.3917	0.3679
1.45	0.5415	0.4961	0.4611	0.4303	0.4003	0.3763
1.50	0.5507	0.5052	0.4701	0.4391	0.4089	0.3845

Glandular fraction by mass = 14.3%

HVL (mm Al)	Breast diameter					
	8	10	12	14	16	18
1.25	0.4884	0.4446	0.4064	0.3684	0.3457	0.3192
1.30	0.4987	0.4547	0.4162	0.3776	0.3546	0.3276
1.35	0.5087	0.4646	0.4257	0.3866	0.3633	0.3358
1.40	0.5184	0.4742	0.4351	0.3955	0.3719	0.3440
1.45	0.5279	0.4836	0.4442	0.4042	0.3803	0.3520
1.50	0.5371	0.4928	0.4532	0.4127	0.3886	0.3599

Glandular fraction by mass = 25%

HVL (mm Al)	Breast diameter					
	8	10	12	14	16	18
1.25	0.4745	0.4296	0.3872	0.3563	0.3280	0.3113
1.30	0.4848	0.4396	0.3967	0.3654	0.3365	0.3196
1.35	0.4947	0.4493	0.4059	0.3743	0.3450	0.3278
1.40	0.5045	0.4588	0.4150	0.3830	0.3533	0.3358
1.45	0.5139	0.4682	0.4239	0.3916	0.3614	0.3438
1.50	0.5231	0.4773	0.4327	0.4000	0.3695	0.3516

Glandular fraction by mass = 50%

HVL (mm Al)	Breast diameter					
	8	10	12	14	16	18
1.25	0.4455	0.3985	0.3571	0.3251	0.3034	0.2798
1.30	0.4556	0.4081	0.3662	0.3337	0.3116	0.2875
1.35	0.4654	0.4176	0.3751	0.3421	0.3196	0.2951
1.40	0.4750	0.4268	0.3839	0.3504	0.3275	0.3025
1.45	0.4844	0.4359	0.3925	0.3585	0.3354	0.3099
1.50	0.4935	0.4448	0.4009	0.3665	0.3431	0.3172

Glandular fraction by mass = 75%

HVL (mm Al)	Breast diameter					
	8	10	12	14	16	18
1.25	0.4192	0.3675	0.3339	0.3022	0.2750	0.2558
1.30	0.4291	0.3768	0.3426	0.3103	0.2826	0.2630
1.35	0.4388	0.3859	0.3512	0.3184	0.2901	0.2701
1.40	0.4482	0.3948	0.3597	0.3263	0.2975	0.2771
1.45	0.4575	0.4035	0.3680	0.3341	0.3048	0.2840
1.50	0.4666	0.4121	0.3762	0.3418	0.3120	0.2908

Glandular fraction by mass = 100%

HVL (mm Al)	Breast diameter					
	8	10	12	14	16	18
1.25	0.3890	0.3446	0.3047	0.2784	0.2548	0.2343
1.30	0.3986	0.3536	0.3129	0.2861	0.2620	0.2410
1.35	0.4079	0.3624	0.3210	0.2937	0.2691	0.2477
1.40	0.4170	0.3710	0.3290	0.3012	0.2761	0.2542
1.45	0.4259	0.3795	0.3368	0.3086	0.2830	0.2607
1.50	0.4347	0.3878	0.3446	0.3159	0.2899	0.2672

C.6. Polyenergetic DgN$_{CT}$ - Breast height = 2 x Breast radius

Glandular fraction by mass = 0%

HVL (mm Al)	Breast diameter					
	8	10	12	14	16	18
1.25	0.5145	0.4715	0.4315	0.3990	/	/
1.30	0.5252	0.4821	0.4418	0.4089	/	/
1.35	0.5356	0.4924	0.4518	0.4186	/	/
1.40	0.5456	0.5025	0.4616	0.4281	/	/
1.45	0.5554	0.5124	0.4713	0.4374	/	/
1.50	0.5649	0.5220	0.4807	0.4466	/	/

Glandular fraction by mass = 14.3%

HVL (mm Al)	Breast diameter					
	8	10	12	14	16	18
1.25	0.4995	0.4545	0.4101	0.3773	/	/
1.30	0.5102	0.4650	0.4202	0.3869	/	/
1.35	0.5206	0.4753	0.4299	0.3962	/	/
1.40	0.5307	0.4853	0.4396	0.4055	/	/
1.45	0.5406	0.4951	0.4490	0.4145	/	/
1.50	0.5502	0.5047	0.4582	0.4234	/	/

Glandular fraction by mass = 25%

HVL (mm Al)	Breast diameter					
	8	10	12	14	16	18
1.25	0.4816	0.4396	0.3958	0.3627	/	/
1.30	0.4922	0.4500	0.4056	0.3720	/	/
1.35	0.5024	0.4601	0.4153	0.3812	/	/
1.40	0.5125	0.4700	0.4247	0.3902	/	/
1.45	0.5222	0.4797	0.4340	0.3991	/	/
1.50	0.5317	0.4892	0.4431	0.4078	/	/

Glandular fraction by mass = 50%

HVL (mm Al)	Breast diameter					
	8	10	12	14	16	18
1.25	0.4538	0.4083	0.3626	0.3355	/	/
1.30	0.4643	0.4184	0.3719	0.3444	/	/
1.35	0.4744	0.4282	0.3811	0.3532	/	/
1.40	0.4844	0.4378	0.3901	0.3618	/	/
1.45	0.4941	0.4473	0.3990	0.3704	/	/
1.50	0.5035	0.4565	0.4077	0.3788	/	/

Glandular fraction by mass = 75%

HVL (mm Al)	Breast diameter					
	8	10	12	14	16	18
1.25	0.4245	0.3745	0.3379	0.3068	/	/
1.30	0.4346	0.3841	0.3469	0.3152	/	/
1.35	0.4445	0.3935	0.3557	0.3235	/	/
1.40	0.4542	0.4027	0.3644	0.3316	/	/
1.45	0.4637	0.4117	0.3729	0.3397	/	/
1.50	0.4730	0.4206	0.3814	0.3476	/	/

Glandular fraction by mass = 100%

HVL (mm Al)	Breast diameter					
	8	10	12	14	16	18
1.25	0.4002	0.3516	0.3112	0.2831	/	/
1.30	0.4101	0.3608	0.3196	0.2910	/	/
1.35	0.4198	0.3699	0.3280	0.2988	/	/
1.40	0.4293	0.3788	0.3362	0.3065	/	/
1.45	0.4387	0.3876	0.3443	0.3141	/	/
1.50	0.4478	0.3962	0.3523	0.3217	/	/

9.4. Appendix D

Table D.I. *Spatial resolution characterizing BCT systems developed by different research groups.*

Prototype	X-ray tube focal-spot size (mm)	Effective pixel pitch (mm)	Maximum Spatial resolution ($MTF_{0.1}$ - radial direction) (mm^{-1})	Ref.
UC Davis (4th setup)	0.3	0.150	3.7	Gazi *et al* 2013, 2015
U Rochester	0.3	0.388	1.9	Liu *et al* 2012
U Naples (1st setup)	0.04	0.050	3.0	Mettivier *et al* 2011a
U Naples (3rd setup)	0.007-0.050	0.050	3.8	This work
U Erlangen	0.3	0.100	5.3	Kalender *et al* 2016

Table D.II. *$MTF_{0.1}$ in radial, vertical and tangential direction, evaluated at 10 mm from isocenter and for cone angles of 1.8 deg, 3.7 deg and 5.6 deg. 1440 projections; voxel size = 50 × 50 × 50 μm³.*

$MTF_{0.1}$ (mm^{-1}); 1440 projections; 10 mm from isocenter; $M = 1.21$; voxel size = $50 \times 50 \times 50 \ \mu m^3$			
Cone angle (deg)	Radial direction	Vertical direction	Tangential direction
1.8	3.8	6.2	3.0
3.7	3.4	4.8	2.6
5.6	2.5	4.0	2.7

Table D.III. *$MTF_{0.1}$ in radial, vertical and tangential direction, evaluated for a cone angle of 1.8 deg and at 30 mm and 50 mm from isocenter. 1440 projections; voxel size = 50 × 50 × 50 μm³.*

$MTF_{0.1}$ (mm^{-1}); 1440 projections; cone angle 1.8 deg; $M = 1.21$; voxel size = $50 \times 50 \times 50 \ \mu m^3$			
Distance from isocenter (mm)	Radial direction	Vertical direction	Tangential direction
30	3.7	6	2.0
50	3.1	5	2.1
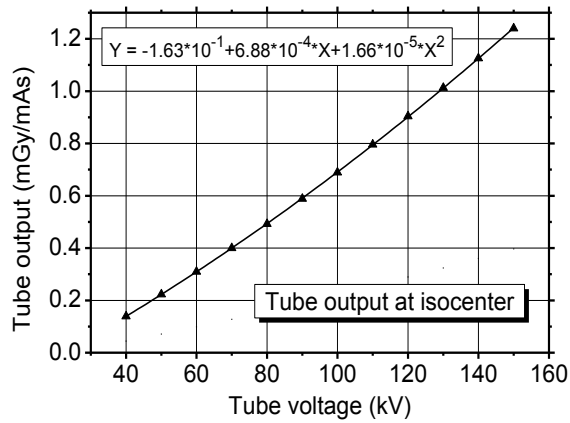
Fig. D1. *X-ray tube output assessed at the scanner isocenter as a function of the tube voltage. A quadratic fit is shown (continuous line) (R2=0.999).*
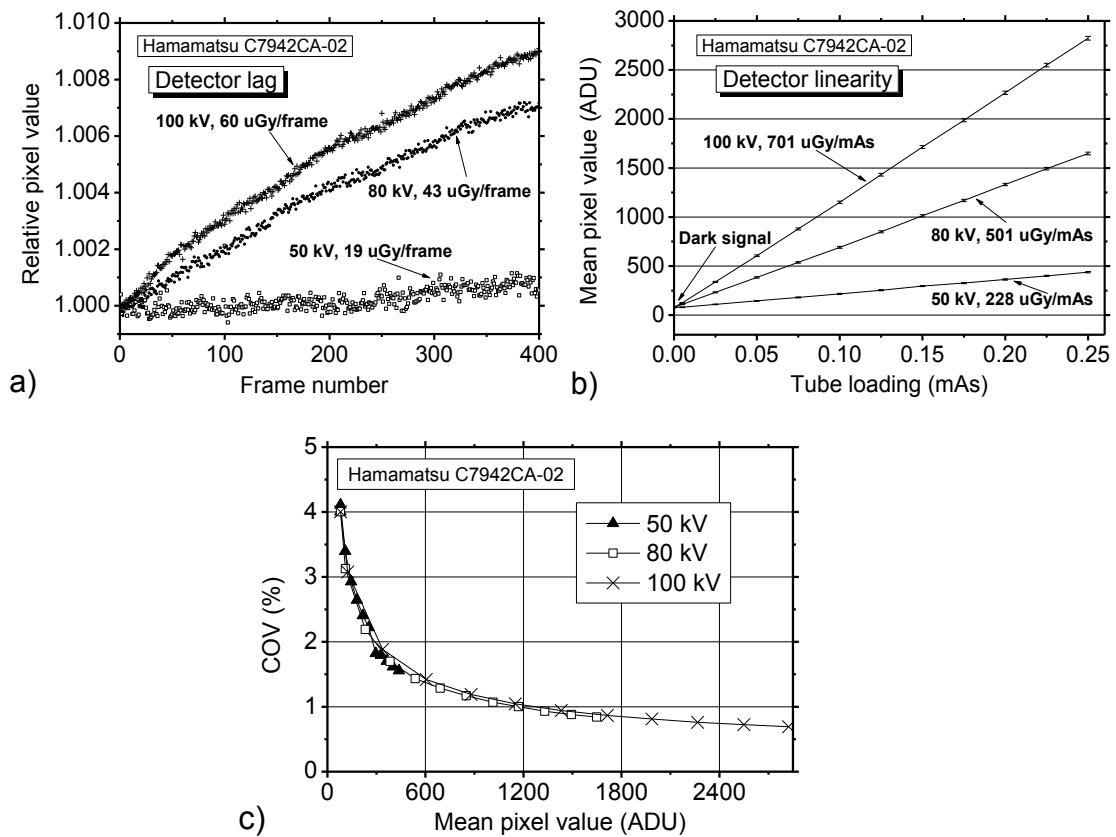
Fig. D2. *a) Time dependent flat-panel response evaluated over 400 consecutive image frames; the curves for the three kilovoltages were normalized to the starting values. b) Linearity curve of flat panel detector. The flat panel was operated at 1×1 binning mode and at 2.13 fps. c) Flat-panel COV as a function of pixel value. The evaluations were performed in a 400×400 pixels ROI at 50 kV, 80 kV and 100 kV.*
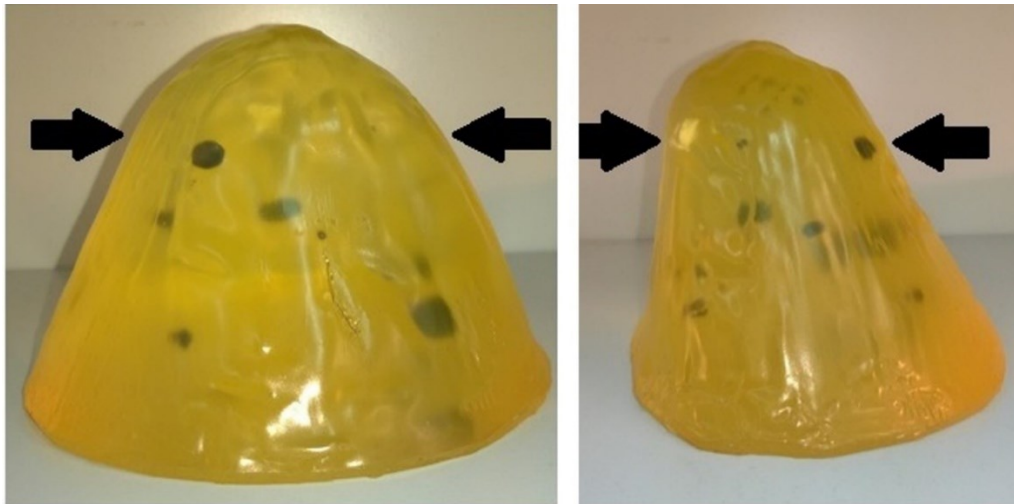
Fig. D3. Breast phantom mod. 1272-00-00. The arrows indicates the height of the section showed in Sec. 4.2.7.
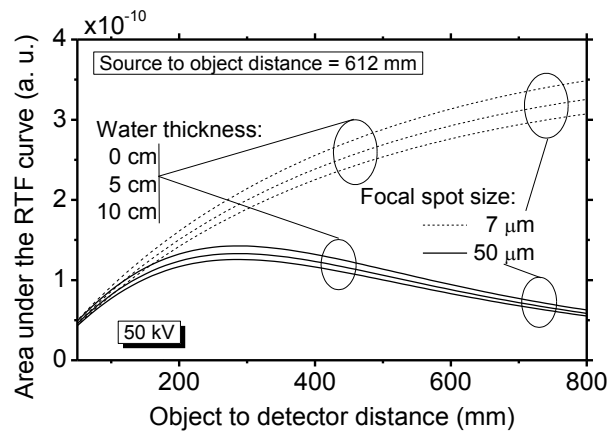
Fig. D4. Area under the RTF curve evaluated for a source-to-isocenter distance of 612 mm and for 7 μm or 50 μm focal spot size. The curve was evaluated for object-to-detector distances in the range 50−800 mm, and for the spectra adopted in the present study (50 kV, HVL = 1.3 mm Al) exiting from 0 cm, 5 cm or 10 cm of water.
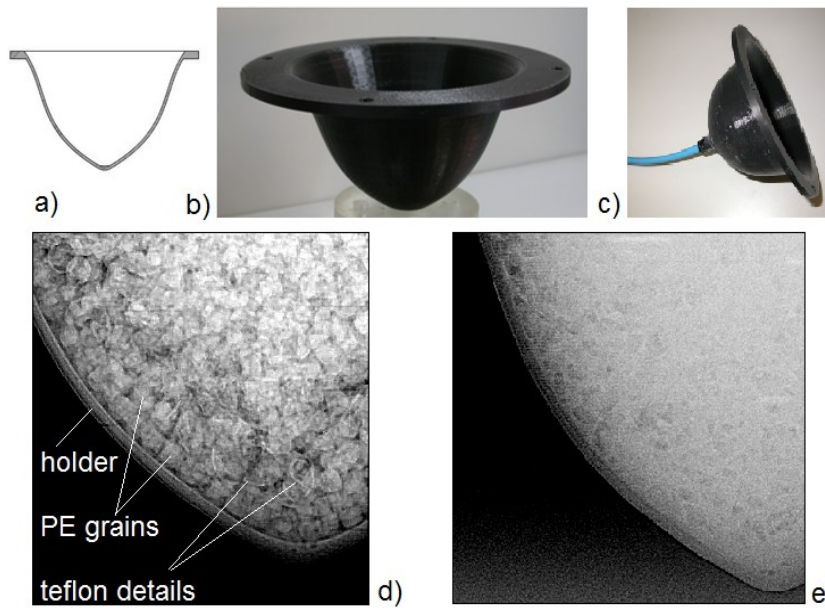
Fig. D5. *Drawings (a) and photo (b) of a breast holder for microCT breast scans. The ABS-plastic holder (weight = 57 g) has a profile shaped as a pendant breast and it has been realized via 3D solid printing; it is intended to host an uncompressed pendant breast with 12 cm diameter at chest wall and ~350 cm3 volume. The holder in c) simulates a 14-cm breast and can be connected, via a valve and plastic tube, to a vacuum pump. In (d) and (e) projections of the breast holder are shown (80 kV, 0.25 mAs, magnification = 1.85). In d) the holder has been filled with 200 g of high-density PE grains of 3-mm size, and 10 g of thin teflon slivers, while in e) the holder is filled with ultrasound gel (≅1.01 g/cm3) and PE grains. The projection images have been processed with a 10-pixel unsharp mask filter.*